MASTERARBEIT | MASTER'S THESIS

Titel | Title

Atomically clean graphene through heating in ultra-high vacuum

verfasst von | submitted by

Philipp Irschik BSc

angestrebter akademischer Grad | in partial fulfilment of the requirements for the degree of

Master of Science (MSc)

Wien | Vienna, 2024

Studienkennzahl lt. Studienblatt	Degree programme code as it appears on the student record sheet:	UA 066 876
Studienrichtung lt. Studienblatt	Degree programme as it appears on the student record sheet:	Masterstudium Physics
Betreut von	Supervisor:	Univ.-Prof. Dr. Jani Kotakoski

Zusammenfassung

Adsorption von Oberflächenkontamination kann während und nach dem Syntheseprozess von zweidimensionalen Materialien wie Graphen, sowie während der Übertragung vom Herstellungssubstrat auf einen anderen Träger, zu Verunreinigungen des Materials führen. Diese Oberflächenkontamination bedeckt nicht nur die darunter liegende Struktur, sondern kann auch die intrinsischen Eigenschaften des Materials negativ beeinflussen. Thermisches Erhitzen der kontaminierten Materialien im Vakuum hat sich als ein effektives Reinigungsverfahren etabliert, welches eine Verminderung der kohlenstoffhaltigen Verunreinigungen hervorruft, ohne das darunter liegende Material deutlich zu beschädigen. Eine Übereinstimmung bezüglich ausreichender Temperaturen und Verfahrungsdauern ist jedoch noch ausständig. Ferner fehlen Informationen, wie sich die Struktur und chemische Zusammensetzung der Kontamination auf atomarer Ebene verändern. Daher wird in dieser Arbeit die Verminderung und Entfernung von Oberflächenkontamination auf Graphen auf atomarer Ebene mittels Rastertransmissionselektronenmikroskopie und Elektronenenergieverlustspektroskopie charakterisiert. Die Proben werden in einer eigens angefertigten Heizkammer im Ultrahochvakuum thermisch erhitzt und im Ultrahochvakuum zum Mikroskop transportiert, so dass die Auswirkungen des Heizens auf den Reinigungsprozess direkt untersucht werden können.

Zufriedenstellende Ergebnisse wurden bei Temperaturen über 150°C erzielt, bei denen die Diffusion der Verunreinigung der vorherrschende Faktor des Reinigungsverfahrens ist. Stark kontaminierte Proben, mit sauberen Stellen im Nanometerbereich, wurden in Proben mit sauberen Bereichen von Hunderten Nanometern Größe konvertiert. Die drastisch erhöhten Größen der sauberen Bereiche können sich bei zukünftigen Durchführungen von Experimenten zur Probenmanipulation als hilfreich erweisen, welche große saubere Stellen bevorzugen, um Wechselwirkungen mit dem Material, und nicht der Kontamination, zu erhöhen.

Abstract

Commercially grown two-dimensional materials such as graphene usually suffer from adsorption of surface contamination during and after the synthesis process. In addition, transfer from the growth substrate onto another, including gold carrier grids often used in (scanning) transmission electron microscopy, can introduce further contamination, obstructing the underlying structure and potentially degrading the material's inherent properties. Thermal annealing in vacuum has been shown to be effective in reducing the amount of carbonaceous surface contamination while inducing only a minimal amount of damage to the underlying material. However, there is no agreed-upon consensus regarding which temperatures and treatment durations are sufficient, in addition to a lack of information on how the local structure and chemical composition of the contamination change on the atomic scale. Hence, in this work atomic-resolution scanning transmission electron microscopy is combined with electron energy loss spectroscopy to assess the reduction and removal of surface contamination down to the atomic level. The samples are thermally annealed in a custom-built ultra-high vacuum heating stage and transferred to the microscope without breaking the vacuum in between, ensuring that the effects of the annealing can be directly characterized.

Satisfactory cleaning results were found at annealing temperatures above 150°C, where the cleaning process is dominated by diffusion of the surface contaminants. A transformation of heavily contaminated samples, with clean areas only in the nanometer scale, into samples with clean patches that are hundreds of nanometers wide was accomplished. The increased average sizes of clean areas can assist in performing sample manipulation experiments in the future, which typically require large clean areas to increase the likelihood of interacting with the material rather than the contamination.

Acknowledgements

First and foremost, I would like to thank my supervisor Jani Kotakoski for not only providing me with the opportunity to work in a field that I have a very high interest in but also for his patience and support throughout my time working in the Physics of Nanostructured Materials group. The freedom I enjoyed here allowed me to implement my own ideas and to have ample time to finish the project at a comfortable pace. Also, I am very grateful for the insightful scientific discussions that we had, which deepened my knowledge in the field of material science and electron microscopy.

Next, I want to thank David Lamprecht, who not only provided me with the necessary training to use the microscope but also for his tremendous assistance with regard to the UHV heating stage. His previous project provided me with a strong head start regarding its design, and his expertise proved essential in re-designing and refining it. Also, he took his time to proofread and correct my thesis and to provide guidance when it came to scientific writing.

Many thanks also go to Clemens Mangler, without whom I would not have been able to implement the heating stage into the CANVAS system. His technical assistance, helpfulness, and patience were invaluable in every step of my project. I would also like to thank Carsten Speckmann, who assisted in the design and assembly of the heating stage.

I am also grateful for the training that I was provided with and the many insightful discussions that I had with Manuel Längle. Our frequent correspondence and general discussions as well as his assistance during microscope operation and the heating stage assembly were incredibly helpful for the progress of my project.

Also, I would like to thank everyone who assisted me with sample preparation, including Shrirang Chokappa, Thi Thuy An Bui, Nandhini Ravindran, and Clara Kofler. They provided me with the necessary training to prepare my own samples, as well as operate the microscopes for pre-characterizing them. A special thanks goes to Thuy An, who took time out of her busy schedule to prepare and characterize samples for me without my presence and also entrusted me with three of her samples. Even though I do not get to present results on her samples here, I still owe her for granting me the opportunity to work with them. Also, she let me use the microscope during some of her allocated time slots, which allowed me to take measurements when time was of the essence.

Furthermore, I would like to extend my thanks to everyone else in the group, who not only entertained me during my time here but also provided me with knowledge and discussion including specialized fields beyond the scope of my project.

Lastly, I would like to thank my parents and close family for providing me with the opportunity to study at my own pace. Without their assistance, I would not have been able to finish my studies in such a comfortable environment.

List of acronyms

2D two-dimensional

AC amorphous carbon

ADF annular dark field

AFM atomic force microscopy

BSE backscattered electron

CANVAS Controlled Alteration of Nanomaterials in Vacuum down to the Atomic Scale

CCD charge-coupled device

CVD chemical vapor deposition

EDX energy dispersive X-ray spectroscopy

EELS electron energy loss spectroscopy

EMCCD electron-multiplying charge-coupled device

FEG field emission gun

FOV field of view

h-BN hexagonal boron nitride

HAADF high-angle annular dark-field

MAADF medium-angle annular dark-field

MBE molecular beam epitaxy

ME mechanical exfoliation

PDMS polydimethylsiloxane

PID proportional-integral-derivative

PL photoluminescence

PMMA poly(methyl methacrylate)

PV process variable

ROI region of interest

SE secondary electron

SEM scanning electron microscopy

SNR signal-to-noise ratio

STEM scanning transmission electron microscopy

STM scanning tunneling microscopy

TEM transmission electron microscopy

TMD transition-metal dichalcogenide

UHV ultra-high vacuum

UV ultraviolet

vdW van der Waals

XPS X-ray photoelectron spectroscopy

ZLP zero-loss peak

Contents

Chapter 1

Introduction

Since the discovery of graphene in 2004 by Novoselov and Geim [1], two-dimensional (2D) materials have emerged as an ever-growing field of research. Among others, monolayer hexagonal boron nitride (h-BN) [2], and transition-metal dichalcogenides (TMDs) [3], such as molybdenum disulfide (MoS_2) and tungsten diselenide (WSe_2), are prime examples of other heavily studied 2D materials. Their reduced dimensionality gives rise to unique physical properties that do not occur in their bulk counterparts, such as a change in their mechanical strength [4] as well as in their electronic [5, 6, 7], optical [8, 9] and thermal properties [10, 11].

Manipulation by purposefully adding impurities and lattice defects, such as dopants and vacancies can alter the materials' properties [12, 13], however, unintentional adsorption of airborne molecules or contamination originating from the sample preparation process have been shown to degrade a variety of the materials' properties. This includes their charge carrier mobility, optical transparency, as well as electrical and thermal conductivity [14]. While it has been shown that contamination can be useful at times, such as a change in the wettability of graphene by making its surface more hydrophobic [15], the effects of contamination rarely yield beneficial results in applications [16, 17, 18]. Also, the degree to which they are affected can vary from sample to sample due to the lack of control of the contamination, hampering the reproducibility in device operations [19].

This makes it desirable to keep the specimen as clean as possible, both during its synthesis and transfer, as well as during device manufacture and operation. Even though in-situ methods for sample preparation of 2D materials have been developed [20], it is still common to use ex-situ procedures, such as chemical vapor deposition (CVD), mechanical exfoliation (ME),

or molecular beam epitaxy (MBE), where the as-prepared samples are exposed to ambient conditions, either during or after the synthesis process [21, 22, 23].

1.1 Origins and effects of contamination

As 2D materials are only one to a few atomic layers thick, they possess a much larger surface-to-volume ratio compared to bulk materials. Even if the materials are synthesized with high purity, airborne contaminants such as oxygen, water (H_2O), and hydrocarbons will be adsorbed onto the sample surface within a few minutes after exposure to air [15]. As a charged impurity, oxygen has been shown to cause p-type doping in graphene through an electrochemical process in which oxygen is chemically reduced from graphene, causing electron transfer. Also, the concurrent presence of H_2O makes the resulting oxygen anions more stable, and thus more difficult to remove [24]. However, the amount of molecular oxygen (O_2) contamination seems to be much lower on free-standing graphene compared to supported graphene [25].

While determining the precise chemical composition of the adsorbed hydrocarbon chains has proven to be difficult, it is speculated that most of them consist of methoxy and carboxyl functional groups [26], methylene and methyl groups [15], alkanes with lengths of 20-26 carbon atoms [27], as well as various other C-H and C=O bonds [28]. Their presence on the surface of 2D materials can result in a decrease of the charge carrier mobility [29], and a formation of bubbles between multiple layers of 2D materials when trying to stack them, making surface cleaning an integral part of the creation of van der Waals (vdW) heterostructures [30, 31]. However, many of the hydrocarbons seem to be desorbed upon thermal annealing in vacuum upon surpassing their peak desorption temperature [32, 33].

Another type of carbon-based contamination is amorphous carbon (AC), a combination of sp^2- and sp^3-bonded carbon with no long-range crystalline order. It can result as a by-product of the CVD synthesis of graphene [14], and as part of the degradation of polymers which are introduced when transferring the sample from one substrate to another [34]. Furthermore, thermal annealing treatments can transform pre-existing carbon contamination into AC instead of removing it [35, 36], especially when annealing in non-oxidizing environments [37].

Transferring the as-grown samples onto suitable target substrates often requires specialized transfer techniques. They are typically divided into wet and dry transfer processes and can induce further contamination and defects to the transferred material. One commonly used

wet transfer process is using polymers, such as poly(methyl methacrylate) (PMMA)[1], to aid in lifting the sample from its growth substrate. However, this does typically leave residue on the sample surface [38] even after dissolving the PMMA with solvents like acetone due to the PMMA's strong vdW interaction with the sample surface [39]. This residue can have significant effects on the properties of the transferred materials. Charged impurities can act as electron scattering centers, resulting in a reduction of charge carrier mobility in graphene [18]. Also, the polymer residues can act as scattering centers for phonon scattering, causing a reduction in the thermal conductivity of h-BN [40] and graphene [41].

These problems incentivized the substitution of PMMA with other polymers [42, 43], however, many of the suggested alternatives can be hazardous to the environment, lack reliability, or their implementation is too complicated for deployment in most laboratories [44]. Hence, PMMA is still widely used due to its convenience, low cost, and time efficiency, as well as good solubility in organic solvents like acetone [45].

Dry transfer processes completely forgo the use of liquids and instead use polymeric stamps, made of materials like polydimethylsiloxane (PDMS) [46]. Here, the sample is in direct contact with PDMS, which makes use of a viscoelastic process to peel the sample off the substrate, similar to the "scotch tape" method [1], which is known to leave trace contaminants on the sample's surface [47]. Efforts have been made to coat the polymer with materials like h-BN [48] or metal-coated silicon nitride membranes [49] to reduce transfer-induced contamination. However, this introduces new problems, such as the failure to pick up the specimen from its growth substrate if the adhesion energy of the stamp material is not strong enough, as well as a lack of scalability, in addition to the creation of cracks and wrinkles [47]. Recent promising advances show the use of functional ultraviolet (UV) tapes with tunable adhesion forces, leaving the sample surface mostly free of residue [50]. However, the scalability and large-scale applications of this method are not known yet.

As silicon dioxide (SiO_2) is the most abundant contaminant in microcrystalline graphite [51], it follows that silicon impurities are ubiquitous in exfoliated graphene. While they can be removed with chemical treatments using sodium fluoride and hydrochloric acid [51], commercially available exfoliated graphene still contains trace contaminants of silicon [52]. Graphene grown via CVD has also been reported to contain silicon contamination in the form of silicates, in particular SiO_2, possibly originating from their sublimation from the quartz tube during the

---

[1]PMMA is most commonly known as acrylic.

CVD synthesis process [53]. The presence of Si directly affects the photoluminescence (PL) emission of graphene oxide as well as making it more hydrophobic, lowering its performance in humidity sensors [52]. Also, silicon is universally present in the hydrocarbon contamination described above [54, 55], and can be found as substitutional impurities in other materials such as h-BN [56].

Despite the various methods that have been developed over the last decades, no sample will be completely devoid of contamination. There is a thin film of weakly adsorbed hydrocarbons that quickly diffuse over the sample surface [57]. This mobile contamination can originate from the sample preparation, sample holder, microscope column, or the sample itself [58, 59]. When exposed to the electron beam during electron microscopy, they will dehydrogenate [60], dissociate, and undergo a cross-linking process (polymerization), eventually becoming immobile. The deposited contamination is amorphous and carbonaceous, although it also contains other elements like hydrogen and oxygen [58, 61]. This electron beam-induced deposition makes the contamination stick to the sample surface [57], and can act as a seed for further molecule attachments [62, 33, 61].

There are many more origins and effects of contamination on the characteristics of 2D materials, which makes characterizing their intrinsic properties challenging [63]. Hence, it is of importance that the samples are cleaned prior to and kept clean during the characterization process. This will strongly aid in achieving a true understanding of the inherent nature of 2D materials.

1.2   Common cleaning methods

Due to the ubiquitous presence of contamination on the surface of all 2D materials and their heterostructures, various cleaning methods have been developed over the last decades. They can typically be divided into plasma and ion beam treatments, mechanical treatments, laser treatments, and thermal annealing treatments.

During plasma and ion beam treatments, the sample is bombarded by charged particles, including ions and electrons. The charged environment allows for precise movement and acceleration of the particles using magnetic or electric fields, which can be utilized to etch the sample surface, including contamination. However, a successful etching process relies on carefully chosen parameters for the plasma energy and density, as well as treatment duration to not damage the

sample in the process [64]. While it has been shown that plasma cleaning with high-density H_2 and H_2/N_2 [28], or O_2/H_2 plasma [65] is effective in removing PMMA contamination, it can cause hydrogenation of graphene, or introduce contaminants from the sample's substrate [66, 67].

During mechanical cleaning procedures, the sample surface is scratched with a nm-sized probe, typically a tip used for imaging in atomic force microscopy (AFM) [29]. In contact-mode AFM, where the probe is in direct contact with the sample surface, the tip is dragged across the surface, causing an unzipping effect of the vdW bonds between the sample surface and the contaminants. This method can be very effective in removing many types of contamination, however, it lacks scalability in addition to making the cleaned surface prone to contamination arising from surface diffusion [61].

Laser cleaning works on the basis of laser ablation. When a sufficiently weak laser beam (to not destroy the sample in the process) hits the sample, the incoming photons diffuse across the surface, causing it to heat up. Subsequently, the contamination will evaporate or sublimate. This process of removing contaminants is similar to that of thermal annealing treatments, as the sample is heated up in the process, which is supported by similar cleaning results [68]. Furthermore, it has been shown that it can be effective in removing polymer residue on graphene by first decomposing it into monomers and low-molecular-weight gases, which are then expelled from the sample surface due to the increased temperature [69]. However, laser treatments are ineffective in cleaning large sample areas due to the narrow width of the laser beam, which is typically in the order of μm.

Thermal solutions for sample cleaning are often used in laboratories due to their rather simple installation and ease of use. Many setups also allow annealing in controlled ambient environments, such as inert (Ar, N_2), reductive (Ar/H_2, H_2) and oxidative (CO_2, air) atmospheres, as well as vacuum [64]. The surrounding atmosphere can have a drastic effect not only on the cleaning process itself but also on the integrity of the 2D material. Electrical doping [35], defect formation [68, 70], induced strain [71], and graphitization of carbonaceous contamination [72, 73] are all common side effects of thermal annealing. Inert atmospheres tend to efficiently remove carboxyl and methoxy functional groups when annealed at 400°C or higher [26], however, it can transform PMMA residue into covalently bonded amorphous carbon, which makes it difficult to remove [34, 74]. Reductive atmospheres can facilitate depolymerization of polymer residue when annealed at 400°C or higher [26], with Ar/H_2 being particularly effective in

removing residual conjugated carbon systems by hydrogenation of the C=C bonds. However, it tends to induce rehybridization of graphene from sp^2 to sp^3, resulting in amorphous carbon [75, 76], as well as strong p-type doping [35]. Also, the presence of H_2 at elevated temperatures can cause etching of graphene, compromising its crystalline integrity [77]. Annealing in oxidative atmospheres, while being effective in reducing amorphous carbon contamination [70], can cause formation of cracks in graphene at temperatures as low as 200°C [75], and still fails to remove all contaminants even at 500°C [68] when annealed in air. Also, it has been found that the annealing temperature and oxidative strength of the ambiance have a strong effect on the etching characteristics of the atmosphere, as NO_2 seems to completely etch graphene away when annealing above 500°C, while CO_2 preserves it [34].

It has been shown that thermal annealing in vacuum, while unable to remove contamination completely, seems to introduce the least amount of lattice defects to the sample compared to other thermal annealing treatments [39]. In addition, the amount of induced hole doping and strain is minimal [35, 71], while providing satisfactory cleaning results [36]. This makes it a suitable candidate for cleaning without harming the integrity of the underlying specimen. However, once the sample is exposed to ambient conditions again, contamination will quickly accumulate on its surface [15], which incentivizes keeping it in vacuum after the cleaning process. This was demonstrated in 2017 by Tripathi et al. [68] using a "pre-situ" method, where a UHV thermal treatment chamber is directly connected to a scanning transmission electron microscope, allowing cleaning and imaging of their samples without exposure to air in between. While their cleaning results seemed promising, they only reported results on graphene, and they did not quantitatively evaluate the obtained cleaning efficiency, as their unique setup limited their options in quantitative assessments.

1.3 Contamination assessment methods

Optical microscopy, atomic force microscopy (AFM), and scanning electron microscopy (SEM) can be used to determine the presence of surface modulation, including contamination [78, 30, 70]. However, distinguishing between the topological variation of the sample and the presence of contamination is not straightforward. Additionally, not all contamination manifests as a distribution of piles or bubbles, hence, these methods can fail to pick up uniform layers of flat contamination [31]. Another shortcoming is that they are unable to provide information

on the chemical composition of the contaminants. Therefore, spectroscopic methods like Raman spectroscopy and X-ray photoelectron spectroscopy (XPS) are often used to assess the cleanliness, as well as sample quality of 2D materials [36]. Still, these techniques struggle to measure very thin films of contaminants that lie flat on the sample surface.

While these techniques can determine and quantify the presence of contaminants on the surface of 2D materials, they are always probing large sample areas and are unable to determine their structure and shape on the atomic level. However, this is necessary, since vacancy sites and nanopores in the atomic lattice can act as a location for the formation of seeds arising from mobile contamination [61], which the above mentioned methods for quantifying the cleanliness of 2D materials are unable to resolve. Also, there is a lack of studies that combine the thermal annealing response of contamination with its structure at the atomic level. However, this is needed as there are applications that require controlling the sizes of graphene nanopores [79], whose evolution is affected by the local structure of adsorbed contaminants during thermal annealing treatments [80].

Hence, in this work, atomic-resolution scanning transmission electron microscopy (STEM) is combined with electron energy loss spectroscopy (EELS) to assess the cleanliness of selected 2D materials down to the atomic scale. This will provide a deeper insight not only into the cleaning effectiveness of thermal annealing in ultra-high vacuum but also into how the shape of the existing contamination changes after the thermal treatment.

Chapter 2
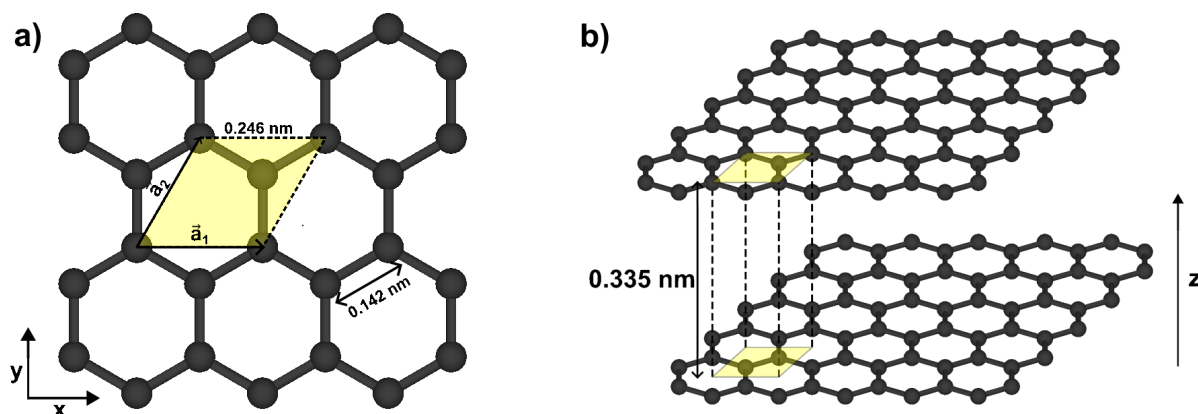
Materials

2.1 Graphene

2.1.1 Structure

Figure 2.1: **Crystallographic structure of graphene.** (a) Crystal lattice of monolayer graphene. $\vec{a_1}$ and $\vec{a_2}$ are the unit vectors of the unit cell (yellow) with a length of 0.246 nm. The carbon atoms (black spheres) are arranged in a honeycomb structure with a C-C bond length of 0.142 nm. (b) Multiple graphene layers stack in an AB configuration, where alternating layers are shifted vertically by 0.335 nm, as well as laterally by a distance that results in the center of each hexagon being occupied by a carbon atom in adjacent layers. Figures generated using VESTA.

Graphene is a 2D material made entirely of carbon atoms arranged in a honeycomb structure (see Figure 2.1a) with an electronic ground state configuration of $1s^2 2s^2 2p^2$. When carbon atoms assemble into molecules or crystalline structures, the linear combination of the $2s$ and

$2p$ (p_x, p_y, p_z) orbitals provides a higher overlap than that of two $2p$ orbitals. This results in hybridized orbitals, namely sp, sp^2, and sp^3. In the case of sp^2 hybridization, the $2s$ and $2p$ orbitals hybridize into three sp^2 orbitals, leaving one $2p$ orbital unhybridized, which results in the crystalline structure of graphene and by extension, graphite.

The three sp^2 orbitals form three covalent σ bonds with adjacent atoms with bond angles of $120°$, and the p_z orbital forms a weaker π bond that is perpendicular to the plane that the σ bonds lie in. In the case of sp^3 hybridization, all p orbitals are involved in the hybridization, resulting in tetrahedral bonds with bond angles of roughly $109.5°$, creating a metastable carbon allotrope, diamond.

The crystallographic structure of graphene is shown in Figure 2.1. Its unit cell has a hexagonal structure with lattice constants of $a = 0.246$ nm, and $c = 0.670$ nm, and a C-C bond length of 0.142 nm. Figure 2.1b shows the stacking of layers of graphene. The inter-planar distance is 0.335 nm, which is half the height of the unit cell. This is because the graphene layers stack in an AB configuration, where the layers are shifted laterally with respect to each other (in addition to the vertical shift of 0.335 nm), such that there is a carbon atom in the center of each hexagon when looking at the projection onto the *x-y*-plane. For monolayer graphene, there are a total of twelve electrons in the unit cell, four of which are occupying the $1s$ core level orbital, with the rest forming three σ bonds and one π bond, as well as the anti-bonding states three σ^* and one π^*.

2.1.2   Properties

The first Brillouin zone of the lattice in Figure 2.1a can be found in Figure 2.2a. Due to the honeycomb structure of the graphene lattice, its reciprocal lattice also shows hexagonal symmetry, with the high-symmetry points Γ, K, K' and M. Since graphene is comprised of only carbon atoms, this yields hexagonal symmetry of the lattice, resulting in K and K' becoming indistinguishable. This leads to a band gap-less dispersion relation (Figure 2.2b), where the density of states is zero at the Fermi level E_F. Also, E_F is exactly where the π and π^* bands touch, resulting in a semi-metallic behavior where the charge carriers move like massless relativistic particles due to the lack of curvature of the dispersion relation at the K point [82, 83, 84]. The strong σ bonds are responsible for the high mechanical strength of graphene, including a breaking strength of 125 GPa, as well as a Young's modulus of 1 TPa [4], which is about five times higher than that of steel [85]. The Young's modulus (or elastic
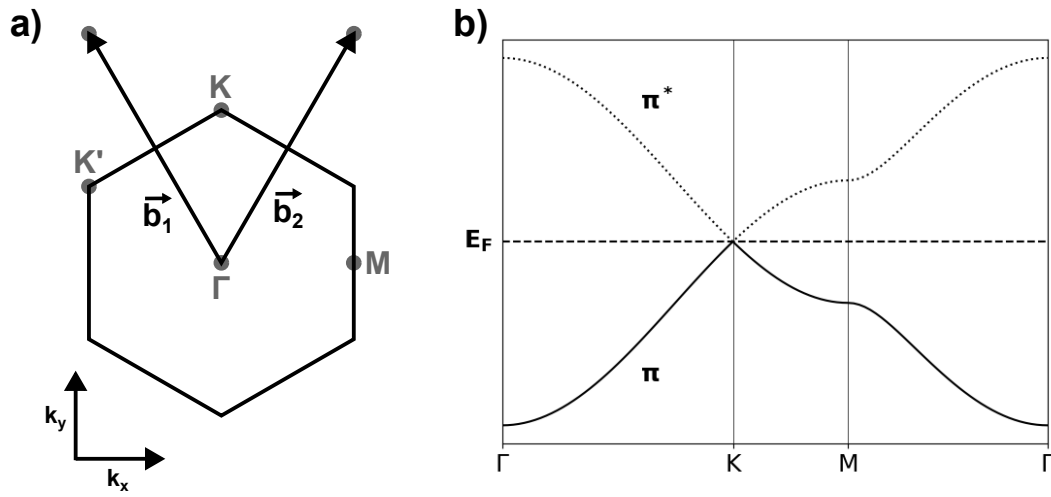
Figure 2.2: **Schematic electronic structure of graphene.** (a) First Brillouin zone of graphene. The high-symmetry points Γ, K, K' and M are highlighted, as well as the basis vectors $\vec{b_1}$ and $\vec{b_2}$ of the reciprocal lattice. (b) Band structure of the π and π^* bonds of graphene approximated using the tight-binding model. The two bands touch at the Fermi level E_F. Source code for (b) is licensed under a GNU General Public License 3.0 [81].

modulus) is a measure of the amount of stress that is required to produce a certain amount of strain in the material, making it a good measure of its stiffness.

The π bonds are much weaker and are delocalized over the entire surface. This results in novel electronic properties of monolayer graphene, including a charge carrier mobility above 200,000 $\frac{cm^2}{V \cdot s}$ at room temperature [5, 86]. Its electronic properties depend strongly on the number of layers, as well as the stacking order of the individual graphene sheets [87]. Monolayer graphene also possesses a thermal conductivity of 3000 - 5000 $\frac{W}{m \cdot K}$ [10], which is over three times higher than diamond [88], and ten times higher than silver [89]. Also, contrary to many other materials, it has a negative thermal expansion coefficient of $-7 \cdot 10^{-6}$ K^{-1} [90], causing it to contract when heated up.

Chapter 3

Methods

3.1 Scanning Transmission Electron Microscopy

In order to resolve structures at the atomic scale, microscopic techniques beyond conventional optical microscopy have to be considered. The resolution of any microscope is fundamentally limited by the Abbe diffraction limit [91, 92]

$$d \geq \frac{\lambda}{n \cdot \sin(\theta)} = \frac{\lambda}{NA} \ ,$$ (3.1)

where d is the highest possible spatial resolution, λ the wavelength of the particle that is used as a probe (photons, electrons, ...), n the refractive index of the medium the probe travels through, and θ the full convergence angle. As visible light encompasses a range of approximately 400 to 700 nm, and the numerical aperture NA is typically in the order of 1 [93], it follows that visible light cannot resolve distances d that are smaller than a couple of hundreds of nm apart. In other words, one can resolve distances that have the same (or higher) order of magnitude as the photons that are used for imaging. Since atoms and inter-atomic distances are in the order of Ångström (10^{-10} m), visible light (10^{-7} - 10^{-6} m) is not able to resolve these structures.

3.1.1 Electrons as a probe

This limitation motivated the usage of other techniques including scanning tunneling microscopy (STM), AFM, as well as electron scattering-based imaging methods such as scanning

electron microscopy (SEM), transmission electron microscopy (TEM) and scanning transmission electron microscopy (STEM). As their names suggest, the latter use electrons as a probe, which allows them to obtain much higher resolutions compared to visible light. This stems from the fact that electrons can be viewed as a wave with their corresponding de Broglie wavelength λ_{dB} [94]

$$\lambda_{dB} = \frac{h}{p} \ , \tag{3.2}$$

where h is the Planck constant and p the momentum of the electron. Assuming that their energy is dominated by the kinetic energy, p can be expressed in terms of their total energy E, taking into account that whenever an electron passes through a potential U, it obtains an energy of eU, which leads to

$$p = \sqrt{2mE} = \sqrt{2meU} \ . \tag{3.3}$$

Here, m is the rest mass of the electron and e the elementary charge. Plugging equation 3.3 into equation 3.2, the de Broglie wavelength of electrons as a function of the applied potential can be determined as

$$\lambda_{dB} = \frac{h}{\sqrt{2meU}} \ . \tag{3.4}$$

Since typical STEMs operate at acceleration voltages U between 5 kV (Low-voltage STEM) and 300 kV [95], the electrons will be accelerated to high velocities v

$$v = \frac{p}{m} = \sqrt{\frac{2eU}{m}} \ , \tag{3.5}$$

warranting relativistic corrections

$$\lambda_{dB} = \frac{h}{\sqrt{2meU}} \frac{1}{\sqrt{1 + \frac{eU}{2mc^2}}} \ . \tag{3.6}$$

Using equation 3.6, electrons that experience an acceleration voltage of 60 kV, possess a relativistic de Broglie wavelength of $\lambda_{dB} \approx 4.9$ pm, which is approximately two orders of magnitude smaller than most inter-atomic distances, allowing them to be used as a probe to image both atomic crystal lattices, as well as individual atoms themselves. However, given that the typical numerical aperture in most STEMs is two orders of magnitude smaller than 1, this theoretical limit is unlikely to be reached, even in aberration-corrected systems [96, 97].
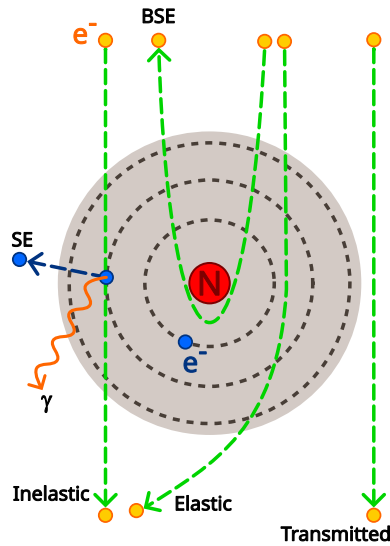
Figure 3.1: **Single electron scattering processes with an atom.** A schematic description of the different interactions and trajectories (dashed green lines) an incident electron (orange) can experience. Electrons that travel far away from the nucleus (red) are transmitted, while ones close to it have their trajectories changed, or could be backscattered (BSE) entirely. Interactions with bound electrons (blue) inside the electron cloud (grey) can result in inelastic scattering processes. A bound electron could be removed from its orbital (dashed grey line), which may result in the emission of a secondary electron (SE) and a subsequent photon (γ). Adapted from an illustration by IndianFace, licensed under a CC-BY 4.0 License [98].

3.1.2 Electron scattering processes

Particle-particle interactions that involve scattering processes are typically divided into elastic and inelastic scattering mechanisms. Elastic scattering occurs when the total kinetic energies of the interacting particles do not significantly change. One particle might lose (or gain) a minuscule amount of energy in the process, however, if this change is too small to be detected, one might still consider this interaction elastic or quasi-elastic. Figure 3.1 schematically describes possible trajectories of a free electron interacting with an atom.

An example of an elastic scattering process including electrons is an incoming (primary) electron that interacts with the electrostatic potential of an atom. Due to the attractive Coulomb force between the negatively charged electron and the positively charged nucleus of an atom, the electron will be deflected in its vicinity. It can either be slightly deflected, or completely back-scattered due to a head-on collision with the nucleus, producing backscattered electrons (BSE). Since protons (and neutrons) are around 1,840 times heavier than electrons, the displacement that the nucleus feels is much smaller than that of the electron, render-

ing this process elastic, or quasi-elastic. The process of deflecting electrons is the basis for transmission-electron-microscopic techniques, including annular dark field (ADF) imaging in STEM, where the scattered electrons are detected to obtain a contrast-based image from the amount of scattered electrons within a certain range of scattering angles.

On the contrary, if the energy of the primary particle changes when interacting with the specimen, that interaction is called inelastic. One such process is the interaction of the primary electron with a bound electron in the specimen. The latter can be knocked out of its orbital, resulting in secondary electron (SE) being emitted. The relaxation of a bound electron from a higher orbital with a now empty state in a lower one can then emit characteristic X-rays (γ), which can be used to determine the composition of the sample using methods such as energy dispersive X-ray spectroscopy (EDX).

Other forms of inelastic scattering processes include the scattering on quasi-particles like phonons, excitons, or plasmons in the specimen. Phonons are collective lattice vibrations that propagate through any crystalline structure with typical energies in the meV to low eV range, and excitons describe bound electron-hole pairs in semiconductors or insulators with energies typically below 1 eV. Plasmons, on the other hand, can possess energies that are much higher. They are delocalized collective oscillations of weakly bound electrons, and can occur in any conductive material, such as metals or semiconductors [99].

The information from the inelastically scattered electrons can be used for spectroscopic techniques like electron energy loss spectroscopy (EELS). Since the amount of energy that the primary electron loses depends on the atomic, molecular, and crystalline structure of the specimen, a chemical footprint of the sample can be obtained.

In general, both elastic and inelastic scattering are probabilistic by nature. A commonly used measure for this is the scattering cross section, which is typically given by the differential cross section σ, also known as Rutherford cross section [99]. $d\sigma$ provides a distribution over all solid angles, which can be integrated to obtain the cross section σ for a desired angular range

$$d\sigma(\theta) = \frac{Z^2 \lambda^4}{64\pi^4 a_0^2} \frac{d\Omega}{[\sin(\frac{\theta}{2})^2 + \frac{\theta_0^2}{4}]^2} \ . \tag{3.7}$$

σ describes the cross section itself, Ω is the solid angle, Z the atomic number of the atom off which the electron is scattered, λ the de Broglie wavelength of the incoming electron, a_0 the Bohr radius, θ the scattering angle, and θ_0 a parameter that takes the screening effect of the

electron cloud around each nucleus into account. This so-called screening parameter is given by [99]

$$\theta_0 = \frac{0.117 Z^{1/3}}{E^{1/2}} \qquad (3.8)$$

with E being the energy of the electron, given in keV. Generally speaking, the scattering cross section is a measure of how likely it is that an incoming electron interacts with the sample through scattering. Since σ is given in units of area, a larger σ corresponds to a larger area, increasing the chance of the electron interacting with a given atom inside the specimen, thus increasing the overall scattering intensity.

3.1.3 Scanning Transmission Electron Microscopy

In this work the Nion UltraSTEM 100 [100] located in Vienna is used. It is the centerpiece of a custom-built system called *Controlled Alteration of Nanomaterials in Vacuum down to the Atomic Scale* (CANVAS) at the University of Vienna. This system allows to transfer samples placed on conventional TEM grids between the microscope and different other devices and manipulation stages, including but not limited to an atomic force microscope (GETec AFSEM), a MBRAUN LabStar glovebox in argon atmosphere, a SPECS plasma source, a 445 nm diode laser, and a radiative heating chamber. All of these devices are connected to each other in ultra-high vacuum through standard UHV pipes (pressures usually in the 10^{-9} mbar range). Additionally, the samples can be stored practically indefinitely in UHV with pressures typically lower than 10^{-8} mbar. This system allows the user to perform atomic-resolution microscopy and spectroscopy, as well as manipulation of samples without exposing them to ambient conditions throughout the measurement procedure [101]. An image showcasing various parts of the CANVAS system is shown in Figure 3.2, and a schematic drawing of the core components in the Nion UltraSTEM 100 can be found in Figure 3.3.

While there are many different options when it comes to generating electrons, cold field emission guns (FEG) are preferred in modern STEM due to their high brightness and low energy spread. This allows chromatic aberration to be minimal and increases resolution in EELS, in particular when analyzing fine structures to get more information on the local density of electronic states [99]. A prerequisite for all STEM designs is the existence of a vacuum inside the microscope itself. If that were not the case, the electrons would scatter off of
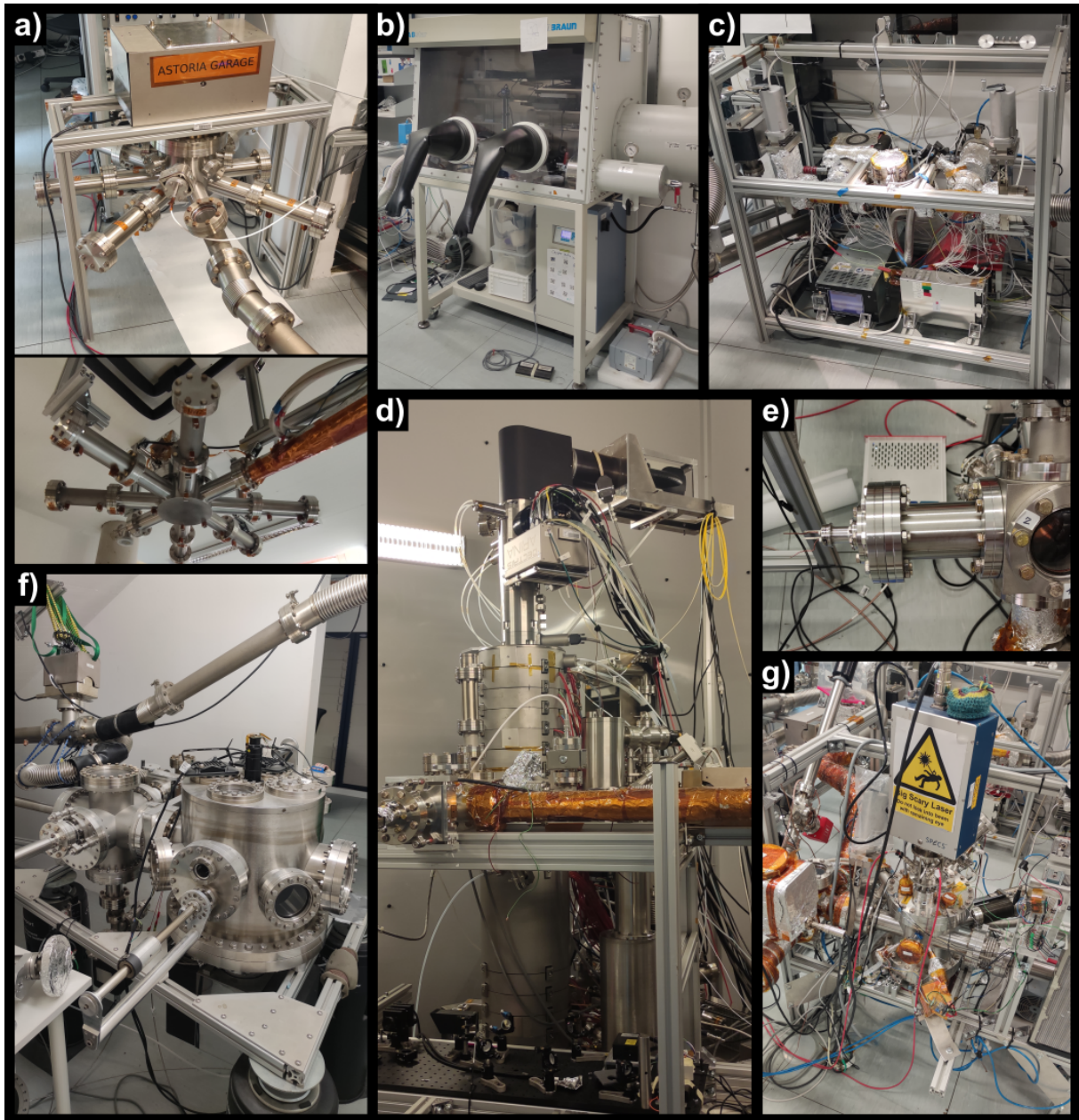
Figure 3.2: **The CANVAS system at the University of Vienna.** (a) UHV sample storages for long-term (top) and short-term (bottom) storage. (b) MBRAUN LabStar glovebox in argon atmosphere. (c) The loadlock, where the samples are introduced into the CANVAS system. (d) The centerpiece of the CANVAS, the Nion UltraSTEM 100. (e) UHV heating stage. (f) GETec AFSEM. (g) Target chamber with a variety of devices for sample manipulation.

air (or other ambient particles) before being able to interact with the specimen. The Nion UltraSTEM 100 typically has pressures in the 10^{-11} mbar range at the electron gun, and 10^{-9} - 10^{-10} mbar around the sample stage. After the electrons are emitted, they are accelerated to the desired energy using electrostatic lenses. Afterwards, they pass through an aperture which ultimately defines the convergence angle θ (see equation 3.1) and thus the theoretical
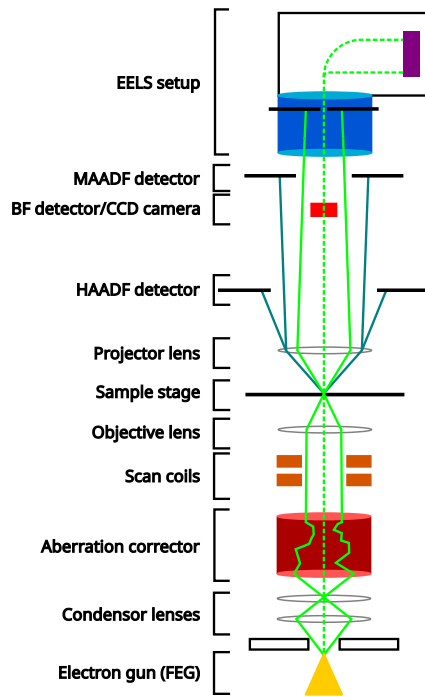
Figure 3.3: **Sketch of an aberration-corrected STEM.** A schematic overview of the used components as well as the beam path in the used STEM (Nion UltraSTEM 100). The dotted green line shows the optical axis, and the solid green line the rough trajectory of the electron beam. Electrons are generated at the bottom and pass through a set of electrostatic lenses before and after hitting the sample. The various electron detectors, as well as the EELS detector, are also outlined.

resolution limit of the setup.

The electrons then traverse through a set of condenser lenses as well as an aberration corrector. This is necessary, because, in contrast to optical microscopy, where components like lenses can be manufactured with very high precision to combat optical aberrations, non-aberration-corrected electron microscopy suffers from aberrations like spherical aberration, chromatic aberration, or astigmatism.

(Positive) Spherical aberration arises from an over-focusing of the electrons, which are farther away from the optical axis. This is showcased in Figure 3.4. The spherical wavefront (blue lines) with a maximum semi-angle β, as defined by the aperture, that emerges from the point object P at the very top of the image, turns into an aberrated wavefront (brown dotted line) after the lens focuses them. This causes the electrons that are off-axis to get focused more strongly than on-axis electrons, resulting in different focal points. The focal point corresponding to the on-axis electrons defines the Gaussian image plane (pink) at P'. However,
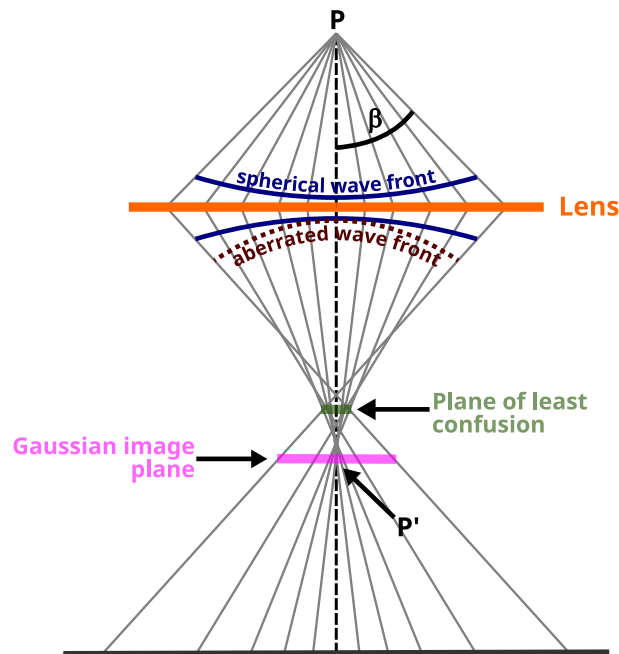
Figure 3.4: **Spherical aberration in electron microscopy.** Electrons with a maximum semi-angle β travel from the very top through an electromagnetic lens (orange). Before getting focused by the lens, they have a spherical wavefront (blue), which turns into an aberrated wavefront (brown) due to the lens interaction. They are then focused at different positions resulting in the Gaussian image plane (pink) and the plane of least confusion (green). Based on [99].

there exists the plane of least confusion (green) where the smallest image of the object is formed, and the spherical aberration is minimal. Still, it is non-zero, which results in an improper focusing on the specimen, causing the resulting image to become blurry.

Chromatic aberration can emerge when the electron beam is not monochromatic, i.e., the electrons do not possess the same energy. A difference in their energy, and thus velocity (equations 3.3 and 3.5), will manifest in different trajectories when exposed to a magnetic field (equation 3.9), causing them to not be focused onto the same spot. Even though the Nion UltraSTEM 100 is not equipped with a monochromator, the energy spread of its cold FEG is small enough ($\Delta E \approx 0.5$ eV) for it to not be the limiting factor with regard to resolution.

Astigmatism can occur when the electrons pass through an asymmetrical magnetic field. This results in different focusing along different axes, resulting in the image appearing to be stretched out in one direction, at least for relatively small astigmatisms. However, this is rather easy to correct using octupole lenses that create magnetic fields that compensate for the non-uniformity of the others [99].

In essence, all aberrations arise from imperfect focusing of the electron beam and play a major role in the practical resolution limit in electron microscopy. Hence, to improve the resolution, a set of aberration-correcting lenses is installed [102], which counteract the positive spherical aberration the electron beam experiences due to being shaped by magnetic lenses. The Nion UltraSTEM 100 is equipped with an autotuning algorithm, the AutoSTEM X, that can, in principle, combat aberrations up to the fifth order [103].

Contrary to TEM, where a large sample area is showered by electrons at once, in STEM the electrons must be focused onto the sample surface. The focused probe then scans over a selected area of the specimen, creating scattering centers at each probe position, from which the scattering information is used to create the image. The focusing of the electron beam is achieved by an objective lens, while the movement of the beam across the surface is handled by a set of scan coils. They deflect the beam via the Lorentz force $\vec{F}$

$$\vec{F} = -q(\vec{E} + \vec{v} \times \vec{B}) \ , \tag{3.9}$$

where q is the charge and $\vec{v}$ the velocity of the electron, $\vec{E}$ the electric field and $\vec{B}$ the magnetic field. Looking at equation 3.9, it can be seen that the electrons experience a force perpendicular to the magnetic field $\vec{B}$ and direction of movement given by $\vec{v}$. This implies that electrons that are already traveling parallel to the magnetic field, experience no force $\vec{F}$ at all (at least none that can be attributed to the magnetic field), while ones that do not, are deflected.

After the probe interacts with the sample through scattering processes (as described in Section 3.1.2), the projector lens spreads the beam such that the electrons can be collected by the various detectors towards the top of the microscope. Since the information about the sample structure lies in the scattering angle (and intensity) of the electrons, different detectors can be positioned at different locations. Along the optical axis, both a bright-field detector as well as a charge-coupled device (CCD) camera (Ronchigram camera) are located. The former can measure the amount of transmitted (forward scattered) electrons, while the latter takes digital images of a luminescent film, which was hit by said electrons. Dark-field detectors, such as medium-angle annular dark-field (MAADF) or high-angle annular dark-field (HAADF) detectors possess a ring-like (annular) shape and are positioned further away from the optical axis. The MAADF detector covers a semi-angular range of 60 - 200 mrad, and the HAADF detector covers 80 - 300 mrad. They measure electrons that had undergone scattering pro-

cesses with the specimen that correspond to scattering angles within the specified angular range. In addition, their annular shape allows them to measure integrated intensities at each probe position. Both operate on the principle of a scintillator and a photomultiplier. After the detector gets hit by electrons, the scintillator converts them into photons, which are then multiplied by the photomultiplier in order to amplify the signal.

The choice of ADF detector typically depends on the studied specimen, as the scattering intensity depends greatly on the atomic number Z due to the Coulomb interaction, empirically given by the Z-contrast, which is $\sim Z^{1.7}$ in the case of HAADF imaging [104, 105]. From this, it follows that scattering on lighter atoms (less positively charged nuclei) produces lower contrast in the image compared to scattering on heavier atoms. Hence, it is typically more beneficial to use MAADF to study lighter atoms (e.g., carbon, boron, nitrogen), and HAADF for heavier atoms (e.g., molybdenum, tungsten, sulfur). Since the measured scattering intensities depend on the total scattering the probe went through at each position, the information that can be obtained through the Z-contrast can vary greatly depending on the thickness of the sample. This phenomenon is often referred to as mass-thickness contrast. Multiple scattering events cause more electrons to be scattered off the optical axis, increasing contrast at larger total scattering angles [99], which can then be collected by ADF detectors. Very contaminated samples, for instance, can display a strong difference in contrast between clean and contaminated areas, with most of it coming from the numerous scattering processes that can arise due to the many layers of contaminant atoms the probe passes through.

3.1.4   Electron Energy Loss Spectroscopy

At the top of the microscope, the Nion UltraSTEM 100 is equipped with an electron energy loss spectrometer, namely a Gatan electron energy loss spectrometer with an Andor iXon Ultra 897 electron-multiplying charge-coupled device (EMCCD) camera with a collection semi-angle of 35 mrad. As not all electrons have the same energy (and thus velocity) after they interact with the sample due to inelastic scattering processes, the electrons can be dispersed by the magnetic field at the top of the microscope column per the Lorentz force (equation 3.9) as well as the centripetal force

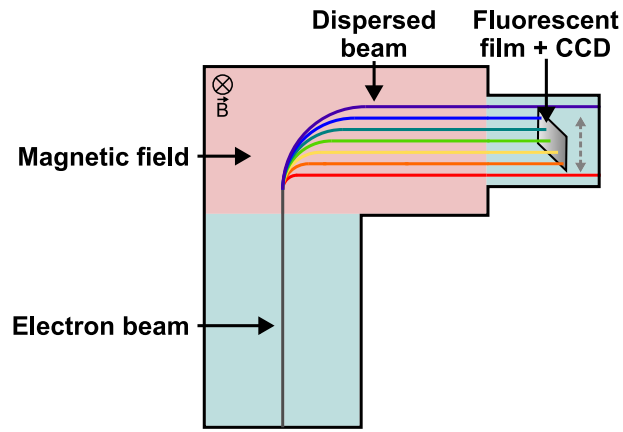$$\vec{F} = \frac{m\vec{v}^2}{r} \ , \tag{3.10}$$

Figure 3.5: **Working principle of an electron energy loss spectrometer.** When the electron beam (grey line) enters the magnetic field (pale red), the beam will be dispersed in accordance with the Lorentz force and centripetal force. The color bands correspond to the energies of the electrons, akin to that of visible light. The most energetic electrons are displayed in purple, while the least energetic ones are red. The dispersed beam then hits a fluorescent screen, which is captured by a CCD camera.

where r is the radius of the circular trajectory, m the mass of the electron, and $\vec{v}$ its velocity. Equating equation 3.9 and 3.10, and assuming that the magnetic field $\vec{B}$ is perpendicular to $\vec{v}$, gives the following relation

$$r = \frac{mv}{qB} \; .$$
(3.11)

Here, v and B are the magnitudes of the velocity $\vec{v}$ and magnetic field $\vec{B}$ respectively. Since all electrons possess the same mass m and charge q, it becomes clear that the radius r by which they are deflected depends only on their velocity v, as long as the magnetic field strength B is kept constant. This allows the electrons to become dispersed and be used for EELS. This process is schematically presented in Figure 3.5.

After the dispersion takes place, the electrons hit a fluorescent screen, which is then captured by the CCD camera. Since the strength of the magnetic field in the spectrometer can be changed, it is possible to only look at a selection of the entire spectrum, or capture finer or broader structures.

The most dominant feature in a typical EELS spectrum is the zero-loss peak (ZLP) centered at 0 eV, which results from electrons that have not undergone inelastic scattering, and thus retained their energies. It is usually many orders of magnitude more intense than any other

feature in an EELS spectrum since most of the electrons interact with the (thin) specimen without losing energy in the process. The energies lost by the incoming electrons due to inelastic scattering interactions with the sample form the other features. The low-loss region of an EELS spectrum, which typically corresponds to energy losses below 50 eV, is comprised of features originating from phonons, excitons, and plasmons. Due to the low energies of phonons and excitons, it is not possible to resolve them without a monochromated electron source, as they would be hidden within the width of the ZLP, which is defined by the energy spread of the source (here $\Delta E \approx 0.5$ eV). Plasmons, however, occur at higher energies in the low-loss regime, and are usually the most prominent peak there, besides the ZLP itself.

After the plasmon peaks, core loss features start to emerge. These core loss edges correspond to the ionization energies of bound inner-shell (core) electrons. The strongly bound core electrons can be promoted to a higher energy state, such as bound states above the Fermi level (corresponding to anti-bonding states) or free electron states above the vacuum level. By comparing the measured spectra to reference values from databases such as the EELS Atlas [106], the positions of the ionization edges can be used to determine the chemical composition of the specimen [107]. Since the energies the electrons lose in this process not only correspond to the energy level of the bound electrons but also the type of bonds in the material, it is possible to also get information on allotropes of a given element [108]. To obtain elemental information, a background subtraction has to be done. While the detector itself will contribute to the background, the majority comes from the high intensity of the ZLP, which can extend even to high energy losses.

The Nion UltraSTEM 100 is also capable of performing sequential measurements of EELS spectra across adjacent positions on the sample, creating spatial maps of EELS spectra ("EELS maps"). All pixels in the image record a spectrum, which combine into elemental composition maps that can complement the data obtained by ADF measurements to provide further insight into the sample composition. The size of the pixels has to be taken into consideration since the spatial resolution of EELS is not only limited by the size of the probe at each probe position but also by the scattering cross section of the specimen.
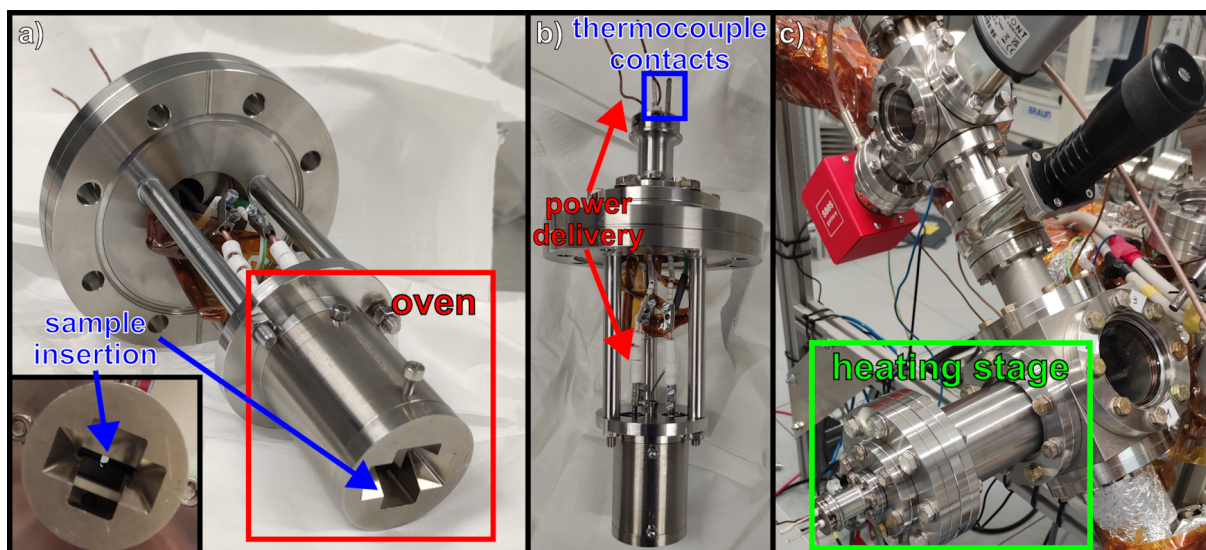
Figure 3.6: **UHV heating stage.** The custom-built heating stage used in this work. (a) The oven into which the sample is inserted into possesses a cylindrical shape and is responsible for the heating process. (b) The tungsten wire as well as the thermocouple inside the oven are connected to the feedthrough at the back of the chamber. (c) The assembled heating stage installed in the CANVAS system.

3.2 UHV heating stage

To thermally anneal the samples, the UHV heating stage (base pressure 10^{-8} - 10^{-9} mbar) integrated within the CANVAS system at the University of Vienna is used. It is specifically designed for this thesis and can be used in future projects to thermally anneal samples if desired. Design sketches and measurements of the heating stage can be found in Appendix A.

The direct connection to the CANVAS system allows to transfer samples between the heating stage and the Nion UltraSTEM 100 while remaining in UHV. The samples are placed onto rectangular "pucks", and up to three can be stored within a "car" [101]. To remove the puck from the car and insert it into the heating stage, the puck is taken out with a gripper arm that can extend to the heating stage, where it is released.

Figure 3.6 shows the assembled heating stage. The oven itself contains a 3D-printed Al_2O_3 (aloxide) ceramic that holds the titanium puck, which holds the sample. The aloxide oven was provided by Lithoz GmbH, who printed it free of charge for us. Aloxide was chosen due to its high melting point of above 2,000°C as well as electrically insulating properties [109]. The oven also has space for a V-shaped tungsten filament with a diameter of 0.5 mm, which is responsible for the heating process via resistive heating (Joule heating). It is positioned slightly

out of sight of the sample area, to prevent potential residual material coming off the W wire to deposit onto the sample, as well as to avoid locally high temperatures on the sample surface. The distance between the tip of the wire and the sample is approximately 2 - 3 mm. Using a K-type thermocouple from TMH GmbH, which was chosen due to its wide temperature range, good sensitivity, and affordability, the temperature is measured at a spot on the puck close to the sample. The thermocouple is mineral-insulated and ungrounded, where the alumel and chromel spot-welded leads (hot junction) are not exposed at the tip but are connected inside the shielding. This design results in lower response times, however, this was not deemed to be the limiting factor due to the slow nature of thermal radiation and low thermal conductivity of the titanium puck [88].

The oven is encompassed by a cylindrical stainless steel frame. Stainless steel was chosen for its poor thermal conductivity [88], which reduces the amount of heat leaving the oven through conduction. Two holes on one of the flat sides of the cylinder are filled with screws made from stainless steel that push the tungsten filament onto the aloxide, securing it in place. To ensure that these screws are not in direct contact with the cylinder itself, ceramic beads are put around the screws. This is necessary because said screws also provide an electronic connection to the tungsten filament.

The cylinder is secured onto a circular stainless steel plate with a width of 6 mm. The purpose of this plate is to allow for adjustment of the positional alignment between the oven and the gripper arm. Using three threaded rods, this plate is screwed onto a reducing flange at the back of the heating stage, where the feedthrough for the thermocouple, as well as the power delivery to the heating filament, is positioned.

3.2.1 Proportional-integral-derivative controller

The heating stage contains many parts that are made of different materials including stainless steel, aloxide, titanium, tungsten, and copper, each with its own heat capacity, thermal conductivity, and thermal expansion coefficient. This makes modeling the heating process and the obtained thermal energy on the sample challenging. Hence, a proportional-integral-derivative (PID) controller is used to control the temperature.

A PID controller is a control loop algorithm that continuously calculates the difference (error) between the currently measured value and the target value (setpoint) of the process variable
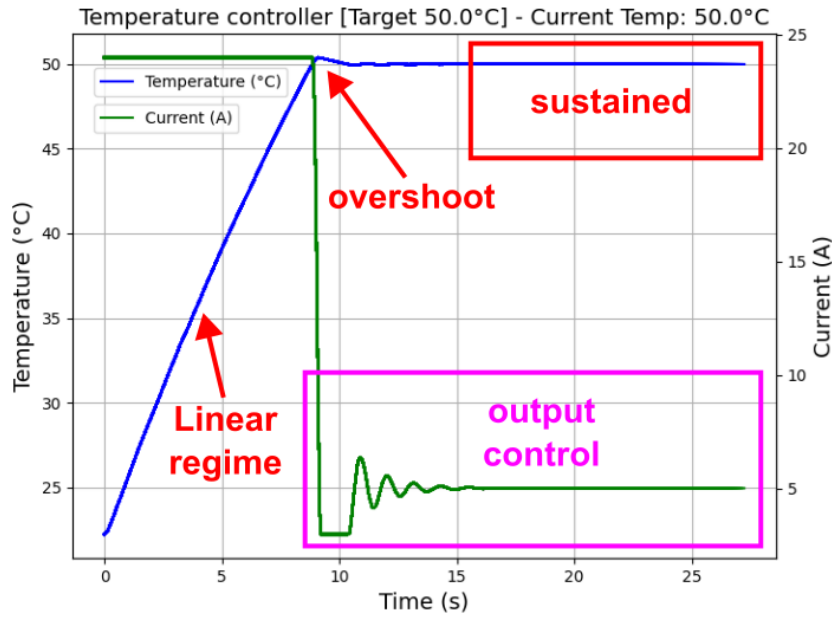
Figure 3.7: **Simulated temperature control using a PID controller.** The process variable (temperature, blue) is controlled by the output variable (current, green). The temperature rises under a constant current until it gets close to the setpoint (50°C). Then, the PID controller controls the current (pink box) such that the temperature remains at the setpoint.

(PV) to provide an output value that controls PV. The goal of this algorithm is to minimize this error over time so that a steady state at the setpoint is achieved, described by

$$u(t) = K_p e(t) + K_i \int_0^t e(\tau) \, d\tau + K_d \frac{de(t)}{dt} \ . \tag{3.12}$$

Here, $e(t)$ is the measured error at time t, and K_p, K_i, and K_d are the (non-negative) numerical coefficients that have to be provided to the controller algorithm. K_p is proportional to the present error, meaning that the control output $u(t)$ will be larger, the larger the difference between the current value and target value is. K_i considers all past errors and is often required to reach a steady state. When the setpoint has been sustained for some time, the integral term in equation 3.12 will stop growing, and the control output will remain constant. The derivative term is proportional to the current rate of change. This information is used to attempt to reduce the future error. Assuming the coefficients are chosen properly, $e(t)$ will eventually tend towards zero, resulting in the proportional and derivative terms to approach zero, and the integral term to become constant. This causes the the output $u(t)$ to be constant too, and the system to reach an equilibrium state. A more detailed breakdown of PID controlling algorithms can be found in [110].

In this work, the process variable is the temperature T, and the output value is the current I provided by the power supply. The current was chosen over voltage as it was found to be more stable. Figure 3.7 shows a simulated example of a PID-controlled process. During the heating process, the temperature rises until it approaches the target temperature of 50°C. Then, the temperature may slightly overshoot the setpoint before it starts to oscillate briefly. Then, it enters the sustained regime, where it remains almost constant due to the control output from the PID controller continuously adjusting the current that is supplied to the tungsten filament. Eventually, the system reaches an equilibrium state, where the supplied heating power is equivalent to the dissipated heat.

3.3   Methods for data analysis

3.3.1   Image thresholding and segmentation

To assess the cleanliness of the samples, contrast-based image processing and analysis based on thresholding is used. Image thresholding and subsequent segmentation is a form of digital image processing that converts an image with a given contrast value distribution, be it grey-scale or color, into a binary image (black and white). Figure 3.8 showcases this process on a sample image. Since contaminated sites are thicker than clean areas, they produce stronger contrast during ADF measurements in STEM compared to thinner areas (mass-thickness-contrast, see section 3.1.3). When performing annular dark-field (ADF) imaging, this results in the contamination appearing as brighter ("more white") than clean areas, which appear as "more black" in grey-scale images. This method has been used in recent literature [14, 70] to quantify the relative clean area of selected patches of graphene samples.

Any digital grey-scale image (see Fig. 3.8a) assigns a contrast value to each of its pixels, with the distribution of those values ranging from the minimum (darkest) contrast value present in the image to a maximum (brightest) one. This can then be normalized such that all contrast values lie between 0 (black) and 1 (white)[1]. One has to choose a (normalized) contrast value between 0 and 1 and assign it as the threshold for the thresholding process. All pixels with contrast values below the threshold are assigned a contrast value of 0, i.e., black, while all pixels above it are white, with a value of 1, creating a binary image (Fig. 3.8e).

---

[1]This step is not strictly necessary, but it makes it easier to compare thresholds for different images.
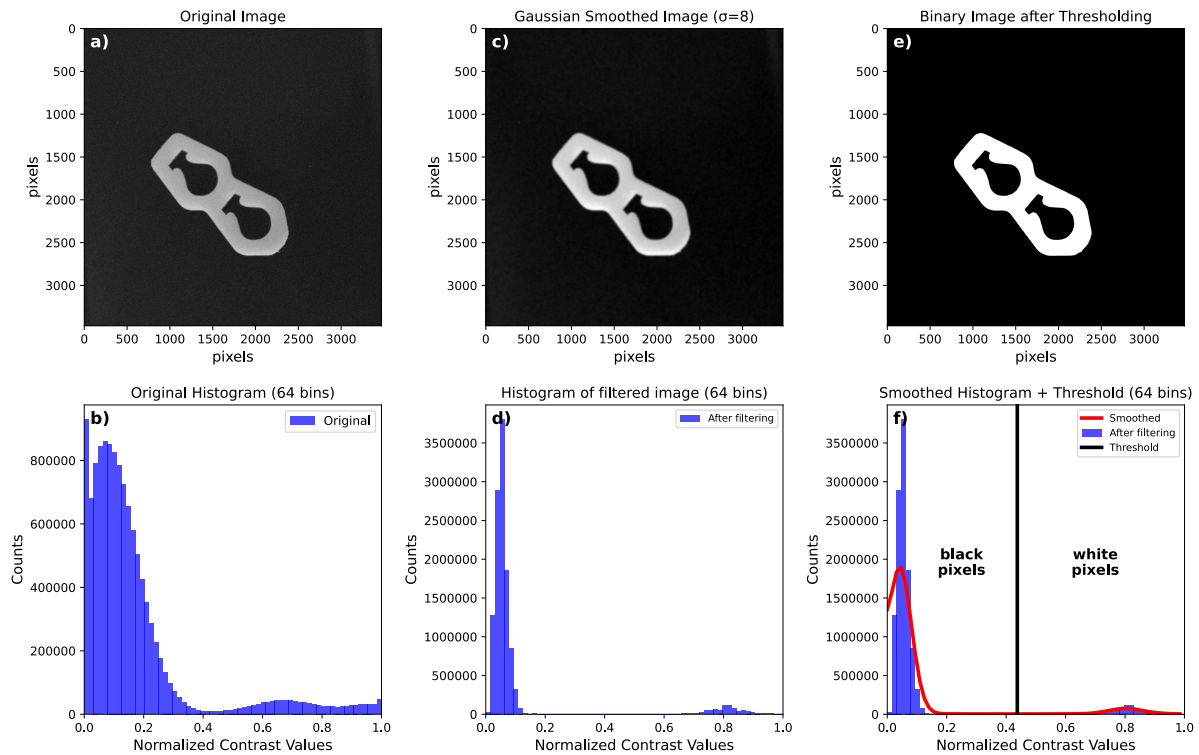
Figure 3.8: **Showcase for the thresholding and segmentation process.** The original image (a) possesses a corresponding contrast intensity histogram (b). After applying a Gaussian filter in (c), the shape of the histogram (d) is changed. Afterward, the histogram is smoothed (red) to determine a useful threshold (black vertical line) via the minimum method (f). In the corresponding binary image (e), all pixels with contrast values below the threshold are now black, and the ones above are white. The original image in (a) shows a photograph of a part of a zip tie, taken with a phone camera.

While thresholds can be chosen manually, this can introduce observer bias, and this process typically does not scale very well as it can be quite laborious. Hence, automated thresholding methods may be used, in particular for large sets of images. While these automated methods can still introduce bias, the benefits of their scalability typically outweigh the cost of minor bias.

One common way to display the contrast values is using a contrast intensity histogram (Fig. 3.8b). It shows the abundance of contrast values from the original image within each interval, or "bin". However, it has to be kept in mind that histograms are not unique. Not only can the number of bins change the shape of the histogram, a histogram is also not invertible, i.e., two identical histograms could originate from two completely different images. Nevertheless, histogram-based image processing is widely used for partitioning and segmentation [111], if one

assumes that the information in an image is given by different contrast values. Furthermore, a histogram alone cannot determine which part of the image is foreground or background, the original image itself has to be taken into account.

Common thresholding methods

The histograms of typical grey-scale images have either a unimodal, bimodal, or polymodal contrast distribution. This means that they contain one, two, or multiple peaks respectively. Depending on the shape of the histogram, different methods for thresholding can be deployed. Commonly used methods include Otsu's method, the triangle method, and the minimum method, as well as thresholding based on statistical parameters, such as the mean, median, or standard deviation, with each of these methods holding its own advantages, disadvantages, and limitations [112].

Otsu's method functions by calculating the variance of both foreground and background pixels and adding them together for all potential thresholds between 0 and 1. The contrast value for which this sum is the smallest is then chosen as the global threshold. This works well for bimodal histograms, especially if both peaks are quite narrow, however, it struggles with very noisy images as well as ones where the foreground and background are not easily distinguishable [113].
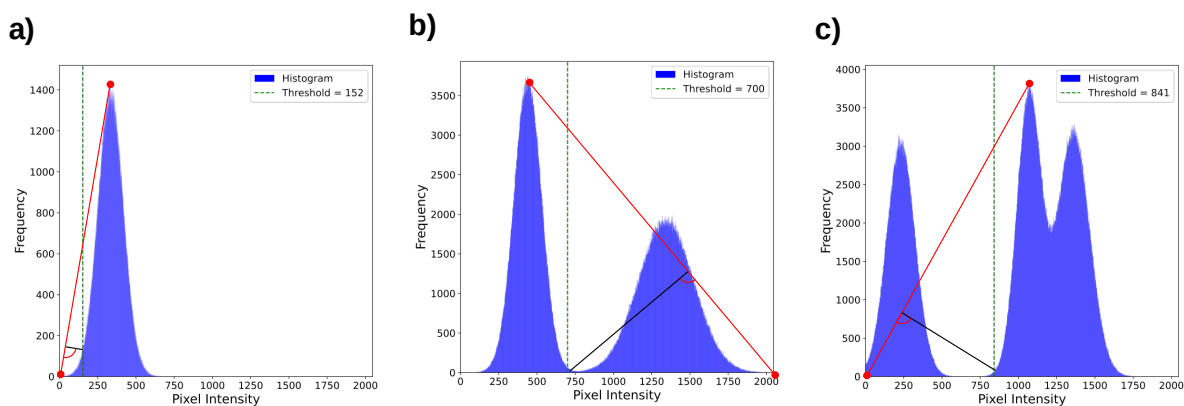
Figure 3.9: **Geometrical demonstration of the triangle method.** The red line connects the top of the highest peak of the histogram (blue) with the last (or first) bin that contains any pixels, and the black line is then drawn perpendicular to the red line. The threshold is the corresponding bin (on the x-axis) where the black line intersects with the histogram. It can successfully determine thresholds for (a) unimodal, (b) bimodal, and (c) polymodal histograms. Based on [112], licensed under a CC-BY 4.0 License.

Another thresholding method is the triangle method. A geometrical description of this method can be obtained by drawing a line from the top of the highest peak to the last (or first) bin that contains any pixels. Then, a perpendicular line is drawn towards each position of the histogram on one side of the peak. Maximizing this distance then defines the threshold. Figure 3.9 shows three sample histograms to demonstrate the method (adapted from [112]). In essence, it tries to estimate the base of the peak, and works quite well for unimodal histograms, along with polymodal histograms with one very dominant peak. However, it can fail to determine useful thresholds for polymodal histograms with peaks that are similar in height.

The minimum method, which is used in this work, functions by determining the position of two peaks in the histogram and then calculating the minimum of the histogram between said peaks. The corresponding contrast value is then picked as the global threshold. Figure 3.9 demonstrates three sample histograms that this method is applied to (adapted from [112]). This method works well for bimodal histograms (Figure 3.10 left, right), as it not only requires at least two peaks but is also oblivious to their shape, as long as two peaks can be identified. While this method can be used for images with a corresponding histogram that contains more than two peaks, prior information about the image is necessary. For example, if it is known that the threshold should be between the third and fourth peaks, the minimum method works excellently, as all peaks aside from the third and fourth can be ignored. It obviously fails if there is only one peak to begin with (Figure 3.10 center).
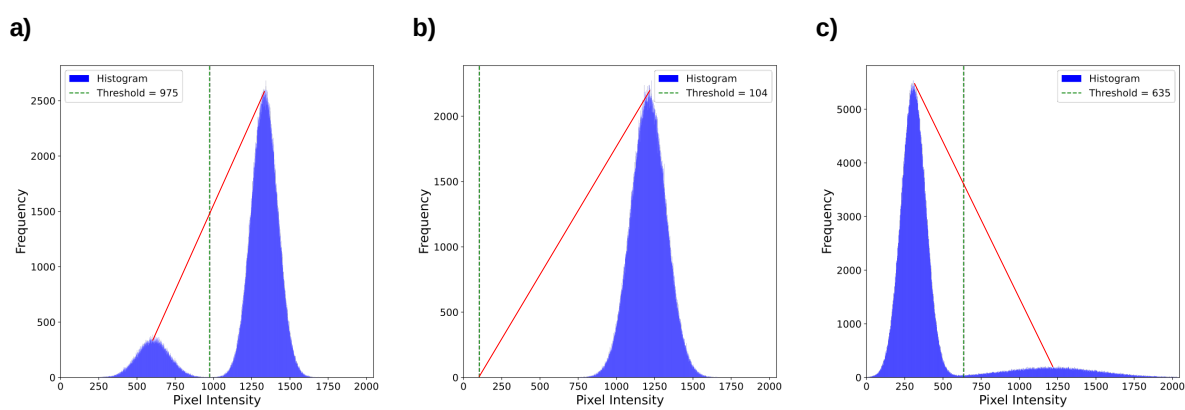
Figure 3.10: **Graphical demonstration of the minimum method.** The histogram is shown in blue, where the red line connects the top of the peaks. the green dashed line signals the position of the threshold. It can successfully determine thresholds for bimodal (a, c) histograms, but fails for unimodal (b) histograms. Based on [112], licensed under a CC-BY 4.0 License.

Image filters

In general, before using a thresholding method, it can be beneficial to apply filters to the image (Fig. 3.8c). This will lead to changes in the histogram (Fig. 3.8d), allowing for the discussed automated methods to work more effectively or to work at all. Many image filters function by applying a filter kernel to each image. A kernel is a small subregion of the image laid out as a matrix with a predefined size, containing the filter coefficients. To apply a filter to the image, the kernel is centered over each pixel in the image and a filter operation is applied. A mean filter simply calculates the arithmetic mean of this matrix, and assigns it to the central pixel. Weighted filters multiply each pixel value in the matrix with the corresponding filter coefficient and assign the result to the central pixel of the image. This process is then carried out for each pixel. Filters like median filters reduce unwanted noise, while Gaussian or Lorentzian filters also blur the image (particularly edges) and enhance foreground structures while diminishing background information. This is because they are weighted filters, which give more importance to the central pixel of the filter kernel.

This can make distinguishing between the foreground and the background easier, as the Gaussian (or Lorentzian) blur increases the number of pixels with intensities closer to the mean values of the background and foreground structures at the cost of reduced contrast in the image. Thus, pixels with intermediate values are changed to values closer to either the background or foreground (see Figure 3.8b and d). The efficacy and possibly introduced bias of these filters depend on carefully chosen parameters. Using overly aggressive ones can blur the image too much, diminishing the amount of information that can be obtained, while choosing filters that are too mild can have next to no effect at all. In addition, carelessly using filters can introduce data to the image that had not been previously there, completely invalidating the information itself.

Another method to prepare images for thresholding is to smooth the histogram itself (Fig. 3.8f, red line) by either averaging the intensities of neighboring bins or applying weighted filters to each bin. This is different from applying filters to the image directly, as the actual contrast value for each pixel remains unchanged, as long as the smoothed histogram is not applied to the image. Some of the noise and minor spikes in the histogram are reduced, while the general shape of the distribution is retained. This smoothing can make it easier for automated thresholding methods to determine their respective thresholds without changing the information in the image in the process.

3.3.2 Morphological operations
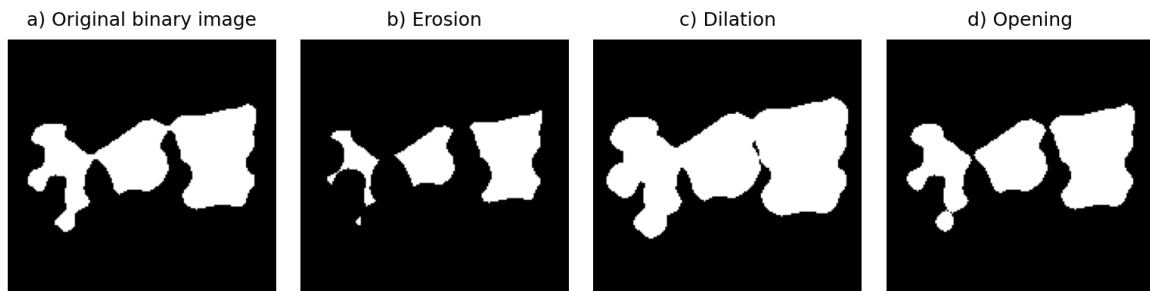
Figure 3.11: **Morphological operations: Erosion, Dilation, and Opening.** The binary image in (a) is eroded in (b) and dilated in (c). (d) Shows the effects of erosion, followed by dilation of the eroded image. Of note is that the patches are now separated when compared to (a).

Regardless of the thresholding method, in the end, one will obtain a binary image (Fig. 3.8e) that consists of only black and white pixels. The original image is now segmented into foreground and background and can be used for further image processing and analysis.

If the obtained binary image contains features that should be omitted due to their size and/or shape, procedures that are based on connectivity, such as opening and area opening can be used. Opening is a process that first erodes the image and then dilates it (see Figure 3.11). Erosion effectively shrinks connected areas in the picture by turning a foreground pixel into a background pixel if any of the pixels in a defined range (kernel) around it are background pixels. Dilation does the opposite. The presence of any foreground pixels within a given area will turn all pixels in that area into foreground pixels, causing connected areas to become larger. This can result in neighboring connected areas merging if they are only separated by a small distance. By combining erosion with subsequent dilation, barely connected areas are split apart. This is because the erosion process causes very small or thinly connected patches to be completely removed from the foreground. Thus, upon dilation, they cannot appear again. The barely connected objects that were separated by erosion, will not be connected again by the dilation process, effectively separating them. Larger connected areas in the image are re-sized to their approximate original size, with a minor change in their shape due to the geometry of the kernel.

Area opening makes direct use of the concept of connectivity in digital image processing. Pixels count as connected pixels if they have the same contrast value and are immediately beside each other. For two-dimensional images, one generally distinguishes between 4-connectivity
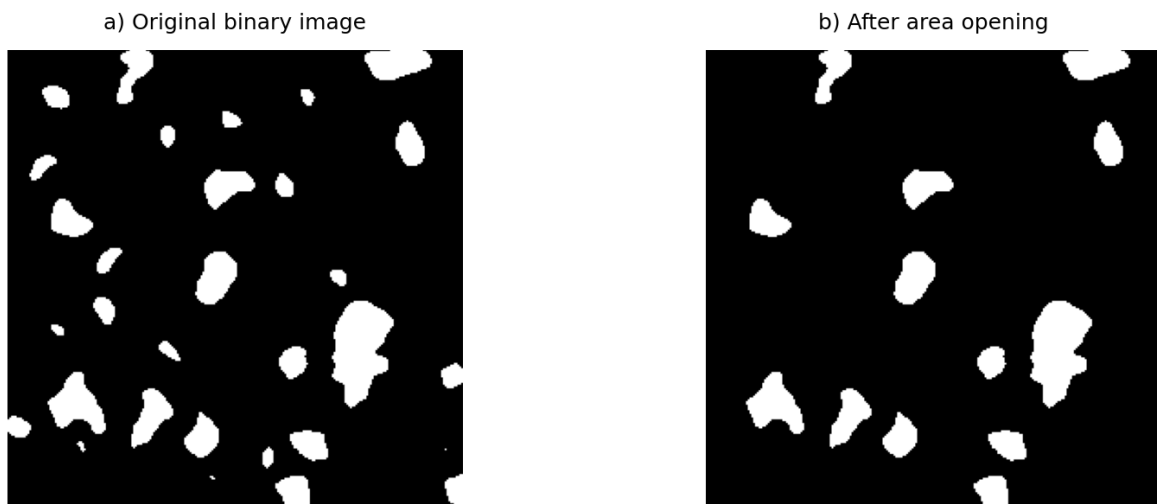
Figure 3.12: **Filtering based on connectivity: Area opening.** (a) Shows a binary image with multiple connected white areas surrounded by black pixels, which are filtered out in (b) by labeling them via 8-connectivity and choosing a suitable size threshold.

and 8-connectivity. 4-connectivity only considers pixels that are vertically and horizontally adjacent (4 pixels in total), while 8-connectivity also allows pixels that are diagonally adjacent (8 pixels in total). Depending on the original image as well as the choice and strength of the applied filters, the resulting binary image may contain connected foreground pixels that are encapsulated by background pixels (or vice versa). An example of this can be seen in the binary image in Figure 3.12a, where multiple small white patches (foreground) are surrounded by black pixels (background). If one considers some of these areas not to count towards the foreground due to their small size, but should instead be assigned the pixel value corresponding to the background, connectivity-based filtering can be applied. This method is commonly used in particle analysis, where particles that are too small (or too large) are sometimes not considered for further data analysis and are thus turned into background pixels. If the number of connected pixels is smaller than a predefined size, their corresponding contrast values are changed to those of the background, effectively eliminating them from the image [112].

The digital image processing steps used in this work are summarized in Figure 3.13. The original image (Figure 3.13a) shows an electron microscopy image, containing clean (darkest contrast) and contaminated (brighter contrast) areas of a 2D material. They are taken at a resolution of 2048x2048 pixels, with a field of view (FOV) of 128 (or 256 nm, depending on the amount of present contamination). First, a Gaussian filter ($\sigma = 1$ px) is applied to the whole image (Figure 3.13b) to blur the edges between the contaminated and clean areas, as well as adjust the contrast in the image, which aids in determining the threshold between
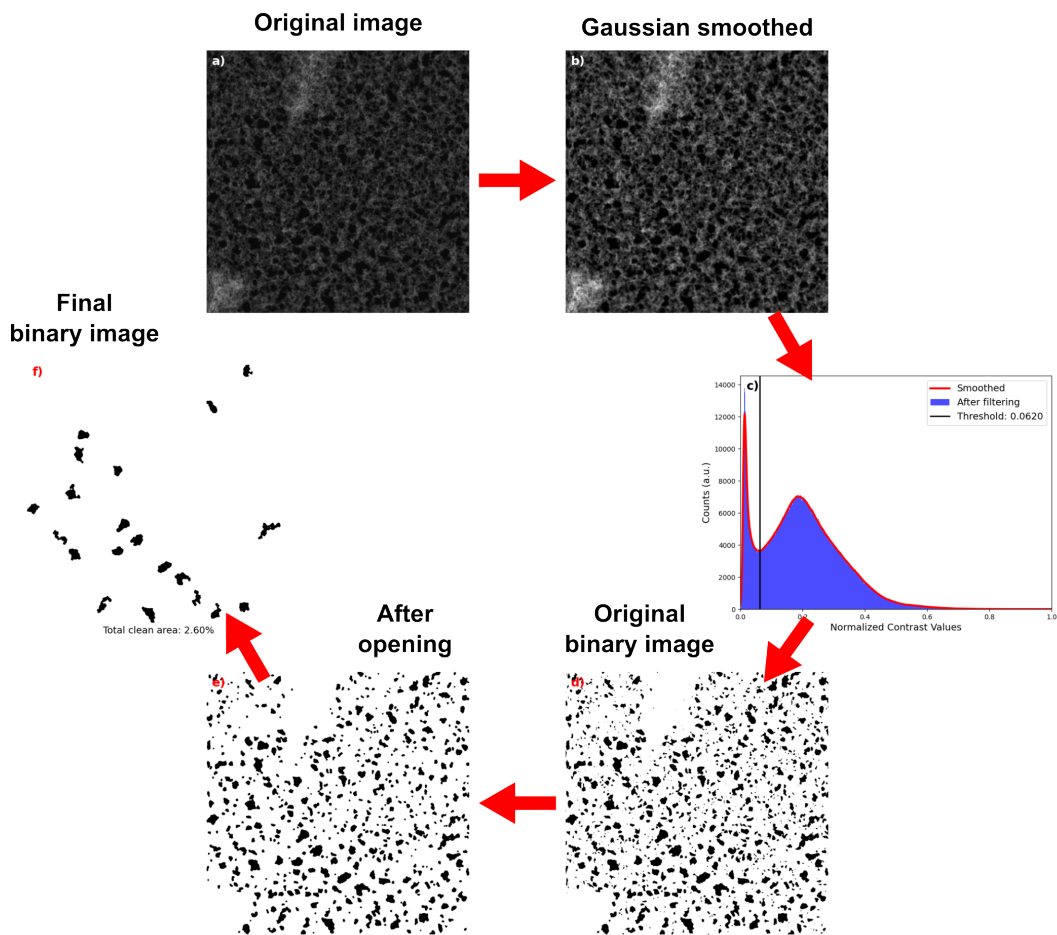
Figure 3.13: **Summary of the used digital image processing steps.** The original image in (a) is filtered using a Gaussian blur in (b). The contrast intensity histogram of (b) is then generated in (c) and thresholded (black line) based on the minimum method following a smoothing (red line) of the histogram (blue), which results in the binary image in (d). Then, opening is applied in (e), followed by area opening in (f), which yields the final binary image.

the background and foreground structures. A σ of 1 px is chosen to keep the blurring effect minimal while still separating the corresponding histogram's peaks. The obtained histogram is used for thresholding using the minimum method (Figure 3.13c), where it is first iteratively smoothed (red line) until only two peaks remain. The smoothing is carried out by applying a one-dimensional Gaussian filter ($\sigma = 1$ bin) to the intensities in each bin. This smoothing process is recommended to ensure the automated thresholding process is more consistent across different images. The obtained binary image from the thresholding and segmentation process (Figure 3.13d) is then subjected to the opening process (Figure 3.13e) to remove small areas as well as separate barely connected structures. The radius of the disk for the opening is 6 px (or 3 px). This results in connected areas that are smaller than approximately three lattice constants in graphene to be removed from the image. Lastly, area opening is applied

to the whole image where the remaining small areas that are smaller than 16 nm^2 are removed (Figure 3.13f). This size is chosen since areas as small as around 2x4 nm^2 have been used in literature to perform quantitative analysis on graphene [114]. However, since the shape of the clean areas (thin and elongated versus more spherical) strongly affects the usefulness of the patch despite potentially having equal areas, a size equivalent to 4x4 nm^2 is chosen. This then yields the final binary image that will be used for further data analysis, including the calculation of the relative clean area in each image, as well as statistics regarding the sizes of the clean patches.

3.3.3 EELS images

When recording EELS maps, as described in section 3.1.4, each pixel in the scan map contains an EELS spectrum. In each spectrum, the integrated intensity over all energy channels provides the contrast value for the respective pixel. Depending on the selected dispersion of the spectrometer, each recorded spectrum typically consists of intensities in energy ranges that can be attributed to the background signal, as well as ones corresponding to core loss edges, plasmon peaks, etc. Since most of the contamination is carbon-based, the carbon K edge, which starts at around 284 eV [106], can be a suitable region of interest (ROI). However, this approach only works for materials that do not contain carbon in the first place, such as h-BN. While there are methods to determine the sp^2 and sp^3 fractions in amorphous carbon using EELS, this method requires reference spectra, as well as the ability to resolve fine structures [115]. Another type of ubiquitous contamination is silicon [52], with a corresponding L$_{2,3}$ edge starting at 99 eV [106]. Its elastic scattering cross section is over twice as large as that of carbon [116], making it a viable option in detecting contamination using the EELS spectrum for graphene.

After choosing the ROI, the background is subtracted using a power law fit function on the area preceding the ROI. Then, all the intensities in the ROI are integrated, which provides the final intensity value of the corresponding pixel.
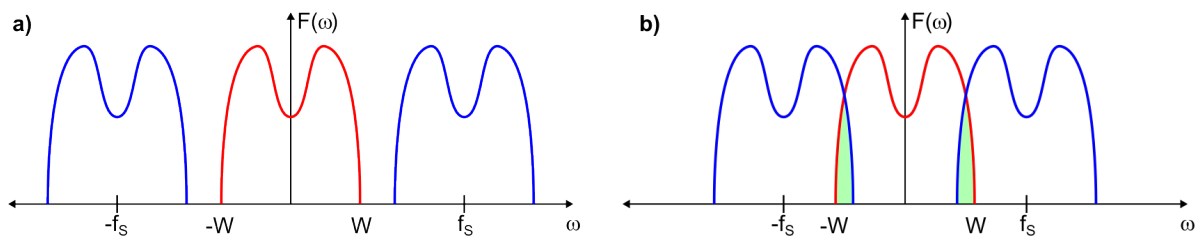
Figure 3.14: **Nyquist-Shannon sampling theorem and aliasing.** (a) A signal (red) with a maximum frequency of W is sampled at a rate f_S that is higher than $2W$. This results in no overlap of the red and blue spectra. (b) The signal is sampled more often than $2W$, causing an overlap (green), resulting in aliasing. Adapted from [118], licensed under a CC-BY License.

3.3.4   Nyquist–Shannon sampling theorem

In digital image processing, the rate at which an analog signal is sampled has to meet a certain criterion in order to be accurately reconstructed in the digital image[2]. The Nyquist-Shannon sampling theorem states that the sampling rate f_S must be at least twice as high as the largest spatial frequency (and hence the smallest distance in real space) one wants to resolve. In the case where one only wants to sample frequencies with a certain frequency range (band), the minimum sampling rate has to be twice the bandwidth W. This defines the Nyquist frequency [117]

$$f_S > 2W \ . \tag{3.13}$$

In Figure 3.14a, the signal (red) is sampled (blue) at a frequency that is higher than twice the largest frequency that is present in the signal, while in Figure 3.14b, the sampling rate f_S is smaller than $2W$. If the sampling rate is not chosen high enough, the sampled data will not be correctly represented, and the concept of aliasing occurs (green area). This can manifest as distortions or artifacts in the digital image, arising from an incorrect interpolation of the signal between the sampling points. When this happens, a signal above $\frac{f_S}{2}$ is mirrored back into the region between 0 and $\frac{f_S}{2}$, generating a signal in "fake" spatial frequencies that did not exist in the analog signal.

Sampling at a frequency that is larger than the Nyquist frequency is necessary if the original signal is to be reconstructed from the sampling points. Figure 3.15 illustrates this using a sinusoidal temporal signal that is sampled below (Figure 3.15a), at (Figure 3.15b), and

---

[2]This is technically not limited to only images but other signals such as audio as well.
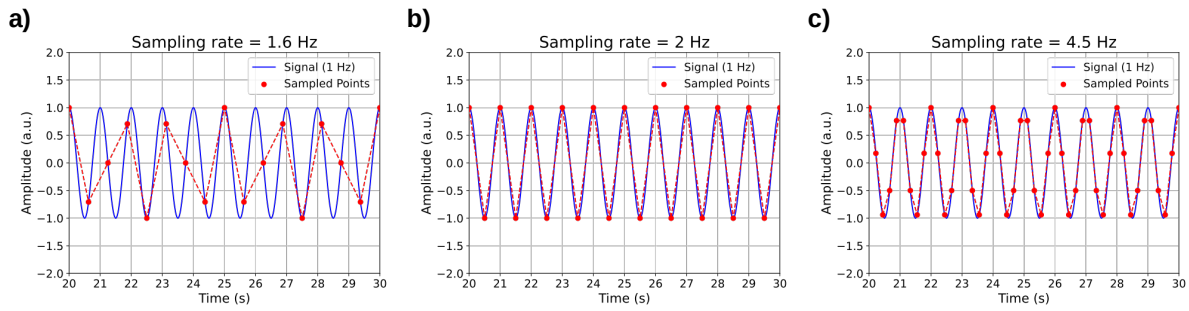
Figure 3.15: **Sampling of a signal at different sampling frequencies.** A temporal sinusoidal signal (blue, 1 Hz) is sampled (red dots) (a) below, (b) at and (c) above the Nyquist frequency.

above (Figure 3.15c) the Nyquist frequency. When sampling below the Nyquist frequency, the periodicity of the original signal cannot be replicated and thus, the original signal is not reconstructed, and a signal at a frequency that did not originally exist is introduced. When the sampling occurs at the Nyquist frequency, the frequency can be reconstructed, but the sinusoidal shape is lost. Sampling above the Nyquist frequency retains the periodicity of the signal and allows proper reconstruction.

An equivalent definition of the Nyquist-Shannon sampling theorem is that the pixel size p in a digital image must be less than half the size of the smallest distance d one wants to resolve

$$p < \frac{d}{2} \ . \tag{3.14}$$

Thus, in STEM, choosing a small enough pixel size is essential in order to avoid spatial aliasing artifacts. If resolving the crystal lattice is desired, then the sampling rate must be smaller than half the distance between two equivalent points in the lattice. To discern the positions of neighboring atoms, the pixel size must be smaller than half the distance between them.

Chapter 4

Results and Discussion

After assembly of the heating stage, but before inserting any samples, it was baked at over 400°C in UHV for 2 h to aid in removing residual contamination inside the chamber and evaporating any surface material from the tungsten filament. This temperature was reached with 18 A at 3.5 V and seems close to the highest stable output power achievable with the used setup. Since I do not intend to use this configuration again in this study, this process made sure that any surface material that could potentially evaporate from the filament at that temperature has already evaporated. This ensures that no material originating from the filament will deposit onto the samples during the cleaning process.

The used graphene samples are commercial samples from Graphenea titled *Monolayer graphene on TEM grids*. They are grown via CVD, and suspended on Quantifoil® TEM gold grids. All measurements were carried out using the Nion UltraSTEM 100 at the University of Vienna operated at 60 kV. Each sample was baked at 150°C for 10 h after introducing it into the CANVAS system to remove water and reduce the amount of hydrocarbon contaminants, after which it stayed in UHV for all measurements and annealing processes.

4.1 Pre-characterization of the contaminated samples

4.1.1 Mobile contamination

Due to the high abundance of surface contaminants on the used graphene samples, the amount of rapidly moving diffuse surface contamination made characterizing the samples difficult. This
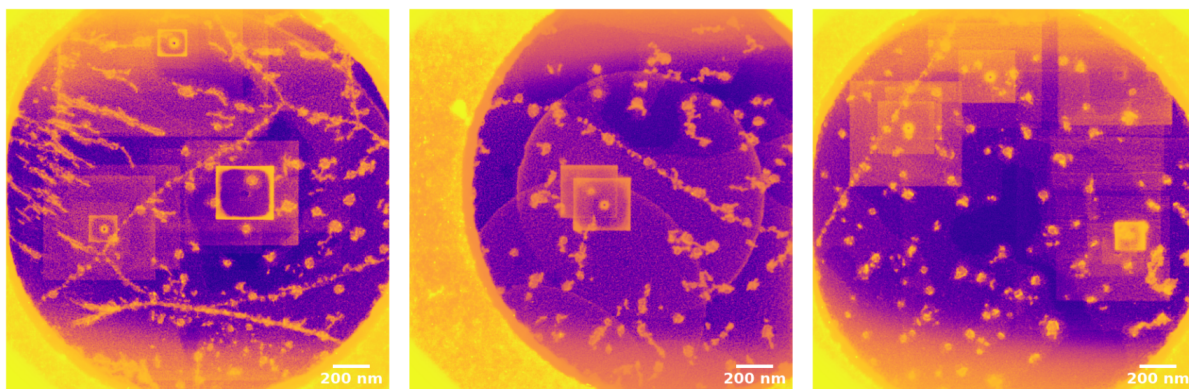
Figure 4.1: **Mobile contamination in STEM.** STEM-MAADF images of three different holes in the holey carbon support film (bright contrast on the edges and corners) containing freestanding monolayer graphene that are affected by mobile contamination upon extended electron beam exposure. The bright contrast indicates contaminated regions. The visible squares correspond to pinned-down contaminants in ADF mode, while the circles originate from imaging in CCD mode.

mobile contamination manifests and becomes visible inside and on the edges of the area that is exposed to the electron beam [119] and can be seen in Figure 4.1. The visible squares represent attracted contamination when imaging the sample in ADF mode due to the scanning of the electron beam over the given (square) area. The circles arise from imaging in CCD mode, where the electron beam is stationary and defocused.

Due to the increased local current density, this attraction and subsequent pinning down of contamination becomes stronger and appears more quickly at higher magnifications [119]. Figure 4.2a shows monolayer graphene surrounded by contamination. Here, it is not yet apparent that mobile contamination has been pinned down, which becomes clear upon lowering the magnification in Figure 4.2b and c. Further exposure to the same area increases the amount of electron beam-induced hydrocarbon deposition (Figure 4.2d), in particular towards the center and the edges of the scan. This is because the initial scan of the area starts to attract mobile contamination, which acts as attachment points for the diffuse contamination that is omnipresent on the material's surface. However, the amount of available diffuse contamination within the scanned area is much smaller than outside, when the supply of new contaminants is slower than their decomposition [120]. Subsequent scans will keep picking up this contamination, that can become immobilized once it reaches a contamination seed, or the edges of the scanned area. Eventually, the amount of mobile contamination inside the scanned area becomes exhausted, and further mobile contamination can only be attracted from the
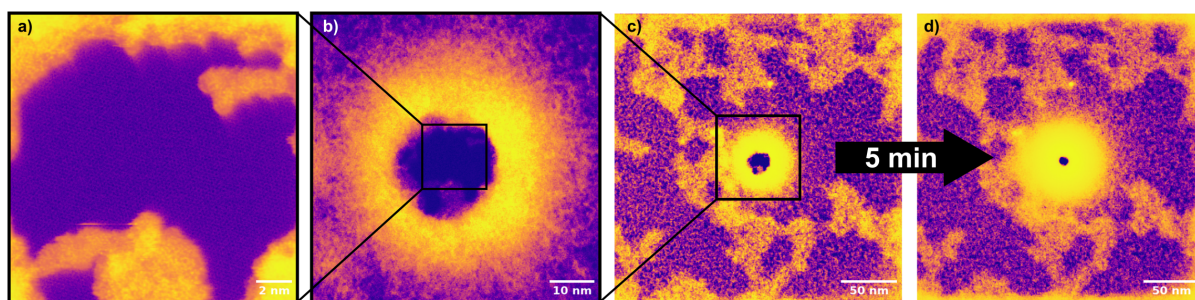
Figure 4.2: **Mobile contamination in STEM at higher magnifications.** (a) STEM-MAADF image of the graphene lattice surrounded by contamination. (b) Lower magnification of (a) shows the shape of the attracted mobile contamination. (c) Even lower magnification shows that mobile contamination is also attracted to the edges of the scan. (d) Evolution of the contamination after scanning the same area for 5 min.

outside. This causes a square-shaped wall to form that is roughly the size of the area that is scanned by the electron beam. The circular appearing contamination in the center of Figure 4.2d started as a square (from scanning at a higher magnification), where more and more mobile contamination is pinned down over time. The reason why there is more contamination towards the edges of the scanned areas could also be attributed to the fast scanning speed (2 µs dwell time) that was used to acquire the images. At slower scanning speeds, contamination can also uniformly deposit inside the scanned area [61] since the electron beam remains at each scan position for longer, giving new incoming molecules time to reach the area.

One way to combat mobile contamination is to perform "beam showers" [119]. This is the process of purposefully exposing a larger area around the region of interest to the electron beam for an extended time, typically in the order of minutes [121]. This reduces the amount of contamination growth inside the exposed area by reducing the density of mobile contamination in its vicinity [59]. The electron beam disrupts the stable state of the diffuse hydrocarbon molecules by decomposing them into smaller fragments. The subsequent cross-linking process picks up more and more fragments until they become immobile and start to grow a thin amorphous carbon-rich film on the sample surface. The goal is to pin down mobile contamination towards the edges of the exposed area, where this "wall" can then act as a shield for future mobile contamination, allowing imaging inside the beam-showered area for extended periods [119]. Figure 4.3 shows the effect of the performed beam shower. It was performed in CCD mode for 10 min. The brighter contrast in Figure 4.3b (labelled exposed area) displays the area that was exposed to the electron beam. Interestingly, the freestanding graphene in Figure
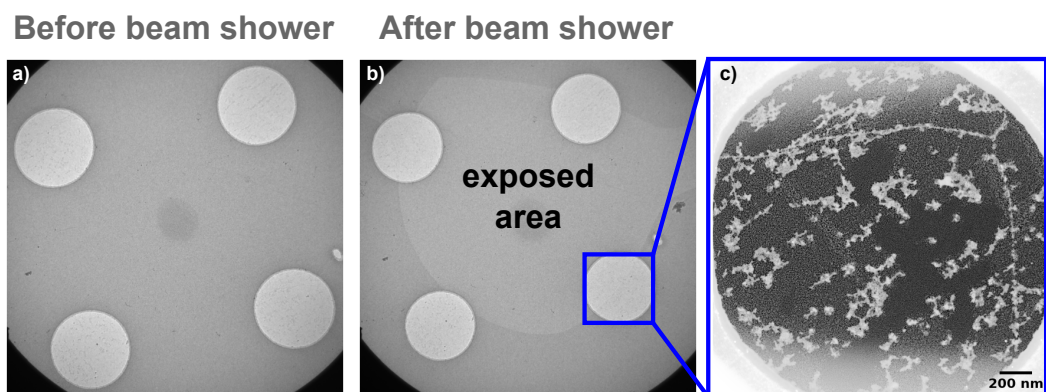
Figure 4.3: **The effect of beam showering.** (a) CCD image of four holes containing suspended monolayer graphene before beam showering. (b) The same area after beam showering for 10 minutes in CCD mode. The beam-showered area can be identified by the brighter contrast. (c) MAADF image of the boxed area in (b).

4.3c lacks any features resembling beam showering, which is apparent from the lack of visible edges of the exposed area. Still, after performing the beam shower, the four visible holes in Figure 4.3a and b remained devoid of mobile contamination for hours.

4.1.2   Local structure of contamination
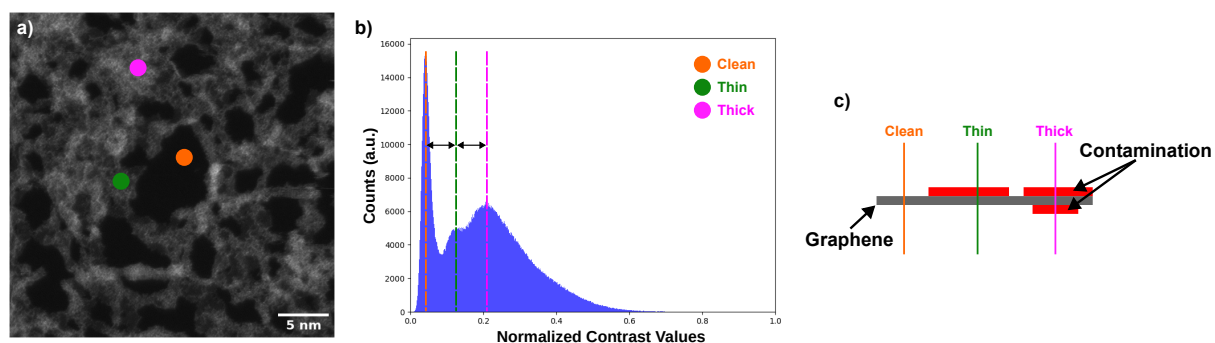
Figure 4.4: **Showcase of the presence of contamination on both sides of suspended monolayer graphene.** (a) MAADF image of monolayer graphene with visible contamination (brighter contrast). (b) Contrast intensity histogram of (a) after applying a Gaussian filter ($\sigma = 1$ px). The distances between the center of the peaks between the clean areas as well as the thick and thin contamination are denoted by black arrows. (c) Schematic sketch of contamination (red) on both sides of graphene (grey).

Since the samples that are used in this work are freestanding monolayer graphene, it follows that there are contaminants on both sides of the material. While the amount of residue

from the sample transfer is predominantly only on one side of the specimen [38], airborne contaminants can stick to both sides of the surface. It can be seen in Figure 4.4a that there is a different amount of contrast on the contaminated sites, represented by different shades of gray. The corresponding histogram in Figure 4.4b contains three major peaks, the first belongs to the clean sites, the second is from thinner contamination, and the third represents thicker contamination. The distance between the first and the third peak is roughly twice the distance between the first and second, which is highlighted by the black arrows and dashed vertical lines. Assuming that most of the contrast in the contaminated areas arises from mass-thickness-contrast, this implies that the average thickness of the thicker contamination is approximately twice that of the thinner contamination (see schematic in Figure 4.4c). Hence, it can be speculated that the thicker-appearing contamination originates from overlapping contamination on both sides of the sample. This could be further investigated by conducting plasmon-loss (or low-loss) EELS maps [122]. However, the uncertainty of the thickness estimation using this method is $\sim$20 %, and the delocalized nature of plasmons makes it difficult to obtain information on the local structure of contamination on the nm- and sub-nm-scale [99].

4.1.3 Types of contaminants

The elemental composition of the contamination was analyzed using atomically-resolved EELS. This allows parking the electron beam on a specific position on the sample, where the obtained signal in the EELS spectrum is only limited by the probe size and elastic scattering cross section of the atoms at the probe position.

Selected background-subtracted EELS spectra on clean (green) and contaminated (red) sites of the graphene samples can be found in Figure 4.5. Both carbon spectra were normalized to the 1s $\to \pi^*$ peak to allow better visualization of the fine structures. The presence of carbon signal on both clean and contaminated patches is because graphene itself is made of carbon atoms only. The difference in the lineshape between the two spectra in Figure 4.5a is due to the difference in how carbon is bonded in pristine graphene (sp^2) compared to amorphous carbon in the contamination [115]. There is also a strong silicon signal (Figure 4.5b) on contaminated sites, as silicon is universally present in carbon contamination [52], while it is absent in clean areas.
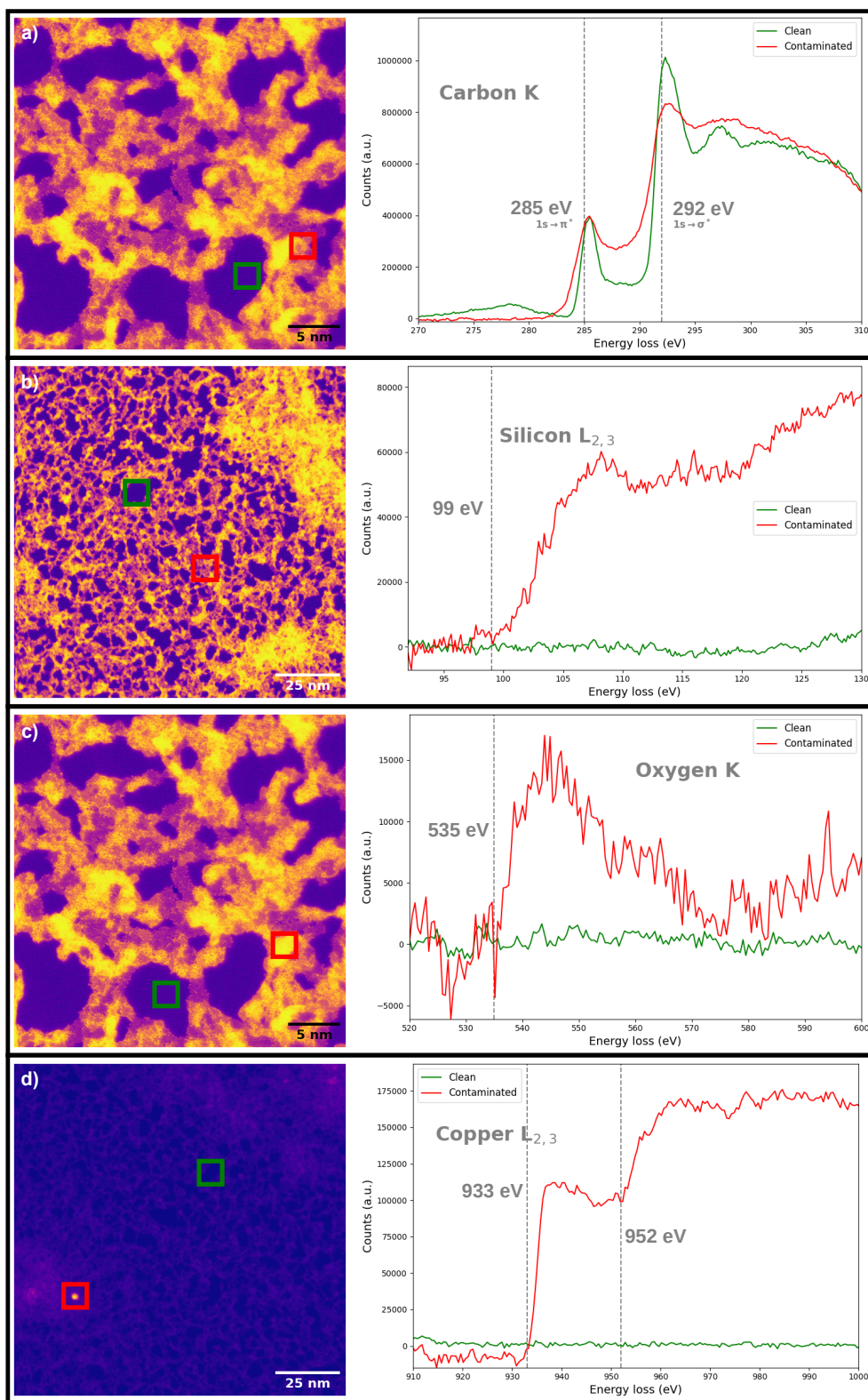
Figure 4.5: **Positioned EELS spectra on graphene for selected edges attributed to contamination.** The first column shows filtered MAADF images, where the EELS spectra were taken within the highlighted squares. The second column shows the corresponding EELS spectra for the carbon K, silicon $L_{2,3}$, oxygen K, and copper $L_{2,3}$ edges on clean (green) and contaminated (red) sites.

A weak oxygen signal was also found on contaminated sites (Figure 4.5c), which is likely due to the oxygen inside the hydrocarbon contamination [123]. While it is possible that this oxygen signal could be from water, all samples were baked at 150°C before imaging, at which it should have evaporated. Furthermore, copper clusters were identified (Figure 4.5d) and are assumed to originate from the CVD growth substrate. The Cu atoms condense into nanosized clusters and, unlike Si and O, are not dispersed within the amorphous carbon contamination that makes up the majority of the contaminated areas.

4.1.4 EELS map analysis
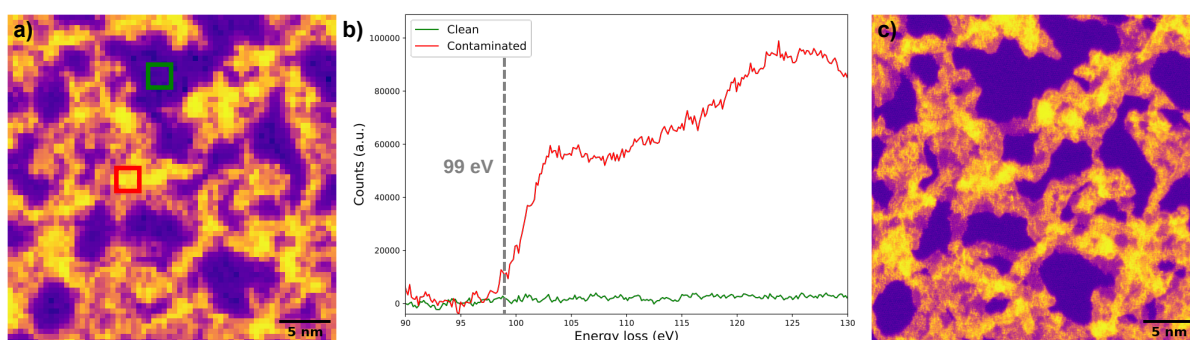
Figure 4.6: **Comparison of Si $L_{2,3}$ edge EELS map and corresponding MAADF image on graphene.** (a) Si $L_{2,3}$ edge EELS map with corresponding spectra in (b) acquired on contaminated (red) and clean sites (green). (c) MAADF image of the same area for comparison.

In order to obtain EELS maps for graphene that allow to distinguish between contaminated and clean areas on the sample surface, the Si $L_{2,3}$ edge is chosen for the EELS signal. The high elastic scattering cross section of Si ($0.16\ a_0^2$ over all scattering angles at electron energies of 60 kV, where a_0 is the Bohr radius [116]) as well as its universal presence in carbonaceous contamination [52] manifests in a strong signal in contaminated areas. Figure 4.6a shows the resulting EELS map. The FOV of the scan is 32x32 nm^2 with a 64x64 px array, resulting in pixel sizes of 0.5x0.5 nm^2 and 4096 total spectra. Each spectrum was acquired for 200 ms at the center of each pixel. Background subtraction was carried out over an energy range of 75 - 95 eV using a power law fit function, after which the intensities were integrated from 98 - 115 eV. Figure 4.6b shows Si $L_{2,3}$ spectra on a clean (green square) and contaminated site (red square) on the specimen. Clearly, there is a strong silicon signal in the contaminated area, which is absent on clean patches. For comparison, Figure 4.6c shows a MAADF image (2048x2048 px, 10 µs dwell time) of the same area. The better contrast in the MAADF image provides more
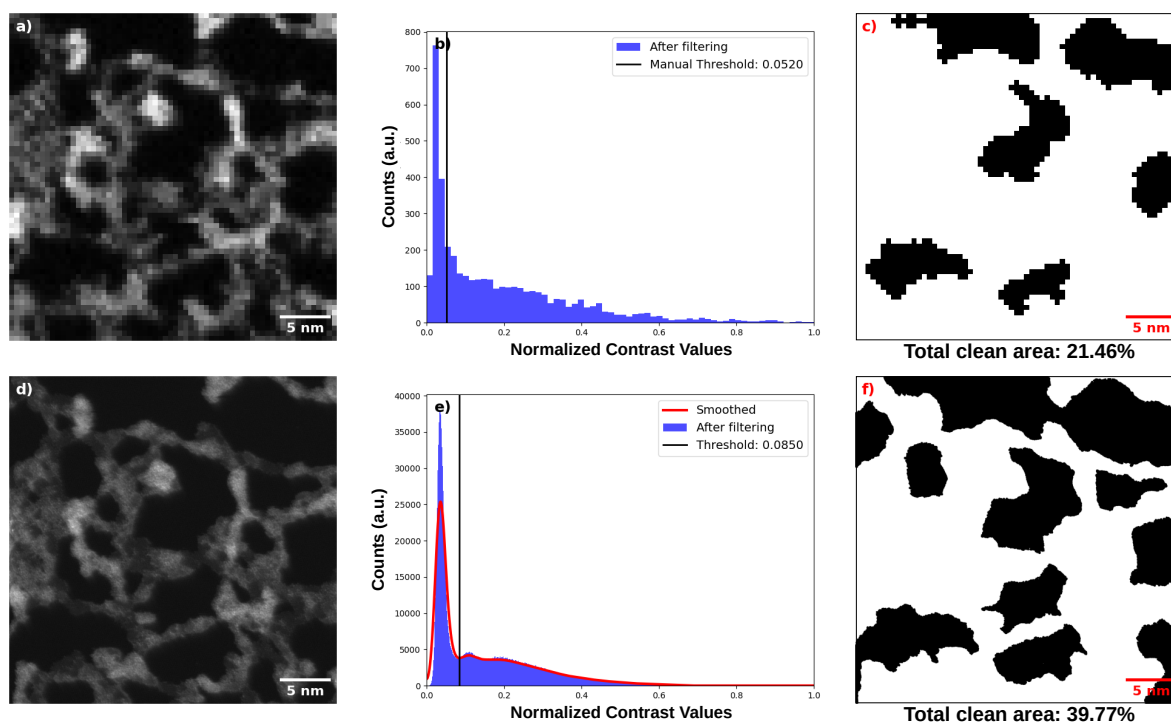
Figure 4.7: **Comparison of the thresholding process for EELS maps and MAADF images on graphene.** (a) Si $L_{2,3}$ edge EELS map with its corresponding histogram in (b). The manually thresholded binary image from the EELS map is shown in (c). For comparison, a MAADF image of the same area was taken and is shown in (d). The threshold in the histogram in (e) was calculated using the minimum method, resulting in the binary image in (f).

information on the local structure of the contamination and the increased number of pixels makes the edges of the clean structures more well-defined.

A comparison between the Si EELS map and the corresponding MAADF image for quantitative analysis of the total clean area for graphene was carried out and is shown in Figure 4.7. Due to the smaller FOV in both images and the lower number of pixels in the EELS map, all the values for the digital image processing steps as described in section 3.3.2 are adjusted accordingly. While it can be seen that the information regarding the contamination obtained from the EELS map mostly correlates with the MAADF image, some issues are present.

Firstly, for practical reasons, each of the 4096 spectra in one map has to be background-subtracted automatically. This requires the background subtraction to be consistent across all spectra and can be accomplished by increasing the signal-to-noise ratio (SNR), which can be achieved by increasing the dwell time of each spectrum. However, this necessitates reducing the total number of pixels in the image not only to attain reasonable total acquisition times

and minimize the effect of the sample and/or stage drift, but also to avoid exposing the same area to the electron beam for too long. This is because extended electron beam exposure results in chemical etching of the edges of the contamination, likely due to the presence of oxygen radicals in the contamination [123]. The etching process is displayed in Figure 4.8, where exposing the same area for 25 min resulted in an observable change of the shape of the contaminated areas, effectively "cleaning" the scanned area. In addition, a noticeable drift outlined by the colored boxes and arrows was observed. Since the etching effect directly influences the resulting total clean area in the obtained image, using EELS maps for measuring the total clean area of the used samples is not a viable method. While there is also an etching effect when acquiring MAADF images, the total exposure time is much lower, which is in the order of seconds compared to minutes for EELS maps. This effect can be minimized by quickly obtaining a MAADF image and then moving to the next area.

Secondly, the obtained total clean areas between the two methods do not match (21.46% for the EELS map, 39.77% for the MAADF image). Part of this can also be attributed to the etching process and drift, which makes a direct comparison between the two images difficult. Also, the measured contrast in the EELS map makes thresholding the image not straightforward. The threshold was manually chosen (see Figure 4.7b), which took some trial and error as the correct bin for the threshold is not immediately apparent from the histogram. Changing the number of bins did not seem to help the algorithm determine a useful threshold, and using a different thresholding method (triangle method) provided better but still unsatisfactory results. This makes thresholding and segmenting the EELS map images time-consuming and introduces observer bias, while simultaneously having worse resolution than MAADF images. It is possible to get a better match between the EELS map and MAADF image, however, this would require careful consideration of the threshold and would also introduce considerable observer bias.

However, EELS directly measures the elemental composition of the specimen, while ADF images only show the difference in scattering intensity at each probe position. While there is a correlation between scattering intensity and elemental composition in ADF images [105], EELS spectra (and consequently EELS maps), provide a more direct and physically meaningful measure for the presence of contamination when compared to ADF images.

In summary, while EELS maps can be an alternative to MAADF images, even though they have lower resolution, the cleaning effect induced by the electron beam when scanning the
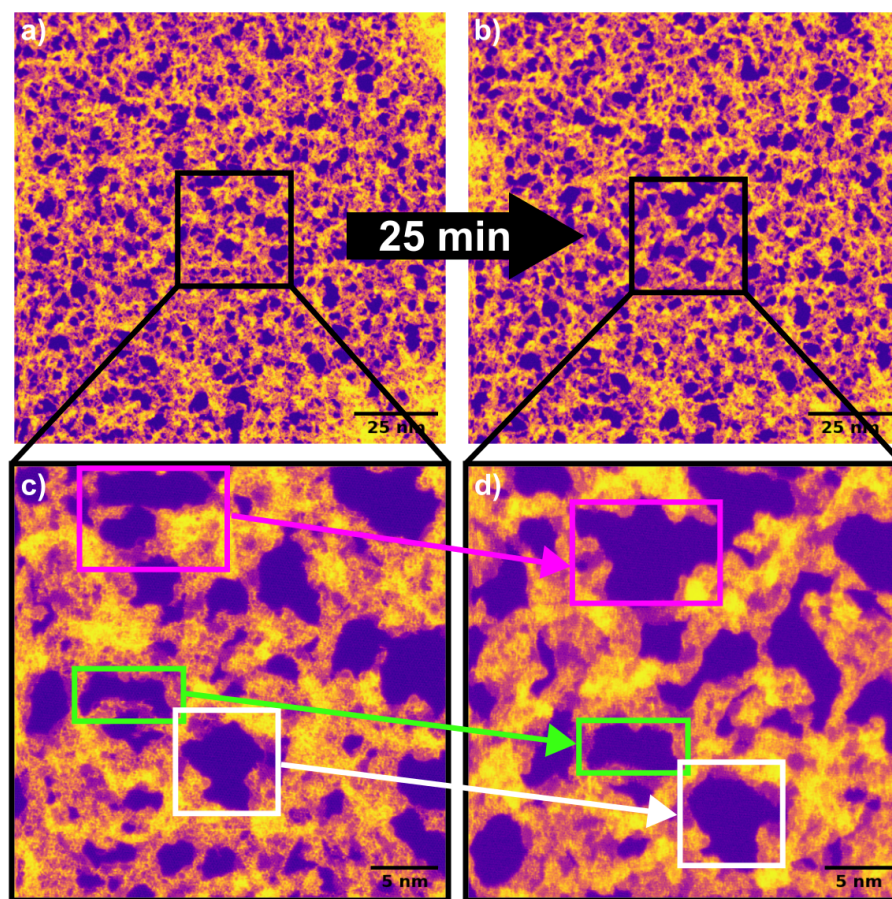
Figure 4.8: **Effect of extended electron beam exposure on the scanned area.** (a) MAADF image of heavily contaminted graphene (128x128 nm^2 FOV) with minimal prior exposure to the electron beam. (b) The same area after exposing a smaller area (black square) to the electron beam for 25 min. Higher magnification images in (c) and (d) show the area inside the black squares of (a) and (b) respectively. The colored boxes and arrows showcase the evolution of the clean patches over 25 min.

same area for too long has a direct effect on the measured result. Hence, EELS maps are not used in this work for quantifying the total clean area of the samples, and MAADF images are used instead. However, EELS can function as complementary data as it provides information on the local elemental composition of the contamination.

4.2 Cleaning results

4.2.1 Before thermal treatment
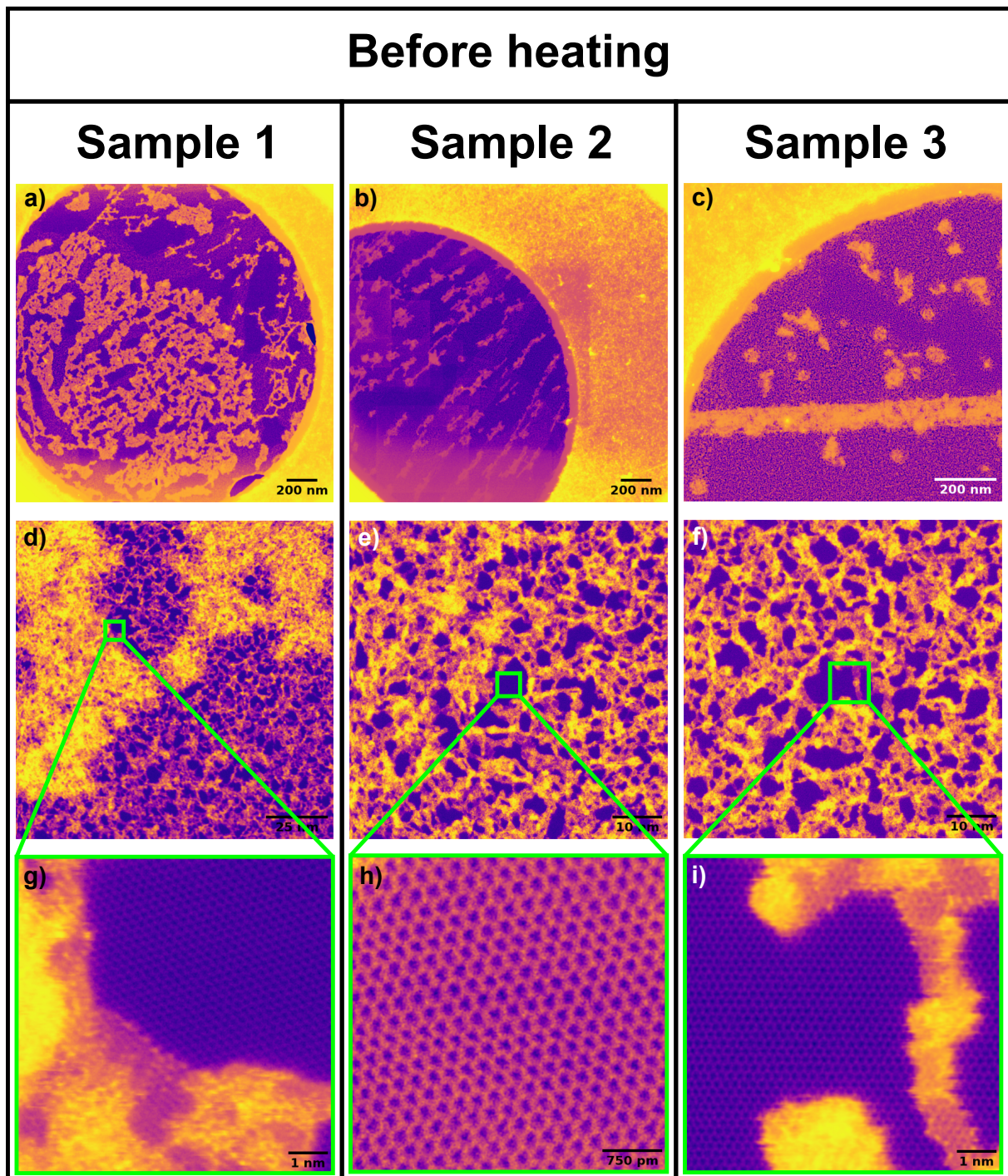
Figure 4.9: **Graphene samples before thermal annealing.** Filtered MAADF images of selected holes in three graphene samples. (a-c) show entire holes in the holey carbon support film. (d-f) shows selected contaminated areas including clean patches, which are shown at higher magnification in (g-i).

All samples were characterized before the annealing process. MAADF images of free-standing graphene on selected holes in the holey carbon support film were taken and can be found in Figures 4.9a-c. Here, the darker contrast does not indicate clean areas but thinner contamination, with the omnipresent contamination of different thicknesses covering the underlying free-standing graphene. Figure 4.9a contains a high amount of thick contamination (bright areas), which is lower in Figures 4.9b and c. The horizontal line in 4.9c is where the graphene folds, which manifests as higher contrast due to the higher thickness of the multilayer structure.

All three samples were very similar concerning the mesoscopic structure of the contamination, even if individual holes looked different. This is unsurprising, as they all came from the same batch from the manufacturer. Higher magnification MAADF images of the three used samples before the thermal treatment are shown in Figures 4.9d-f. They provide better insight into the local structure of the contamination, which is not apparent on lower magnifications. Figures 4.9g-i contain atomic-resolution MAADF images, clearly showing the graphene lattice obstructed and surrounded by contamination.

To assess the amount of contamination on each sample (both before and after the annealing process), around 30 images of each sample are taken at an FOV of 128 nm (or 256 nm) with a resolution of 2048x2048 px. This combination was chosen to avoid aliasing [117] while being able to capture a high number of clean patches in each image. The images were obtained from many different holes in the holey carbon support film distributed across a large part of the sample, and were thresholded and segmented as described in section 3.3.1. Out of the 174 total images analyzed in this work, 163 were automatically thresholded using the minimum method, while 11 were manually thresholded.

All three untreated samples were found to possess a similar amount of contamination, both in terms of total area, as well as the sizes of the individual clean patches. The amount of clean area was found to be only (2.8 ± 0.4) % for sample 1, (3.3 ± 0.6) % for sample 2, and (3.8 ± 0.7) % for sample 3 (medians of 2.2 %, 2.4 %, and 2.6 % respectively). The sizes of clean areas were also determined, showing an average of (23.2 ± 0.4) nm^2, (24.8 ± 0.5) nm^2, and (24.8 ± 0.5) nm^2, with respective medians of 20.8 nm^2, 20.9 nm^2, and 21.2 nm^2 with the largest clean patch across all three samples before annealing being 160 nm^2 large. The findings for all samples before and after the heating processes are summarized in Table 4.1 and visualized in Figure 4.10.
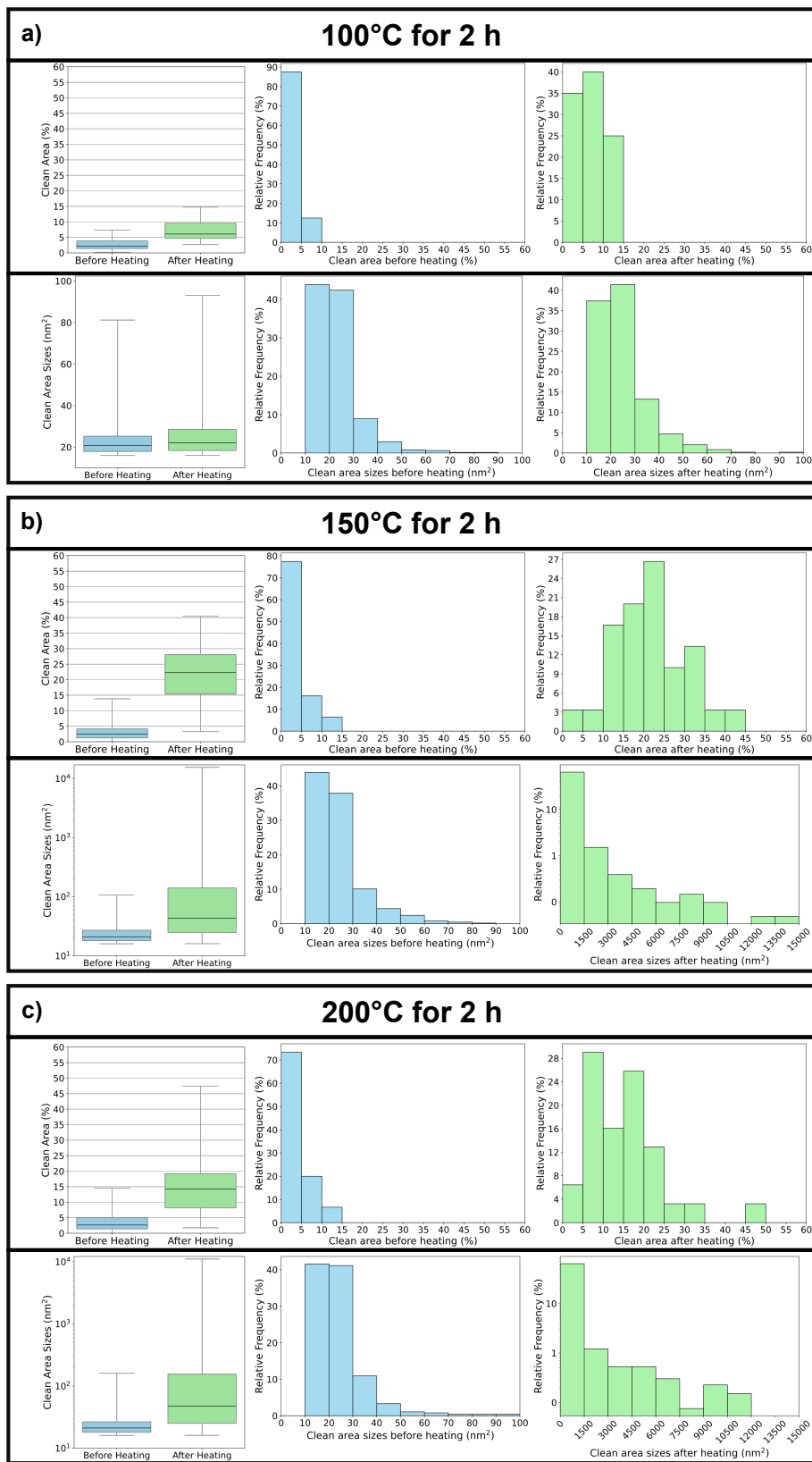
Figure 4.10: **Comparison of the total clean area before and after thermal annealing.** Boxplots and histograms comparing the clean area in % of the total area in the taken MAADF images, as well as their size distribution before and after annealing at (a) 100°C, (b) 150°C, (c) and 200°C.
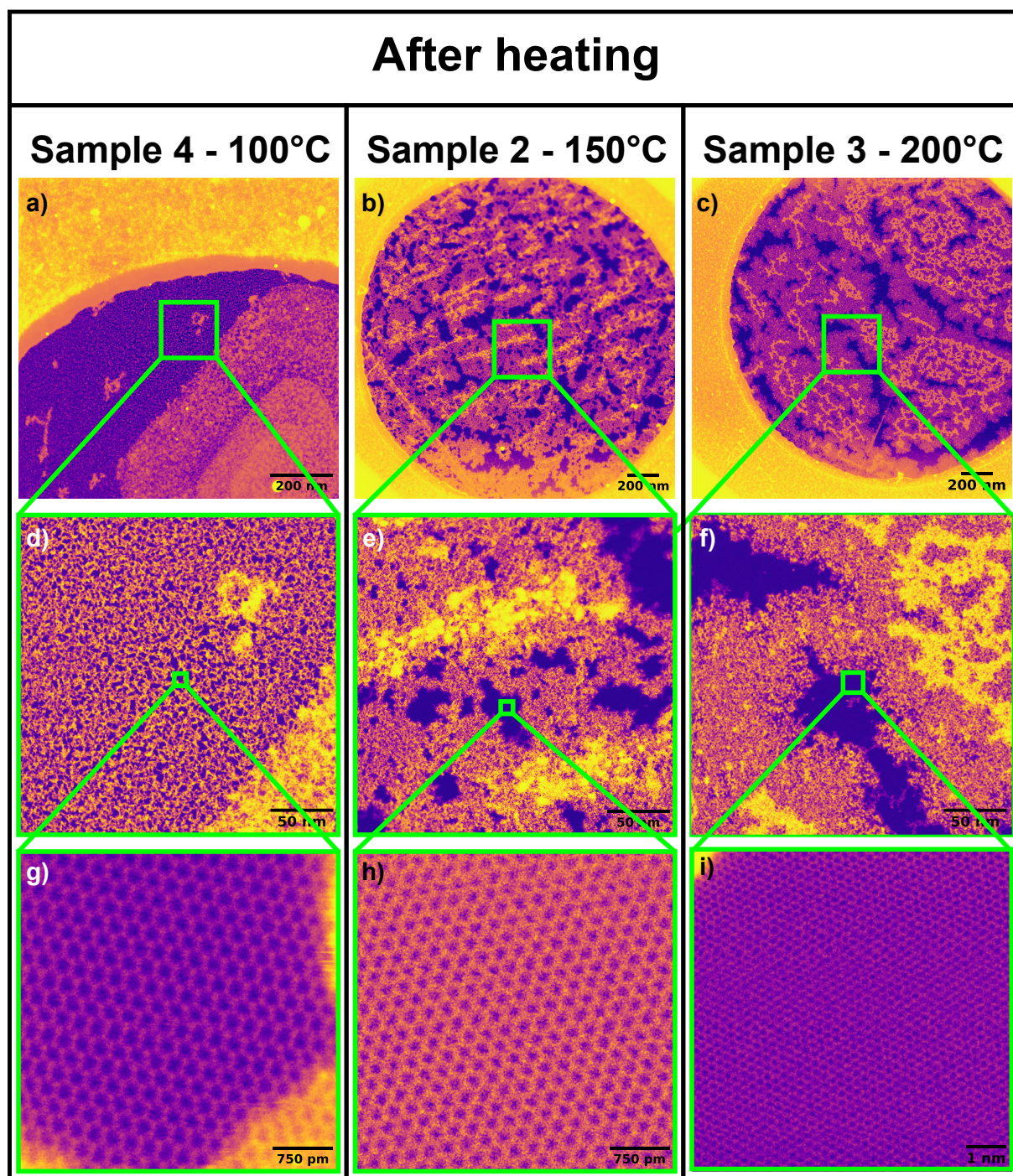
4.2.2 After thermal treatment

Figure 4.11: **Graphene samples after thermal annealing.** Filtered MAADF images of selected holes in all three graphene samples after heating to different temperatures. (a-c) show large parts of a hole in the holey carbon support film, providing mesoscopic insight into the contamination after the treatment. (d-f) shows selected contaminated areas with visible clean patches, which are shown at even higher magnification in (g-i).

Wire Power	Temperature	Rel. area before (%)		Rel. area after (%)		Sizes before (nm^2)		Sizes after (nm^2)	
		mean	median	mean	median	mean	median	mean	median
9 W	100°C	2.8 (0.4)	2.2	7.3 (0.8)	6.1	23.2 (0.4)	20.8	25.2 (0.4)	22.0
17 W	150°C	3.3 (0.6)	2.4	21.6 (1.6)	22.3	24.8 (0.5)	20.9	284.7 (27.2)	43.4
25 W	200°C	3.8 (0.7)	2.6	15.4 (1.7)	14.2	24.8 (0.5)	21.2	340.5 (38.1)	47.4

Table 4.1: **Summary of cleaning results.** The relative clean areas (mean and median) in % of the total area (standard deviation in parentheses) for each sample are compared before and after annealing at the given temperatures that were sustained at a given wire power. The average (standard deviation in parentheses) and median sizes of the clean patches are also summarized.

The sample used to determine the cleanliness after heating to 100°C was not the same as before the treatment. However, it was briefly characterized before the annealing process and deemed to be similar to the others, both in terms of total contamination, contamination structure, and mobile contamination. It came from the same batch and from the same manufacturer as the one that was characterized before the heating treatment. The similarities between all untreated samples are further supported by the similar amount of contamination present on the three untreated samples (see Table 4.1).

100°C for 2 h

The first sample was heated to a modest temperature of 100°C for 2 hours. This temperature is lower than what all samples were already baked at in the loadlock after insertion into the CANVAS system. Hence, no cleaning effect should be observed after the treatment. While the samples may be getting re-contaminated while remaining in UHV, this typically only happens over extensive periods of time, while all samples in this study were inserted into the system and studied within one month. Furthermore, heating to a low temperature could allow us to gauge the temperature reported by the thermocouple during the annealing process. While it is positioned as close to the sample (and in contact with the puck) as feasibly possible, it may report a lower temperature than what the sample experiences.

Comparing Figure 4.9d to Figure 4.11d, the sample looked about the same as before the treatment. Only very small clean areas could be found akin to all three untreated samples. This indicates that 100°C is likely below or slightly above 150°C, although statements about an upper limit cannot be made from this measurement alone. Still, the cleaning effect at this temperature and treatment duration was minimal, indicating that it is probably well below

300°C, which is often reported to start producing cleaning results on graphene via thermal annealing in vacuum [18, 36]. Also, no significant change in the elemental composition of the contamination was observed (Figure 4.12), which is expected given the similarities in the contamination structure between the untreated and heated samples. The SNR in the O edge is only about 5:1, albeit the peak is still clearly visible. The weak signal might be due to extended e-beam exposure before acquiring the spectrum, which could have reduced the amount of oxygen in the exposed area [123].

While the size distribution, mean ((25.2 ± 0.4) nm^2), and median (22.0 nm^2) were largely unaffected by the annealing procedure, the total clean area has more than doubled from (2.8 ± 0.4) % to (7.3 ± 0.8) %. This can be attributed to the interaction of the electron beam with the contamination. When taking images, initially, the surface seems to be heavily contaminated, with only very few clean exposed graphene patches. However, the contamination appears to contract or move away from the illuminated area almost immediately upon e-beam exposure, which was also found but not explained by Dyck et al. [121] after annealing in Ar/O$_2$ at 500°C. It is unlikely that this change in the shape of the contamination originates from etching [123] that was observed before annealing since the change occurred almost immediately here. This observation will be further discussed in section 4.2.3.

After exposing the area to the e-beam for 30 min (Figure 4.12a), the shape of the contamination slightly changed, which is related to oxygen etching. One peculiar observation was that there was next to no e-beam-induced hydrocarbon deposition during imaging. This is in stark contrast to what was observed before the treatment, where beam showers were necessary to combat the heavy mobile contamination. In any case, the cleaning effect at this temperature was minimal, and higher temperatures are needed.

150°C for 2 h

The second sample was baked at 150°C for 2 h to verify that the temperature reported by the thermocouple is accurate. As mentioned already, all samples had already been baked at 150°C for 10 h in the loadlock. Hence, it is expected that another bake at the same temperature has very little if any effect on the amount of contamination. However, it was found that the sample had changed drastically, increasing the average sizes of the clean patches across all imaged holes on the sample. This indicates that the actual temperature is likely higher than what is reported by the thermocouple.
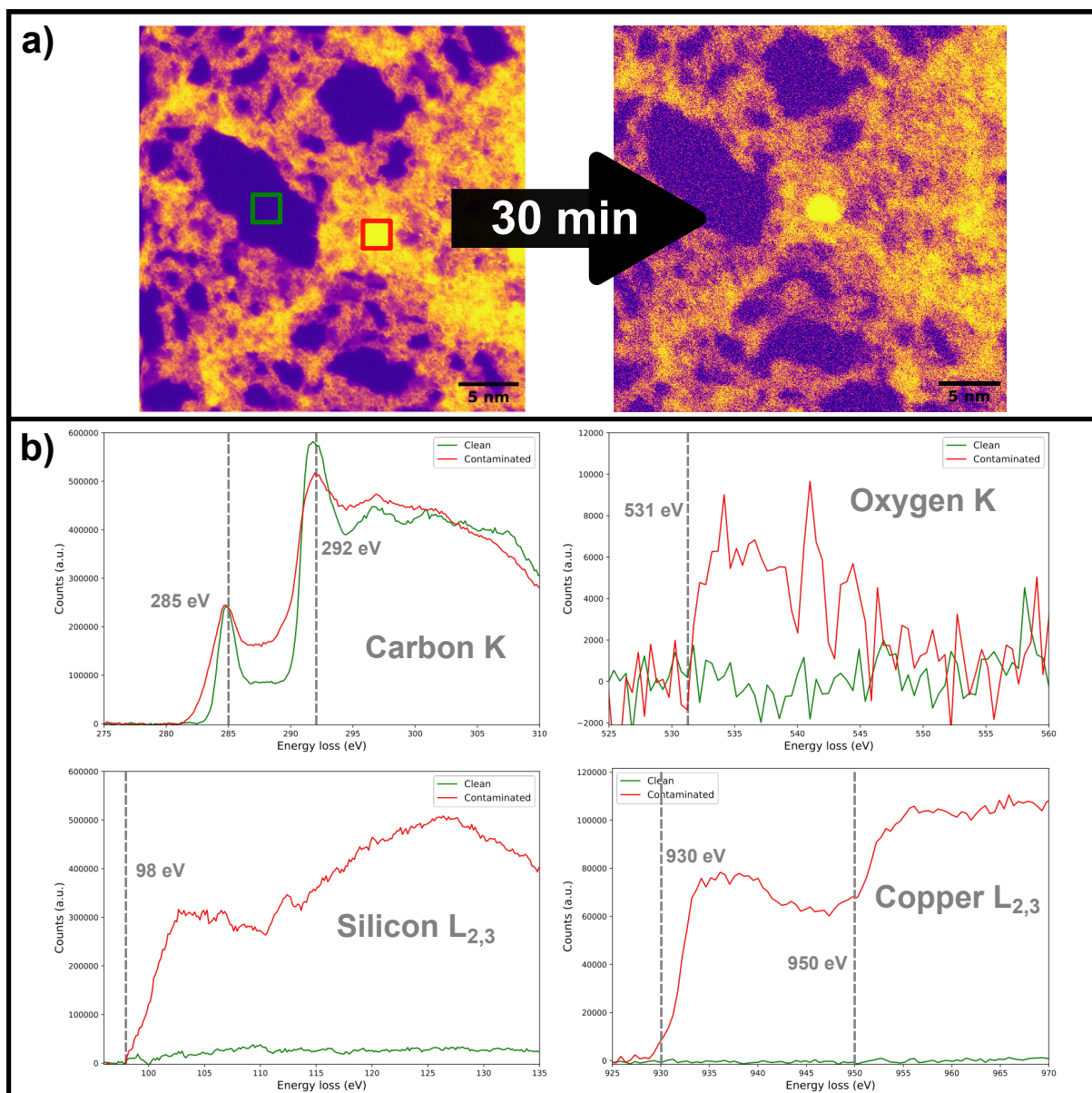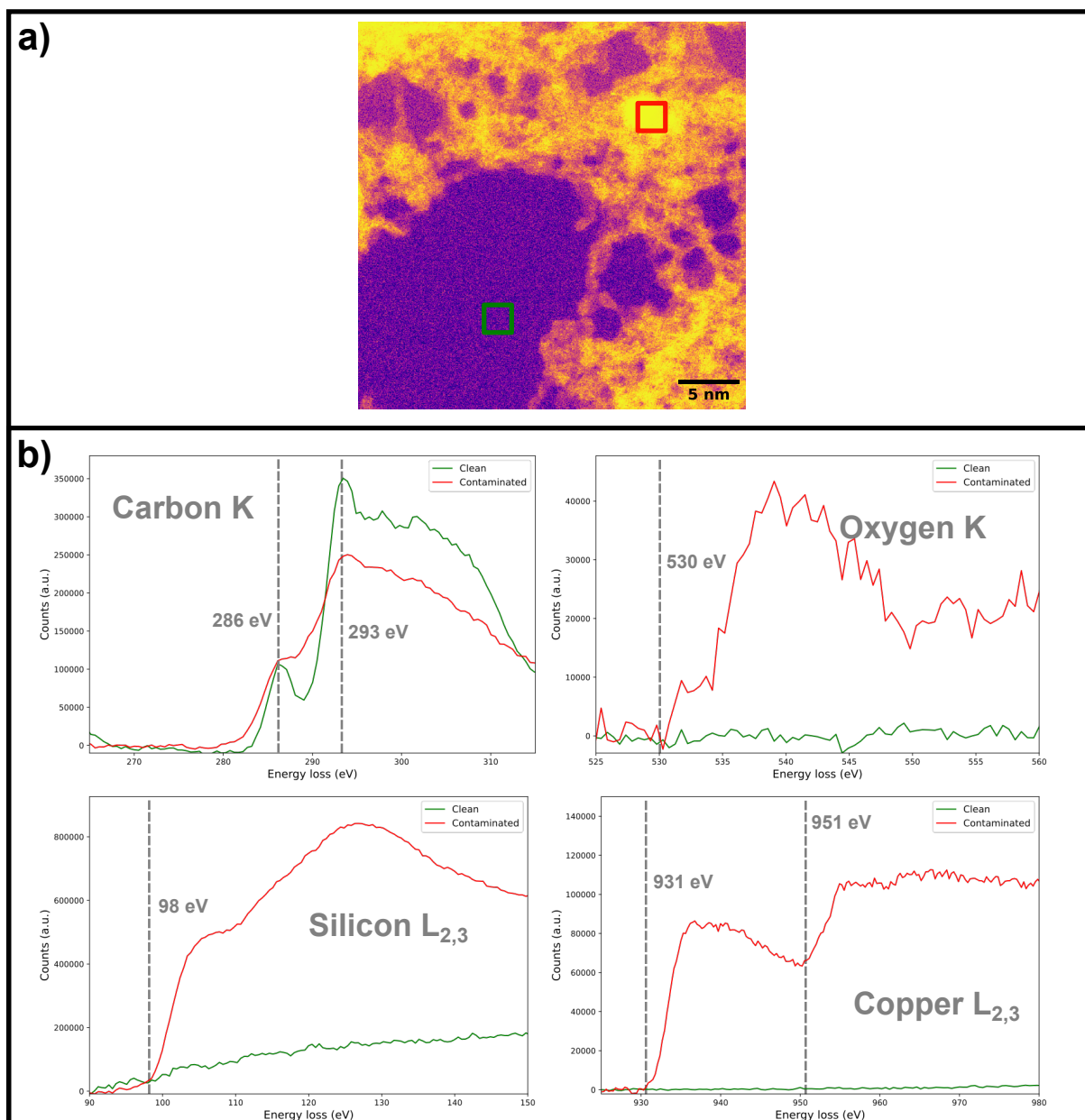
Figure 4.12: **EELS spectra attributed to contamination after heating to 100°C for 2 h.** (a) MAADF image (left) of the area from which the EELS spectra were taken. The boxed areas correspond to clean (green) and contaminated (red) sites. The picture on the right shows a HAADF image of the same area, taken after all EELS measurements have been taken. (b) Background-subtracted EELS spectra of carbon, silicon, oxygen, and copper core loss edges obtained from contaminated and clean areas.

The amount of total clean area as well as sizes of found clean patches before and after the heating are compared in Figure 4.10b. It has been found that this thermal treatment drastically increases the total clean area to an average of (21.6 ± 1.6) % (median = 22.3 %). As outlined in section 3.3.2, areas smaller than 16 nm^2 were excluded due to their small size. However, when counting all clean patches (on the untreated sample) that were identified
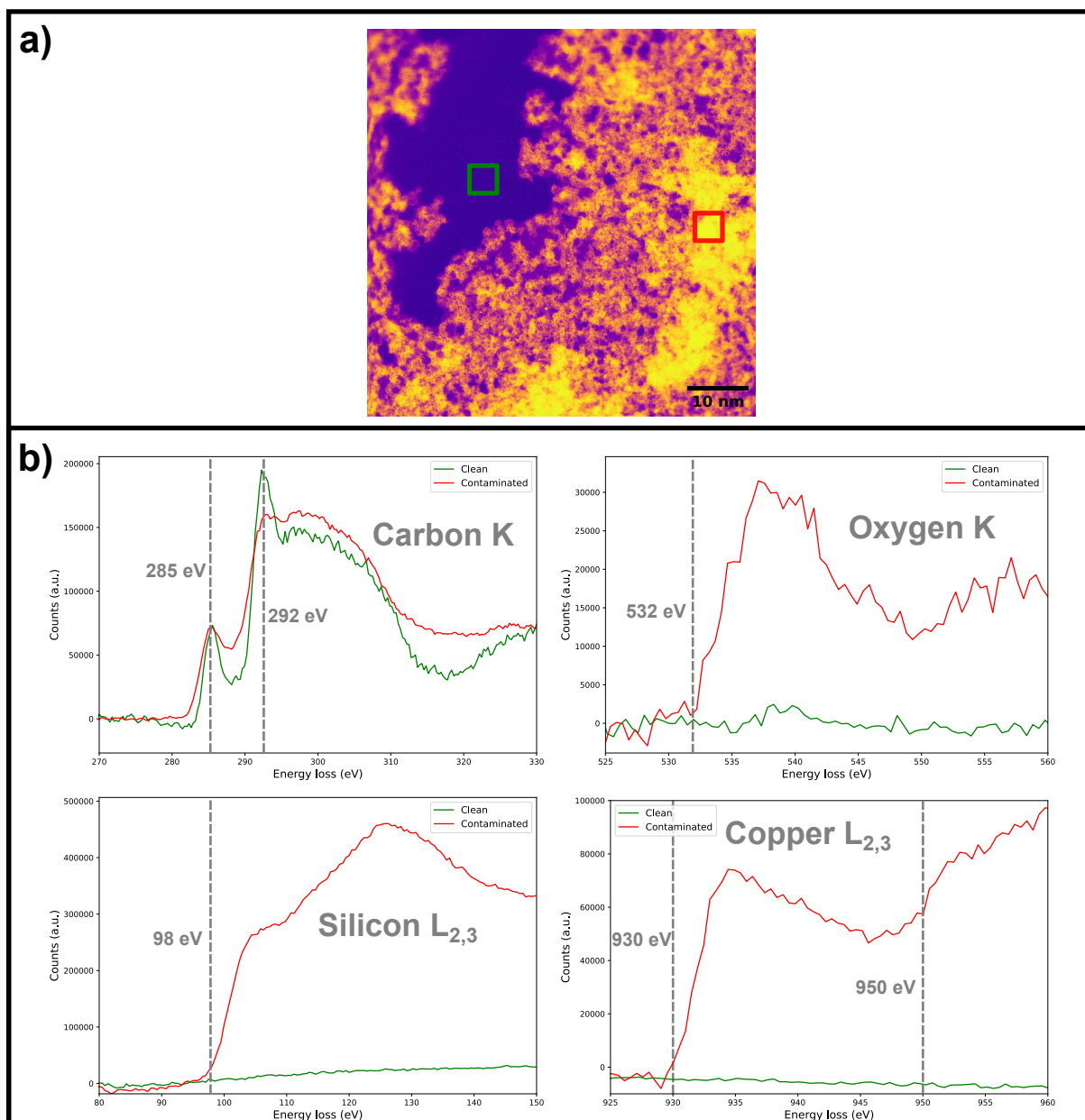
Figure 4.13: **EELS spectra attributed to contamination after annealing at 150°C for 2 h.** (a) MAADF image of the area from which the EELS spectra were taken. The boxed areas correspond to clean (green) and contaminated (red) sites. (b) Background-subtracted EELS spectra of carbon, silicon, oxygen, and copper core loss edges obtained from contaminated and clean areas.

via the thresholding and segmentation process (regardless of their size), the average amount of clean area changes to (20.4 ± 1.7) % with a median of 21.1 %. This is much closer to what was found after the heating process (within one standard deviation), where only very few small areas had to be excluded due to their small size. The total contrast in similar-looking images before and after the heating is comparable (at the same imaging conditions), indicating similar thickness of the contaminated areas. This suggests the contamination was
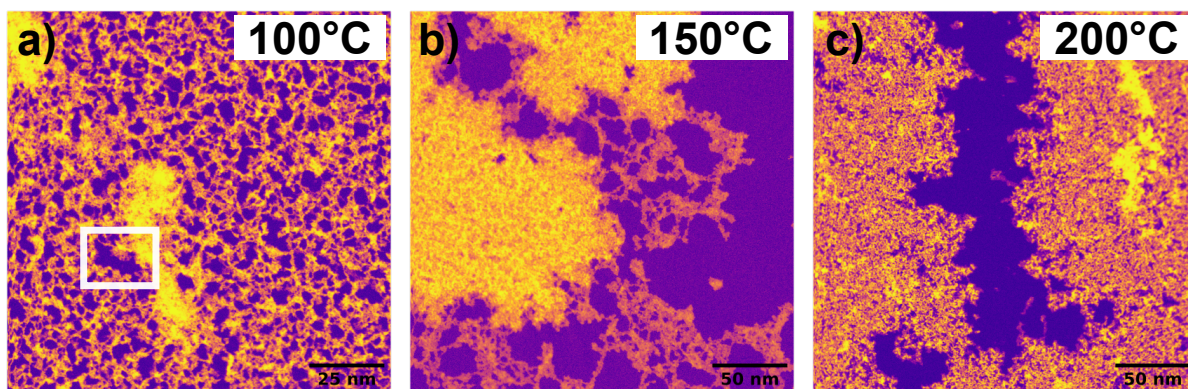
Figure 4.14: **MAADF images showing large clean areas on the annealed samples.** Showcase of larger clean areas (darkest contrast) that were found in this study after thermal annealing at (a) 100°C, (b) 150°C, and (C) 200°C. The white box in (a) marks the largest clean area found after the 100°C treatment.

mostly moved around via diffusion instead of desorbing at this temperature and treatment time. Since the diffusion coefficient D increases linearly with temperature [124], this could be an explanation for the observed cleaning result. Also, this implies that the actual temperature the sample was subjected to during this treatment is still below the desorption temperature for the majority of the contaminants present on the sample surface [32].

Looking at the EELS measurements in Figure 4.13b, the signals from all the elements observed before the heating process are still present. Both silicon and oxygen are still found within the carbon contamination. Copper clusters could also be identified. No other core loss signal in the energy range up to 1,000 eV was found, indicating that no foreign material (with core loss edges below 1,000 eV) has been introduced to the sample during the thermal annealing process.

Still, the drastically increased average size of 285 nm^2 is one order of magnitude larger than before annealing. More interesting, and also relevant, is probably the largest clean area that was found, which was over 15,000 nm^2 large and is shown in Figure 4.14b. It can be seen that this clean patch extends even further to the right of the image, effectively resulting in an even larger size.

Figure 4.15: **EELS spectra of clean and contaminated areas after annealing at 200°C for 2 h.** (a) MAADF image of the area from which the EELS spectra were taken. The boxed areas correspond to clean (green) and contaminated (red) sites. (b) Background-subtracted EELS spectra of carbon, silicon, oxygen, and copper core loss edges taken from clean and contaminated sites in (a).

200°C for 2 h

At first glance, heating sample 3 to 200°C for 2 h did not seem to induce drastic changes to the amount and shape of the contamination compared to sample 2, which was treated at 150°C. However, Figure 4.11c shows that the sizes of the clean areas seem to be larger, despite the surface being still heavily contaminated.

When comparing the results to the 150°C treatment (Figure 4.10b), the total clean area seems to be lower ((15.4 ± 1.7) % vs. (21.6 ± 1.6) %) when annealed at 200°C, with the average sizes of the clean areas favoring the 200°C treatment ((340.5 ± 38.1) nm^2). This can be explained by the way the data was collected. Firstly, some of the clean areas extended beyond the FOV of the taken images, which means that the areas of the large clean patches are probably larger than what was found here. Also, the clean patches on sample 2 (150°C) were more dispersed and evenly distributed, while they seemed more concentrated on sample 3 (200°C). Secondly, no special care was taken to find particularly large clean areas, which would have been a source of observer and selection bias for the statistics obtained in this study. More images would need to be taken to obtain better statistical results to provide conclusive evidence that annealing at 200°C produces a higher amount of larger clean patches when compared to lower temperatures. One way to accomplish this would be to acquire scan maps over even larger areas, which would provide a better insight into the true total clean area. However, this requires a very stable sample stage and flat support grid or an automatic algorithm that compensates for the change in defocus on an uneven support surface. Silicon nitride grids are a good candidate due to their increased rigidity [125], however, the total amount of suspended sample area is much smaller when compared to conventional gold TEM grids.

The strong discrepancy between the respective mean and median sizes for both the 150°C and 200°C treatments (see Table 4.1) indicates that a few large areas are skewing the mean towards higher values. These relatively big areas were also found during imaging (see Figures 4.11b and 4.11c) and are visible in the size distributions in Figure 4.10b and 4.10c. Despite the largest clean area being found on the sample that was heated to 150°C, it was very easy to find large clean patches after heating to 200°C, some even extending beyond the 256 nm FOV at which the images were taken. These large clean areas could be advantageous for sample manipulation, such as impurity atom implantation [114] or defect engineering [126], which benefit from large exposed areas to increase the likelihood of hitting the material instead of contamination.

Interestingly, the general shapes of the clean areas are elongated stripes for the majority of large clean patches, which could be explained by the effect of thermal expansion and contraction. Graphene possesses a negative thermal expansion coefficient [90], meaning that it expands when lowering the temperature, which could unveil clean patches due to the stretching motion when the sample is cooling down after the annealing treatment.
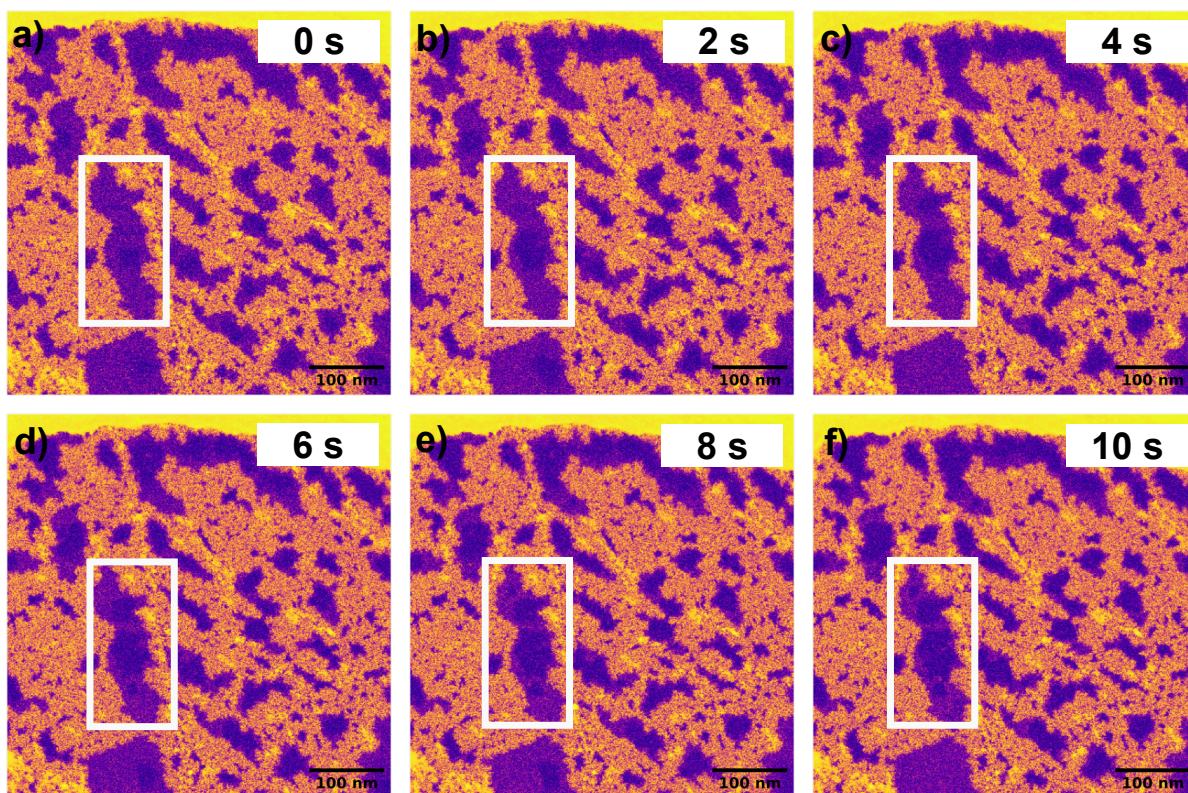
Figure 4.16: **MAADF time series showcasing the dissociation of hydrocarbon contamination after annealing at 150°C.** The small clean patch in the center of the boxed area in (a) grows over time as a result of dehydrogenation and polymerization of the hydrocarbon contamination, turning it into amorphous carbon. It also retracts towards the sides (brighter contrast), resulting in larger clean areas.
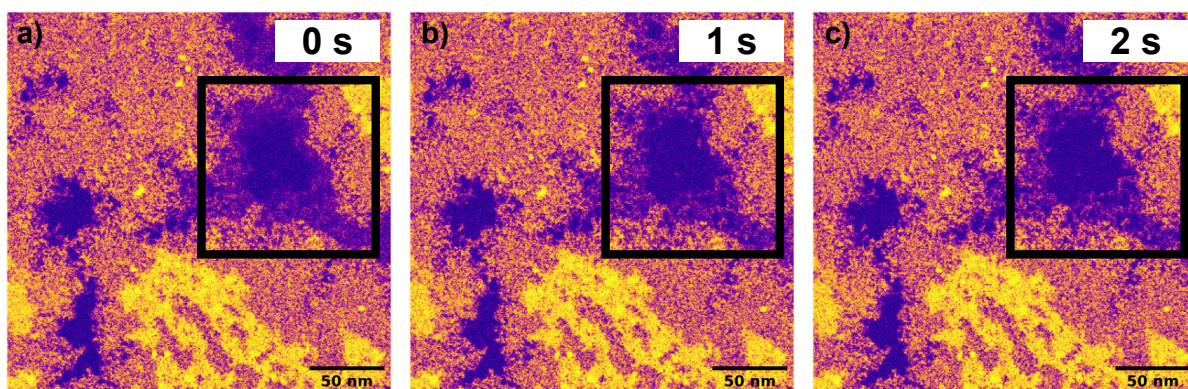

Figure 4.17: **MAADF time series showing the dehydrogenation of hydrocarbon contamination after annealing at 200°C.** The size of the clean area (darkest contrast) in the center of the boxed area in (a) grows over 2 s, after which it reaches its final state in (c).

4.2.3 Contamination behavior

When acquiring MAADF images of the samples that were annealed at 150°C and 200°C, some of the clean-looking areas (by contrast) were actually covered by a thin film of contamination, which only became apparent upon higher magnification. When exposed to the electron beam, this thin contamination started to retract toward the thicker contamination surrounding it. Figure 4.16 shows a time series of MAADF images with individual scan times of about 1 s, where every other frame is shown. The boxed area shows how the clean areas grow over about 10 s. This transformation can also be seen in the other areas in the image with darker contrast. This is a direct observation of the dehydrogenation and subsequent transformation of the hydrocarbon contamination into amorphous carbon on the surface of graphene [121] upon exposure to the electron beam, resulting in larger clean areas (darkest contrast). Figure 4.17 shows similar behavior on the sample that was baked at 200°C. Here, this dehydrogenation process is quicker due to the increased local current density (higher magnification image) during image acquisition. As a result, the total clean area before e-beam exposure is significantly lower than after, meaning that using electron microscopy techniques to assess the cleanliness of these samples can directly affect the result. This has to be taken into account when comparing against results from other studies that used other assessment methods. However, since most of the samples introduced into the CANVAS system at the University of Vienna will be imaged using the Nion UltraSTEM 100, this ramification may benefit the observer since larger clean areas are rarely undesired.

Regarding the desorption of hydrocarbons, Paserba and Gellman [32] showed that there is a relation between the length of hydrocarbon oligomers and their desorption temperature, as well as their number of layers. They experimentally determined that alkanes with lengths of $5 \leq n \leq 60$ have peak desorption temperatures ranging from -104°C to 450°C on flat graphite substrates. If there are multiple layers of alkanes present, the adlayers already start to desorb at lower temperatures. This implies that the contaminant hydrocarbon chains containing up to around 20 carbon atoms should have already been desorbed when the samples were baked at 150°C inside the loadlock. Given that the observed amount of mobile contamination on the sample annealed at a reported temperature of 100°C is much lower than before the treatment, the relatively low annealing temperature suggests that only small hydrocarbon or adlayers of contamination were desorbed during this process. Schweizer et al. [61] attributed the mobile contamination that they observed to larger hydrocarbon specimens. However, they were only

estimating the diffusion constant D, which they used to estimate the molecule sizes, using the simple Einstein relation for diffusion in two dimensions, $D = \frac{x^2}{4t}$, with the time t and mean displacement x. Also, the microscope vacuum was only in the 10^{-7} mbar range, which could supply additional contaminants to the sample surface. Müller et al. [59] also suggested that the majority of the surface contaminants consist of larger hydrocarbon molecules, which was determined by fitting the parametric reaction-diffusion equation to their experimental findings. However, they used thin amorphous carbon films as their substrates instead of graphene, and the pressure in the microscope column was only $5 \cdot 10^{-6}$ mbar.

Regardless, annealing to 100°C or higher seemed to be effective in reducing the amount of mobile contamination on the samples used in this work. Adlayers of longer hydrocarbon chains were likely desorbed during the annealing procedure, with a thin layer still present. This reduction heavily reduces the amount of electron beam-induced hydrocarbon deposition, especially when some thicker immobile contamination is still present, which acts as a shield for the residual contamination arising from surface diffusion during microscope operation.

4.2.4 Annealing response of a beam showered area

Comparing the same area before and after the heating process provides valuable insight into how the structure of the contamination changes. The Nion UltraSTEM 100 can save the stage positions at any point, which allows for finding the same area again. While the heating process will change the exact positions due to thermal expansion and contraction, as well as the contribution from stage drift in the microscope, locating the same spot is a quite straightforward procedure. Inconsistencies or very pronounced contaminants on the sample support can act as guides. Here, an area was beam showered before the annealing process (Figure 4.3), and was found again afterward (Figure 4.18).

Before annealing, the beam showered area has a brighter contrast when compared to the surrounding area. This suggests a thinning of the amorphous carbon support. However, after the heating process, the same area is now darker than its surroundings, indicating an increased thickness. One explanation could be the combined effect of beam showering, namely hydrocarbon decomposition, and oxygen etching. Firstly, carbon-rich molecules are deposited and turned into (mostly) amorphous carbon [58, 119], and secondly, oxygen in the contamination is reduced due to etching inside the oxygen-rich contamination [123]. The latter could be responsible for the different behavior of the higher amounts of now oxygen-poor amorphous
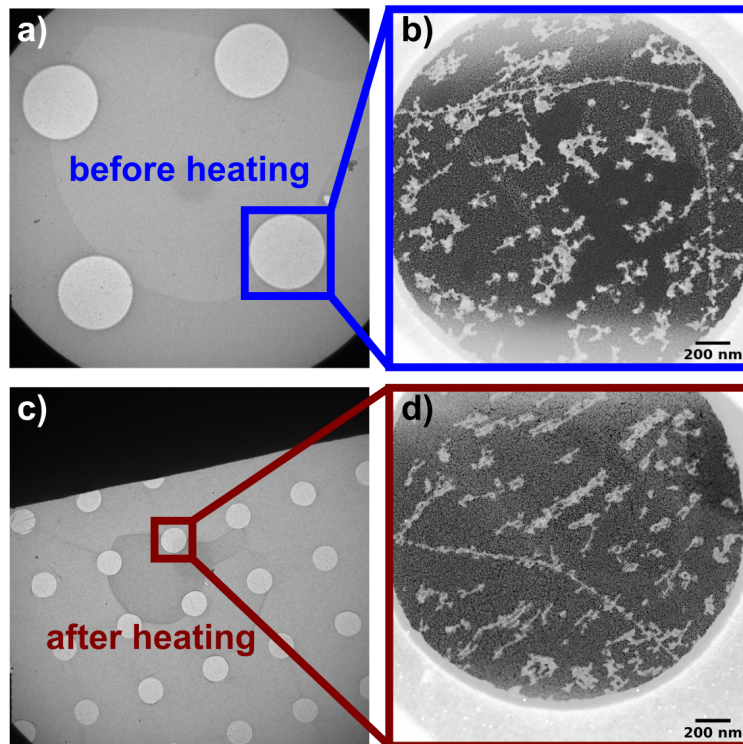
Figure 4.18: **Comparison of the same area before and after the heating process.** (a) CCD image of the beam showered area before the heating treatment. (b) MAADF image of one of the beam showered holes in (a). (c) The same area after heating to 150°C. (d) MAADF image of another beam showered hole after the cleaning process, which shows no signs of cleaning.

carbon contamination under thermal annealing. The higher magnification MAADF image in Figure 4.18d reveals that that hole was not cleaned at all. In fact, there is a thick film of amorphous contamination obfuscating the underlying structure. Despite Figures 4.18b and 4.18d not showing the same hole, they were both exposed to the beam shower before the heating process, and both exhibit a high amount of contamination. Similar observations were made by Dyck et al. [121] and van Dorp et al. [127] where small areas that were irradiated by electrons before heating did not undergo any changes, while other parts of their samples were cleaned.

However, electron irradiation in the form of beam showering was necessary due to the heavy mobile contamination on the untreated samples in this work (as already described in section 4.1.1) but this then makes a direct comparison of contamination on the atomic scale difficult. Perhaps, this type of characterization could be achievable if the as-prepared samples were not this heavily affected by mobile contamination.

Chapter 5

Conclusions

The two main objectives of this study were the implementation into and characterization of the UHV heating stage in the CANVAS system, as well as the quantification of the cleaning effect of graphene (and potentially other 2D materials) at temperatures that can be reached inside the oven. After iterating the design for the heating stage twice, this was achieved. The current implementation allows for thermal annealing in UHV up to (reported) temperatures of about 400°C at a tungsten wire power of 80 W. Its operation requires only minimal training, and servicing is trivial due to the rigid assembly and integration of the oven design. It is possible to reach higher temperatures and faster heating rates by using a thinner tungsten wire, but this increases the chance of wire breakage, and the longevity of the wire was prioritized to keep maintenance low.

Since the temperatures measured in this work are likely lower than the actual values, it raises the question of what might be the origin of this discrepancy. While the thermocouple may report the temperatures accurately, it might be measured at the incorrect spot. It is possible that the two leads join not at the tip of the thermocouple, but at some point before it. However, without cutting it open, this is difficult to verify. Another possibility is that the thermocouple is not a K-type, despite the manufacturer's claims, which could result in different voltage readings that translate to incorrect temperatures. Also, regardless of the integrity of the thermocouple, the spot where we measure the temperature is probably lower than what we actually have on the sample surface, as we are probing the area at the bottom of the puck (farther away from the tungsten wire). However, assuming that the oven is in thermal equilibrium when sustaining a set temperature, it should be reasonably accurate. This issue needs further investigation, perhaps an alternative design to probe the temperature, which should be addressed in the

future.

At the temperatures used in this study, the amount of desorption of contamination was minimal but diffusion was high, which could be explained by low annealing temperatures [32]. Methods that probe large areas such as Raman spectroscopy or XPS would not consider these samples as clean as the bulk of the contamination has not been removed despite larger clean areas cropping up due to the annealing process. In addition, these methods are also unable to determine the sizes of clean areas, which was performed in this work. It is important to emphasize that the measured amount of clean area is not indicative of the cleanliness of the sample as a whole but rather quantifies the usable clean area for the fundamental study of 2D materials. Clearly, very thick layers of contamination are of no interest if the material itself is to be studied.

To get a better understanding of the cleaning process, a direct comparison of the same area before and after the heating treatment is desired. This would allow for the study of the evolution and transformation of pre-existing contamination. However, this seems to be impossible if the pre-treated samples require beam showering due to the high amount of mobile contamination present on the sample surface, as the beam showered area is impervious to cleaning via thermal annealing [121]. Perhaps a different sample preparation process or different source material could alleviate this issue.

In conclusion, most of the cleaning effect likely resulted from diffusion rather than desorption of the contaminants, with some of the cleaning possibly being attributed to thermal expansion and contraction of the sample and sample support. A diffusion-dominant process is expected at low annealing temperatures, where the desorption temperature of the hydrocarbon molecules that make up the bulk of the contamination has not been reached yet [32]. While it is possible that some adlayers were desorbed, hydrocarbon contamination is definitely still present on all samples that were annealed in this work. The average sizes of the clean and exposed graphene patches increased drastically upon annealing at 150°C and 200°C, which could prove useful for sample manipulation experiments [114, 126]. The annealed samples also exhibited a lower amount of mobile contamination, allowing extended microscopy sessions without the interference of electron beam induced hydrocarbon deposition. Annealing at higher (but still below the desorption) temperatures seems to produce larger clean areas, which can be explained by the linear increase of the diffusion constant with temperature [124]. By raising the temperature, we increase the diffusion of the hydrocarbon molecules, which causes them to become

more mobile and eventually get stuck on pre-existing contamination. Annealing at even higher temperatures as well as different durations, beyond what was performed in this work, could produce even cleaner samples, which can be explored in future studies.

Bibliography

[1]   K. S. Novoselov *et al.* Electric field in atomically thin carbon films. *Science* **306** (2004), 666–669. DOI: `DOI:10.1126/science.1102896`.

[2]   S. Roy *et al.* Structure, Properties and Applications of Two-Dimensional Hexagonal Boron Nitride. *Advanced Materials* **33** (2021), 2101589. DOI: `10.1002/ADMA.202101589`.

[3]   S. Manzeli *et al.* 2D transition metal dichalcogenides. *Nature Reviews Materials* **2** (2017), 17033–17033. DOI: `10.1038/natrevmats.2017.33`.

[4]   A. Falin *et al.* Mechanical properties of atomically thin boron nitride and the role of interlayer interactions. *Nature Communications* **8** (2017), 15815. DOI: `10.1038/ncomms15815`.

[5]   K. I. Bolotin *et al.* Ultrahigh electron mobility in suspended graphene. *Solid State Communications* **146** (2008), 351–355. DOI: `10.1016/j.ssc.2008.02.024`.

[6]   K. F. Mak *et al.* Atomically Thin MoS2 : A New Direct-Gap Semiconductor. *Physical Review Letters* **105** (2010), 136805. DOI: `10.1103/PhysRevLett.105.136805`.

[7]   C. Elias *et al.* Direct band-gap crossover in epitaxial monolayer boron nitride. *Nature Communications* **10** (2019), 2639. DOI: `10.1038/s41467-019-10610-5`.

[8]   C. Ruppert, B. Aslan, and T. F. Heinz. Optical Properties and Band Gap of Single- and Few-Layer MoTe2 Crystals. *Nano Letters* **14** (2014), 6231–6236. DOI: `10.1021/nl502557g`.

[9]   C. Li *et al.* Purification of single-photon emission from hBN using post-processing treatments. *Nanophotonics* **8** (2019), 2049–2055. DOI: `10.1515/nanoph-2019-0099`.

[10] A. A. Balandin *et al.* Superior Thermal Conductivity of Single-Layer Graphene. *Nano Letters* **8** (2008), 902–907. DOI: `10.1021/nl0731872`.

[11]   Q. Cai *et al.* High thermal conductivity of high-quality monolayer boron nitride and its thermal expansion. *Science Advances* **5** (2019), eaav0129. DOI: `10.1126/sciadv.aav0129`.

[12]   G. López-Polín *et al.* Increasing the elastic modulus of graphene by controlled defect creation. *Nature Physics* **11** (2015), 26–31. DOI: `10.1038/nphys3183`.

[13]   J. Jiang *et al.* Defect Engineering in 2D Materials: Precise Manipulation and Improved Functionalities. *Research* **2019** (2019), 4641739. DOI: `10.34133/2019/4641739`.

[14]   L. Lin *et al.* Towards super-clean graphene. *Nature Communications* **10** (2019), 1912. DOI: `10.1038/s41467-019-09565-4`.

[15]   Z. Li *et al.* Effect of airborne contaminants on the wettability of supported graphene and graphite. *Nature Materials 2013 12:10* **12** (2013), 925–931. DOI: `10.1038/nmat3709`.

[16]   Y. Dan *et al.* Intrinsic response of graphene vapor sensors. *Nano Letters* **9** (2009), 1472–1475. DOI: `10.1021/nl8033637`.

[17]   P. L. Levesque *et al.* Probing Charge Transfer at Surfaces Using Graphene Transistors. *Nano Letters* **11** (2011), 132–137. DOI: `10.1021/nl103015w`.

[18]   A. Pirkle *et al.* The effect of chemical residues on the physical and electrical properties of chemical vapor deposited graphene transferred to SiO2. *Applied Physics Letters* **99** (2011), 122108. DOI: `10.1063/1.3643444`.

[19]   J. W. Suk *et al.* Enhancement of the Electrical Properties of Graphene Grown by Chemical Vapor Deposition via Controlling the Effects of Polymer Residue. *Nano Letters* **13** (2013), 1462–1467. DOI: `10.1021/nl304420b`.

[20]   A. Grubišić-Čabo *et al.* In Situ Exfoliation Method of Large-Area 2D Materials. *Advanced Science* **10** (2023), 2301243. DOI: `10.1002/ADVS.202301243`.

[21]   K. E. Whitener and P. E. Sheehan. Graphene synthesis. *Diamond and Related Materials* **46** (2014), 25–34. DOI: `10.1016/J.DIAMOND.2014.04.006`.

[22]   R. Lv *et al.* Transition metal dichalcogenides and beyond: Synthesis, properties, and applications of single- and few-layer nanosheets. *Accounts of Chemical Research* **48** (2015), 56–64. DOI: `10.1021/ar5002846`.

[23]   K. Zhang *et al.* Two dimensional hexagonal boron nitride (2D-hBN): synthesis, properties and applications. *Journal of Materials Chemistry C* **5** (2017), 11992–12022. DOI: `10.1039/C7TC04300G`.

[24] S. Ryu *et al.* Atmospheric oxygen binding and hole doping in deformed graphene on a SiO2 substrate. *Nano Letters* **10** (2010), 4944–4951. DOI: 10.1021/nl1029607.

[25] S. Berciaud *et al.* Probing the Intrinsic Properties of Exfoliated Graphene: Raman Spectroscopy of Free-Standing Monolayers. *Nano Letters* **9** (2009), 346–352. DOI: 10.1021/nl8031444.

[26] Y. Ahn *et al.* Procedure of removing polymer residues and its influences on electronic and structural characteristics of graphene. *Applied Physics Letters* **102** (2013), 091602. DOI: 10.1063/1.4794900.

[27] A. Pálinkás *et al.* The composition and structure of the ubiquitous hydrocarbon contamination on van der Waals materials. *Nature Communications* **13** (2022), 6770. DOI: 10.1038/s41467-022-34641-7.

[28] G. Cunge *et al.* Dry efficient cleaning of poly-methyl-methacrylate residues from graphene with high-density H2 and H2-N2 plasmas. *Journal of Applied Physics* **118** (2015), 123302. DOI: 10.1063/1.4931370.

[29] N. Lindvall, A. Kalabukhov, and A. Yurgens. Cleaning graphene using atomic force microscope. *Journal of Applied Physics* **111** (2012), 064904. DOI: 10.1063/1.3695451.

[30] D. G. Purdie *et al.* Cleaning interfaces in layered materials heterostructures. *Nature Communications* **9** (2018), 5387–5387. DOI: 10.1038/s41467-018-07558-3.

[31] I. Gasparutti *et al.* How Clean Is Clean? Recipes for van der Waals Heterostructure Cleanliness Assessment. *ACS Applied Materials & Interfaces* **12** (2020), 7701–7709. DOI: 10.1021/acsami.9b18821.

[32] K. R. Paserba and A. J. Gellman. Kinetics and energetics of oligomer desorption from surfaces. *Physical Review Letters* **86** (2001), 4338–4341. DOI: 10.1103/PhysRevLett.86.4338.

[33] D. R. G. Mitchell. Contamination mitigation strategies for scanning transmission electron microscopy. *Micron* **73** (2015), 36–46. DOI: 10.1016/j.micron.2015.03.013.

[34] C. Gong *et al.* Rapid Selective Etching of PMMA Residues from Transferred Graphene by Carbon Dioxide. *The Journal of Physical Chemistry C* **117** (2013), 23000–23008. DOI: 10.1021/jp408429v.

[35] K. Kumar, Y. S. Kim, and E. H. Yang. The influence of thermal annealing to remove polymeric residue on the electronic doping and morphological characteristics of graphene. *Carbon* **65** (2013), 35–45. DOI: 10.1016/J.CARBON.2013.07.088.

[36] Y. Ahn *et al.* Thermal annealing of graphene to remove polymer residues. *Materials Express* **6** (2016), 69–76. DOI: 10.1166/mex.2016.1272.

[37] J. Hong *et al.* Origin of New Broad Raman D and G Peaks in Annealed Graphene. *Scientific Reports* **3** (2013), 2700. DOI: 10.1038/srep02700.

[38] Y.-C. Lin *et al.* Clean Transfer of Graphene for Isolation and Suspension. *ACS Nano* **5** (2011), 2362–2368. DOI: 10.1021/nn200105j.

[39] Z. Cheng *et al.* Toward Intrinsic Graphene Surfaces: A Systematic Study on Thermal Annealing and Wet-Chemical Treatment of SiO 2 -Supported Graphene Devices. *Nano Letters* **11** (2011), 767–771. DOI: 10.1021/nl103977d.

[40] I. Jo *et al.* Thermal Conductivity and Phonon Transport in Suspended Few-Layer Hexagonal Boron Nitride. *Nano Letters* **13** (2013), 550–554. DOI: 10.1021/nl304060g.

[41] M. T. Pettes *et al.* Influence of Polymeric Residue on the Thermal Conductivity of Suspended Bilayer Graphene. *Nano Letters* **11** (2011), 1195–1200. DOI: 10.1021/nl104156y.

[42] J. D. Wood *et al.* Annealing free, clean graphene transfer using alternative polymer scaffolds. *Nanotechnology* **26** (2015), 055302. DOI: 10.1088/0957-4484/26/5/055302.

[43] E. Auchter *et al.* A facile alternative technique for large-area graphene transfer via sacrificial polymer. *AIP Advances* **7** (2017), 125306. DOI: 10.1063/1.4986780.

[44] X. Yang and M. Yan. Removing contaminants from transferred CVD graphene. *Nano Research* **13** (2020), 599–610. DOI: 10.1007/s12274-020-2671-6.

[45] H. J. Vandenburg *et al.* A simple solvent selection method for accelerated solvent extraction of additives from polymers. *Analyst* **124** (1999), 1707–1710. DOI: 10.1039/A904631C.

[46] A. Castellanos-Gomez *et al.* Deterministic transfer of two-dimensional materials by all-dry viscoelastic stamping. *2D Materials* **1** (2014), 011002. DOI: 10.1088/2053-1583/1/1/011002.

[47] S. R. Na *et al.* Selective Mechanical Transfer of Graphene from Seed Copper Foil Using Rate Effects. *ACS Nano* **9** (2015), 1325–1335. DOI: 10.1021/nn505178g.

[48] L. Wang *et al.* One-Dimensional Electrical Contact to a Two-Dimensional Material. *Science* **342** (2013), 614–617. DOI: 10.1126/science.1244358.

[49] W. Wang *et al.* Clean assembly of van der Waals heterostructures using silicon nitride membranes. *Nature Electronics* **6** (2023), 981–990. DOI: `10.1038/s41928-023-01075-y`.

[50] M. Nakatani *et al.* Ready-to-transfer two-dimensional materials using tunable adhesive force tapes. *Nature Electronics 2024 7:2* **7** (2024), 119–130. DOI: `10.1038/s41928-024-01121-3`.

[51] W. Xie *et al.* Fixed carbon content and reaction mechanism of natural microcrystalline graphite purified by hydrochloric acid and sodium fluoride. *International Journal of Mineral Processing* **155** (2016), 45–54. DOI: `10.1016/j.minpro.2016.08.002`.

[52] R. Jalili *et al.* Silicon as a ubiquitous contaminant in graphene derivatives with significant impact on device performance. *Nature Communications* **9** (2018), 5070. DOI: `10.1038/s41467-018-07396-3`.

[53] I. Ruiz *et al.* Silicon Oxide Contamination of Graphene Sheets Synthesized on Copper Substrates via Chemical Vapor Deposition. *Advanced Science, Engineering and Medicine* **6** (2014), 1070–1075. DOI: `10.1166/asem.2014.1615`.

[54] G. Algara-Siller *et al.* Dry-cleaning of graphene. *Applied Physics Letters* **104** (2014), 153115. DOI: `10.1063/1.4871997`.

[55] T. Susi, J. C. Meyer, and J. Kotakoski. Manipulating low-dimensional materials down to the level of single atoms with electron irradiation. *Ultramicroscopy* **180** (2017), 163–172. DOI: `10.1016/j.ultramic.2017.03.005`.

[56] M. R. Ahmadpour Monazam *et al.* Substitutional Si impurities in monolayer hexagonal boron nitride. *Applied Physics Letters* **115** (2019), 071604. DOI: `10.1063/1.5112375`.

[57] J. J. Hren. Specimen contamination in analytical electron microscopy: Sources and solutions. *Ultramicroscopy* **3** (1978), 375–380. DOI: `10.1016/S0304-3991(78)80057-6`.

[58] S. Hettler *et al.* Carbon contamination in scanning transmission electron microscopy and its impact on phase-plate applications. *Micron* **96** (2017), 38–47. DOI: `10.1016/j.micron.2017.02.002`.

[59] E. Müller *et al.* Reaction-diffusion study of electron-beam-induced contamination growth. *Ultramicroscopy* **264** (2024), 113995. DOI: `10.1016/j.ultramic.2024.113995`.

[60] T. Bret *et al.* Characterization of focused electron beam induced carbon deposits from organic precursors. *Microelectronic Engineering*. Proceedings of the 30th International Conference on Micro- and Nano-Engineering **78-79** (2005), 300–306. DOI: `10.1016/j.mee.2005.01.006`.

[61] P. Schweizer *et al.* Mechanical cleaning of graphene using in situ electron microscopy. *Nature Communications 2020 11:1* **11** (2020), 1–9. DOI: `10.1038/s41467-020-15255-3`.

[62] L. Reimer and M. Wächter. Contribution to the contamination problem in transmission electron microscopy. *Ultramicroscopy* **3** (1978), 169–174. DOI: `10.1016/S0304-3991(78)80023-0`.

[63] H. Chou *et al.* Revealing the planar chemistry of two-dimensional heterostructures at the atomic level. *Nature Communications* **6** (2015), 7482. DOI: `10.1038/ncomms8482`.

[64] B. Zhuang *et al.* Ways to eliminate PMMA residues on graphene —— superclean graphene. *Carbon* **173** (2021), 609–636. DOI: `10.1016/j.carbon.2020.11.047`.

[65] N. Peltekis *et al.* The effect of downstream plasma treatments on graphene surfaces. *Carbon* **50** (2012), 395–403. DOI: `10.1016/j.carbon.2011.08.052`.

[66] D. Ferrah *et al.* XPS investigations of graphene surface cleaning using H2- and Cl2-based inductively coupled plasma. *Surface and Interface Analysis* **48** (2016), 451–455. DOI: `10.1002/sia.6010`.

[67] D. Ferrah *et al.* CF4/H2 Plasma Cleaning of Graphene Regenerates Electronic Properties of the Pristine Material. *ACS Applied Nano Materials* **2** (2019), 1356–1366. DOI: `10.1021/acsanm.8b02249`.

[68] M. Tripathi *et al.* Cleaning graphene: Comparing heat treatments in air and in vacuum. *physica status solidi (RRL) – Rapid Research Letters* **11** (2017), 1700124. DOI: `10.1002/pssr.201700124`.

[69] Y. Jia *et al.* Toward High Carrier Mobility and Low Contact Resistance: Laser Cleaning of PMMA Residues on Graphene Surfaces. *Nano-Micro Letters* **8** (2016), 336–346. DOI: `10.1007/s40820-016-0093-5`.

[70] J. Zhang *et al.* Large-Area Synthesis of Superclean Graphene via Selective Etching of Amorphous Carbon with Carbon Dioxide. *Angewandte Chemie International Edition* **58** (2019), 14446–14451. DOI: `10.1002/anie.201905672`.

[71] X. Wang *et al.* Direct Observation of Poly(Methyl Methacrylate) Removal from a Graphene Surface. *Chemistry of Materials* **29** (2017), 2033–2039. DOI: 10.1021/acs.chemmater.6b03875.

[72] N. Hong *et al.* Facile synthesis of graphene by pyrolysis of poly(methyl methacrylate) on nickel particles in the confined microzones. *Materials Research Bulletin* **47** (2012), 4082–4088. DOI: 10.1016/j.materresbull.2012.08.049.

[73] L. H. Karlsson *et al.* Graphene on graphene formation from PMMA residues during annealing. *Vacuum* **137** (2017), 191–194. DOI: 10.1016/J.VACUUM.2017.01.004.

[74] W. Xie *et al.* Clean graphene surface through high temperature annealing. *Carbon* **94** (2015), 740–748. DOI: 10.1016/j.carbon.2015.07.046.

[75] Y.-C. Lin *et al.* Graphene Annealing: How Clean Can It Be? *Nano Letters* **12** (2012), 414–419. DOI: 10.1021/nl203733r.

[76] W. Choi *et al.* Effect of annealing in Ar/H2 environment on chemical vapor deposition-grown graphene transferred with poly (Methyl Methacrylate). *IEEE Transactions on Nanotechnology* **14** (2015), 70–74. DOI: 10.1109/TNANO.2014.2365208.

[77] I. Vlassiouk *et al.* Role of Hydrogen in Chemical Vapor Deposition Growth of Large Single-Crystal Graphene. *ACS Nano* **5** (2011), 6069–6076. DOI: 10.1021/nn201978y.

[78] E. Stolyarova *et al.* Observation of Graphene Bubbles and Effective Mass Transport under Graphene Films. *Nano Letters* **9** (2009), 332–337. DOI: 10.1021/nl803087x.

[79] G. F. Schneider *et al.* DNA Translocation through Graphene Nanopores. *Nano Letters* **10** (2010), 3163–3167. DOI: 10.1021/nl102069z.

[80] T. Xu *et al.* Size-Dependent Evolution of Graphene Nanopores Under Thermal Excitation. *Small* **8** (2012), 3422–3426. DOI: 10.1002/smll.201200979.

[81] S. Coh and D. Vanderbilt. Python Tight Binding (PythTB). Zenodo (2022). URL: https://doi.org/10.5281/zenodo.12721315 (accessed on 14 June 2024).

[82] K. S. Novoselov *et al.* Two-dimensional gas of massless Dirac fermions in graphene. *Nature* **438** (2005), 197–200. DOI: 10.1038/nature04233.

[83] V. Ariel. Effective Mass and Energy-Mass Relationship. *arXiv* (2012), 1205.3995.

[84] V. Ariel and A. Natan. Electron effective mass in graphene. In: *2013 International Conference on Electromagnetics in Advanced Applications (ICEAA)*, pp. 696–698. DOI: 10.1109/ICEAA.2013.6632334.

[85] Z. Chen *et al.* Variation and consistency of Young's modulus in steel. *Journal of Materials Processing Technology* **227** (2016), 227–243. DOI: `10.1016/j.jmatprotec.2015.08.024`.

[86] L. Banszerus *et al.* Ultrahigh-mobility graphene devices from chemical vapor deposition on reusable copper. *Science Advances* **1** (2015), 1:e1500222. DOI: `10.1126/sciadv.1500222`.

[87] A. H. Castro Neto *et al.* The electronic properties of graphene. *Reviews of Modern Physics* **81** (2009), 109–162. DOI: `10.1103/RevModPhys.81.109`.

[88] Solids, Liquids and Gases - Thermal Conductivities. URL: `https://www.engineeringtoolbox.com/thermal-conductivity-d_429.html` (accessed on 8 May 2024).

[89] H. D. Young. University physics. 8th ed. (Addison-Wesley Pub. Co., USA, 1992).

[90] W. Bao *et al.* Controlled ripple texturing of suspended graphene and ultrathin graphite membranes. *Nature Nanotechnology* **4** (2009), 562–566. DOI: `10.1038/nnano.2009.191`.

[91] E. Abbe. Beiträge zur Theorie des Mikroskops und der mikroskopischen Wahrnehmung: I. Die Construction von Mikroskopen auf Grund der Theorie. *Archiv für mikroskopische Anatomie* **9** (1873), 413–418. DOI: `10.1007/BF02956173`.

[92] E. Abbe. The Relation of Aperture and Power in the Microscope. *Journal of the Royal Microscopical Society* **2** (1882), 300–309. DOI: `10.1111/J.1365-2818.1882.TB00190.X`.

[93] E. Hecht and A. Zajac. Optics. Vol. Fourth Edit. (Pearson Higher Education, USA, 2003).

[94] L. De Broglie. Recherches sur la théorie des Quanta. *Annales de Physique* **10** (1925), 22–128. DOI: `10.1051/anphys/192510030022`.

[95] R. F. Egerton. Choice of operating voltage for a transmission electron microscope. *Ultramicroscopy* **145** (2014), 85–93. DOI: `10.1016/J.ULTRAMIC.2013.10.019`.

[96] P. D. Nellist. The Principles of STEM Imaging. *Scanning Transmission Electron Microscopy* (2011), 91–115. DOI: `10.1007/978-1-4419-7200-2_2`.

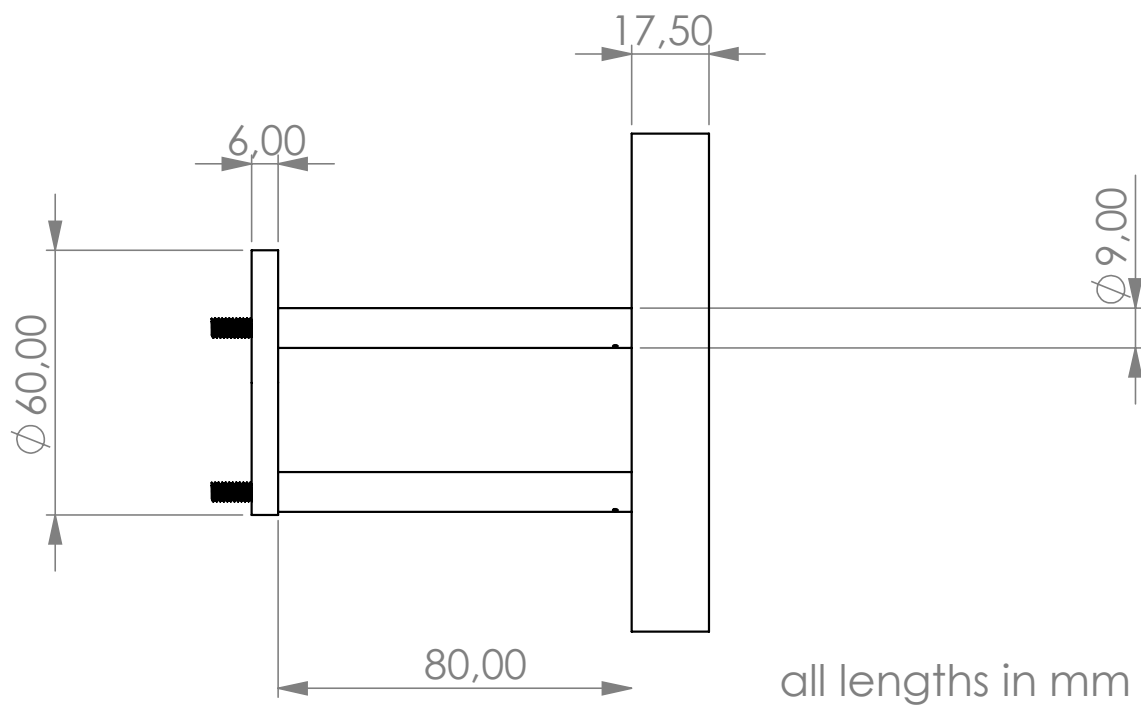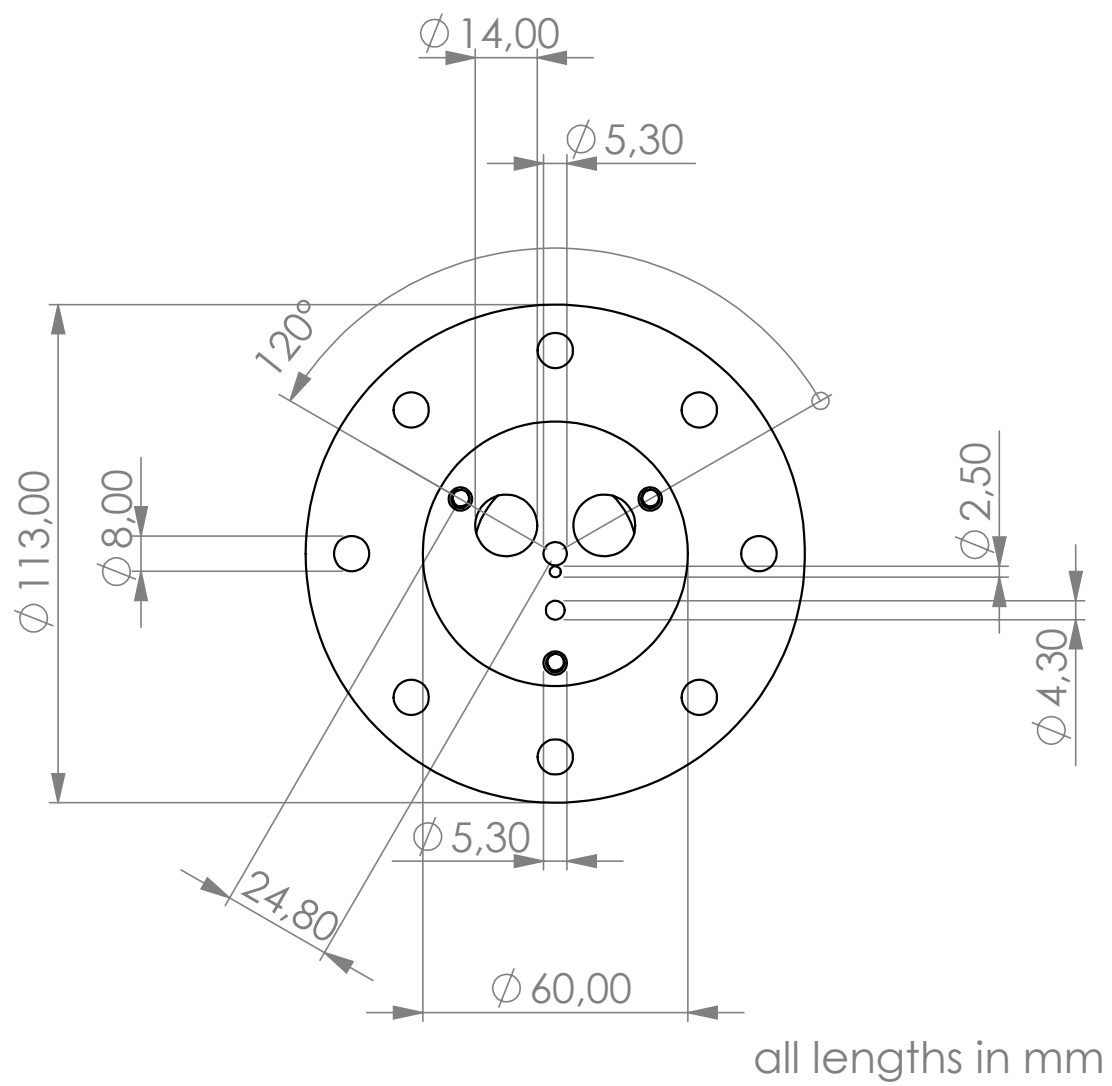[97] R. Gross and A. Marx. Festkörperphysik. 3rd ed. (De Gruyter, Berlin/Boston, 2018).

[98] Electron scattering. 2024. URL: https://en.wikipedia.org/w/index.php?title=Electron_scattering&oldid=1220202713 (accessed on 14 June 2024).

[99] D. B. Williams and C. B. Carter. Transmission electron microscopy: A textbook for materials science. 2nd ed. (Springer, New York, 2009).

[100] O. Krivanek *et al.* An electron microscope for the aberration-corrected era. *Ultramicroscopy* **108** (2008), 179–195. DOI: 10.1016/j.ultramic.2007.07.010.

[101] C. Mangler *et al.* A Materials Scientist's CANVAS: A System for Controlled Alteration of Nanomaterials in Vacuum Down to the Atomic Scale. *Microscopy and Microanalysis* **28** (2022), 2940–2942. DOI: 10.1017/S1431927622011023.

[102] M. Lentzen. Progress in Aberration-Corrected High-Resolution Transmission Electron Microscopy Using Hardware Aberration Correction. *Microscopy and Microanalysis* **12** (2006), 191–205. DOI: 10.1017/S1431927606060326.

[103] O. Krivanek, T. Lovejoy, and N. Dellby. Aberration-corrected STEM for atomic-resolution imaging and analysis. *Journal of Microscopy* **259** (2015), 165–172. DOI: 10.1111/jmi.12254.

[104] P. Hartel, H. Rose, and C. Dinges. Conditions and reasons for incoherent imaging in STEM. *Ultramicroscopy* **63** (1996), 93–114. DOI: 10.1016/0304-3991(96)00020-4.

[105] O. L. Krivanek *et al.* Atom-by-atom structural and chemical analysis by annular dark-field electron microscopy. *Nature 2010 464:7288* **464** (2010), 571–574. DOI: 10.1038/nature08879.

[106] EELS Atlas. URL: https://eels.info/atlas (accessed on 5 May 2024).

[107] R. F. Egerton. Electron Energy-Loss Spectroscopy in the Electron Microscope. 3rd ed. (Springer, New York, 2011).

[108] P. K. Chu and L. Li. Characterization of amorphous and nanocrystalline carbon films. *Materials Chemistry and Physics* **96** (2006), 253–277. DOI: 10.1016/j.matchemphys.2005.07.048.

[109] P. Patnaik. Handbook of inorganic chemicals. (McGraw Hill, New York, 2003).

[110] H. Unbehauen. Control Systems, Robotics and Automation - System Analysis and Control: Classical Approaches II. Vol. 2. (EOLSS Publishers/UNESCO, Paris, 2009).

[111] S. Uchida. Image processing and recognition for biological images. *Development, Growth & Differentiation* **55** (2013), 523–549. DOI: 10.1111/dgd.12054.

[112] P. Bankhead. Introduction to Bioimage Analysis. (2022). URL: https://bioimagebook.github.io/index.html (accessed on 2 May 2024).

[113] N. Otsu. A Threshold Selection Method from Gray-Level Histograms. *IEEE Trans Syst Man Cybern* **SMC**-**9** (1979), 62–66. DOI: 10.1109/TSMC.1979.4310076.

[114] T. Susi *et al.* Single-atom spectroscopy of phosphorus dopants implanted into graphene. *2D Materials* **4** (2017), 021013. DOI: 10.1088/2053-1583/aa5e78.

[115] M. Diociaiuti, S. Casciardi, and R. Sisto. The sp2 and sp3 fractions of unknown carbon materials: electron energy-loss near-edge structure analysis of C-K spectra acquired under the magic-angle condition by the electron nanobeam technique. *Micron* **90** (2016), 97–107. DOI: 10.1016/j.micron.2016.07.005.

[116] A. Jablonski *et al.* NIST Electron Elastic-Scattering Cross-Section Database Version 4.0, NIST Standard Reference Database Number 64, National Institute of Standards and Technology, Gaithersburg MD, 20899 (2016). 2016. DOI: 10.18434/T4/1502642. (accessed on 2 June 2024).

[117] C. Shannon. Communication in the Presence of Noise. *Proceedings of the IRE* **37** (1949), 10–21. DOI: 10.1109/JRPROC.1949.232969.

[118] R. Baraniuk. 10.2: Sampling Theorem. 2020. URL: https://eng.libretexts.org/Bookshelves/Electrical_Engineering/Signal_Processing_and_Modeling/Signals_and_Systems_(Baraniuk_et_al.)/10%3A_Sampling_and_Reconstruction/10.02%3A_Sampling_Theorem (accessed on 31 Aug. 2024).

[119] M. Hugenschmidt *et al.* Electron-Beam-Induced Carbon Contamination in STEM-in-SEM: Quantification and Mitigation. *Microscopy and Microanalysis* **29** (2023), 219–234. DOI: 10.1093/micmic/ozac003.

[120] W. F. van Dorp and C. W. Hagen. A critical literature review of focused electron beam induced deposition. *Journal of Applied Physics* **104** (2008), 081301. DOI: 10.1063/1.2977587.

[121] O. Dyck *et al.* Mitigating e-beam-induced hydrocarbon deposition on graphene foratomic-scale scanning transmission electron microscopy studies. *Journal of Vacuum Science & Technology B* **36** (2017), 011801. DOI: 10.1116/1.5003034.

[122] T. Malis, S. C. Cheng, and R. F. Egerton. EELS log-ratio technique for specimen-thickness measurement in the TEM. *Journal of Electron Microscopy Technique* **8** (1988), 193–200. DOI: 10.1002/jemt.1060080206.

[123] G. T. Leuthner *et al.* Scanning transmission electron microscopy under controlled low-pressure atmospheres. *Ultramicroscopy.* 75th Birthday of Christian Colliex, 85th Birthday of Archie Howie, and 75th Birthday of Hannes Lichte / PICO 2019 - Fifth Conference on Frontiers of Aberration Corrected Electron Microscopy **203** (2019), 76–81. DOI: 10.1016/j.ultramic.2019.02.002.

[124] A. Einstein. Über die von der molekularkinetischen Theorie der Wärme geforderte Bewegung von in ruhenden Flüssigkeiten suspendierten Teilchen. *Annalen der Physik* **322** (1905), 549–560. DOI: 10.1002/andp.19053220806.

[125] M. Sekimoto, H. Yoshihara, and T. Ohkubo. Silicon nitride single-layer x-ray mask. *Journal of Vacuum Science and Technology* **21** (1982), 1017–1021. DOI: 10.1116/1.571854.

[126] A. Trentino *et al.* Atomic-Level Structural Engineering of Graphene on a Mesoscopic Scale. *Nano Letters* **21** (2021), 5179–5185. DOI: 10.1021/ACS.NANOLETT.1C01214/ASSET/IMAGES/LARGE/NL1C01214_0004.JPEG.

[127] W. F. v. Dorp *et al.* Nanometer-scale lithography on microscopically clean graphene. *Nanotechnology* **22** (2011), 505303. DOI: 10.1088/0957-4484/22/50/505303.

Appendix A

Heating stage construction plan

Ø 14,00
Ø 5,30
120°
Ø 113,00
Ø 8,00
Ø 2,50
Ø 4,30
24,80
Ø 5,30
Ø 60,00

all lengths in mm

17,50
6,00
Ø 60,00
Ø 9,00
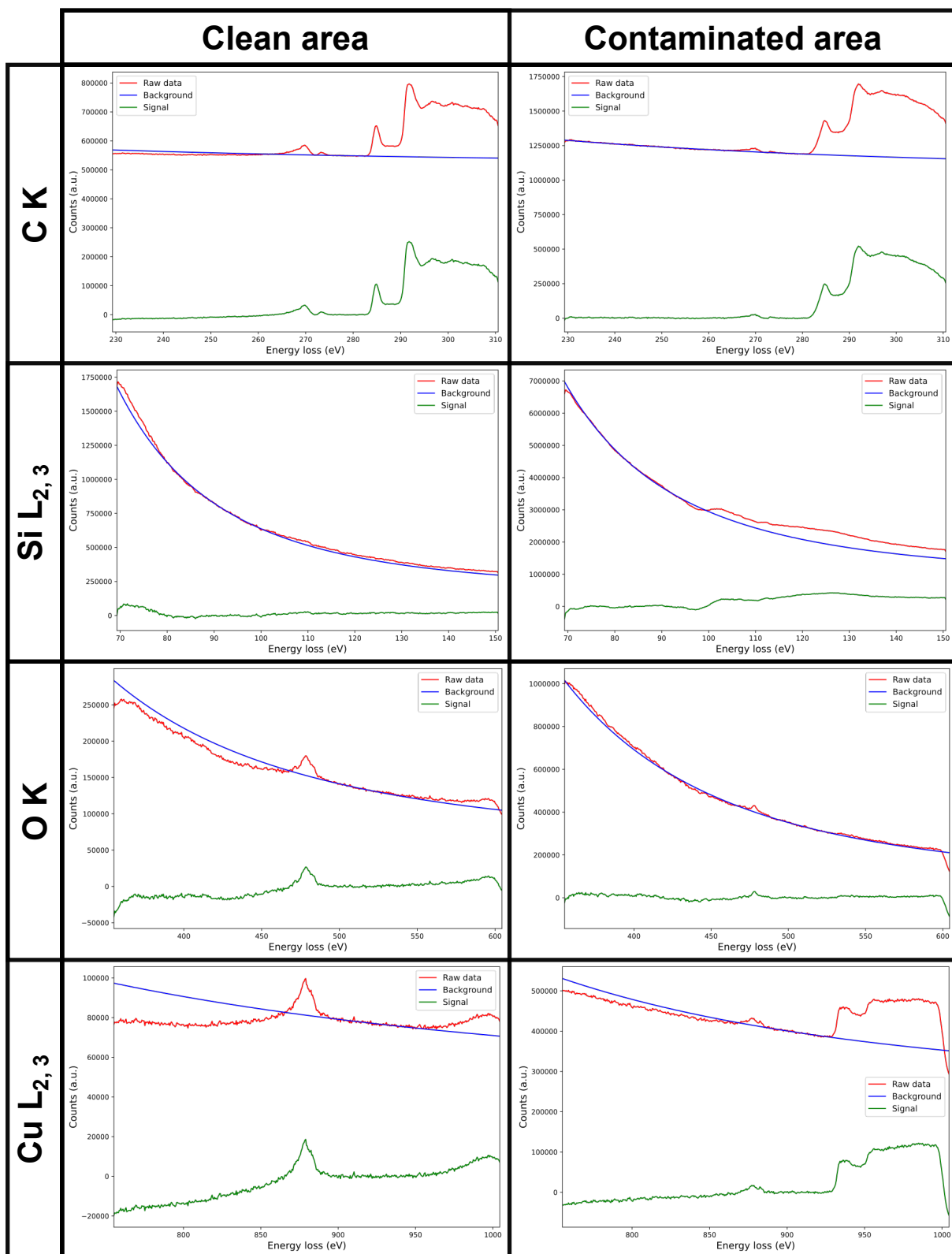80,00

all lengths in mm
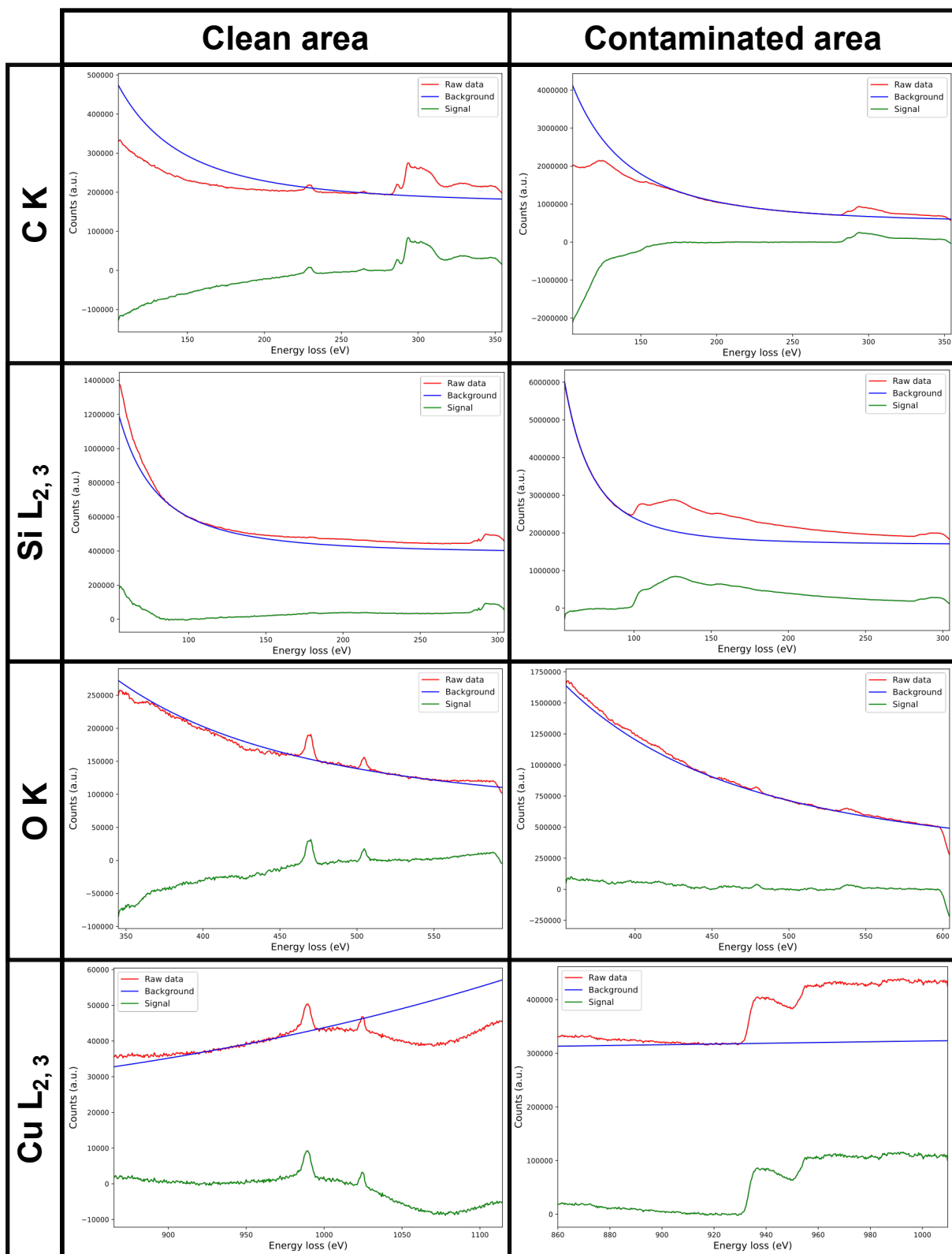
85

Appendix B

Raw data of EELS measurements

Before heating
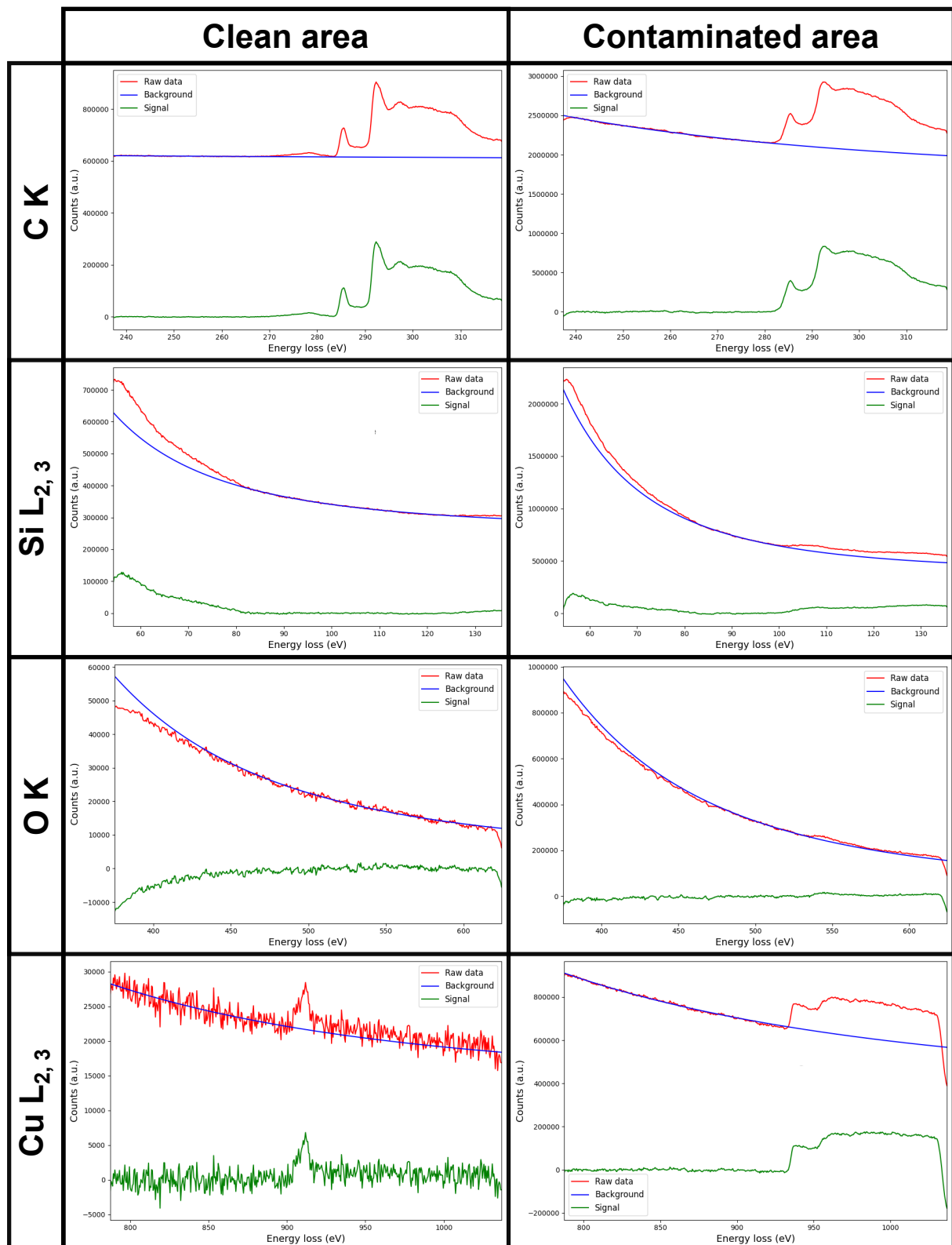
After heating (100°C for 2 h)

After heating (150°C for 2 h)

After heating (200°C for 2 h)